

CRANFIELD UNIVERSITY

HENRIQUE DA SILVA DAITX

DEVELOPMENT OF A COMBINED ATTITUDE AND  
POSITION CONTROLLER FOR A SATELLITE SIMULATOR

SCHOOL OF AEROSPACE, TRANSPORT AND  
MANUFACTURING  
MSc in Astronautics and Space Engineering

MSc Thesis  
Academic Year: 2014–2015

Supervisors:

Dr. James Whidborne

Dr. Markus Schlotterer

October 2015



CRANFIELD UNIVERSITY

SCHOOL OF AEROSPACE, TRANSPORT AND  
MANUFACTURING  
MSc in Astronautics and Space Engineering

MSc Thesis  
Academic Year: 2014–2015

HENRIQUE DA SILVA DAITX

DEVELOPMENT OF A COMBINED ATTITUDE AND  
POSITION CONTROLLER FOR A SATELLITE SIMULATOR

Supervisors:

Dr. James Whidborne  
at Cranfield University, UK

Dr. Markus Schlotterer  
at the Institute of Space Systems, DLR, Germany

October 2015

This thesis is submitted in partial (45%) fulfillment of the  
requirements for the degree of MSc in Astronautics and Space  
Engineering.

© Cranfield University 2015. All rights reserved. No part of this  
publication may be reproduced without the written permission of the  
copyright owner.



# Abstract

Formation flying is an emerging space technology which requires special facilities and methods for the purpose of GNC testing. This thesis documents the design and implementation of a combined position and attitude controller for a 5-DoF air bearing satellite simulator vehicle. Automated identification procedures were implemented and the relevant platform parameters—center of rotation, inertia tensor, thruster torque vectors—were identified. A static reference controller was developed as an intermediate step. Automated balancing procedures were also developed and applied, in order to eliminate a restricted class of gravity disturbances. Finally, a trajectory-following combined attitude and position controller was developed. To demonstrate its capabilities, a test was devised in which the vehicle moves around the experiment area while pointing a laser at a fixed target. The results obtained indicate all objectives were satisfactorily achieved.



# Acknowledgments

I would like to thank Dr. Schlotterer, for all the trust deposited in me before even meeting me, and in the course of these months at the DLR in Bremen. Thank you immensely for letting me work with my own ideas, but always being there ready to give good advice all the times I needed it.

I would like to thank my Cranfield supervisor, Dr. James Whidborne, for all the guidance (no pun intended) even being a few good miles of sea and land away.

Because of these same miles, I probably also left my course director Dr. Jenny Kingston quite anxious every time she got an email from me, as she knew I had some urgent problem that required her help. And help she did, every time. Thank you, Jenny.

Finally, it's impossible for me to thank my family properly as they deserve. I could write all day about my parents Ivani and Reinaldo, my sister Josi and my wife Vanessa, but their love and support goes far beyond what I am capable of describing in words; I can only recognize it with all my heart. Nothing I ever achieve will make me happier than knowing you are parts of me. Thank you.



# Contents

<b>1</b>	<b>Introduction</b>	<b>1</b>
1.1	Background . . . . .	1
1.2	DLR . . . . .	2
1.2.1	Formation flying and the TEAMS facility . . . . .	3
1.3	Objectives . . . . .	5
1.4	Report structure . . . . .	5
<b>2</b>	<b>Literature review</b>	<b>7</b>
2.1	Formation flying . . . . .	7
2.2	Satellite simulators . . . . .	9
2.3	Attitude . . . . .	11
<b>3</b>	<b>System</b>	<b>14</b>
3.1	Conventions . . . . .	14
3.2	Facility . . . . .	14
3.2.1	Granite table . . . . .	15
3.2.2	Optical tracking . . . . .	15
3.2.3	Compressed air system . . . . .	18
3.2.4	Control room . . . . .	18
3.3	Plant . . . . .	19
3.3.1	Air bearings . . . . .	19
3.3.2	Cold gas thrusters . . . . .	21
3.3.2.1	Thruster allocation . . . . .	22
3.3.3	Compressed air system . . . . .	24
3.3.4	Reaction wheels . . . . .	24
3.3.5	Power subsystem . . . . .	26
3.3.6	Onboard computer . . . . .	26
3.3.7	Inertial measuring unit . . . . .	26
3.3.8	Balancing system . . . . .	28
3.3.9	Laser . . . . .	28
3.4	Simulink . . . . .	29
3.5	Scope . . . . .	30
3.5.1	Initial state . . . . .	30
3.5.2	Final desired state . . . . .	30
3.6	Methodology . . . . .	31
3.7	Dynamics, kinematics . . . . .	32
<b>4</b>	<b>Parameter identification</b>	<b>34</b>
4.1	Center of rotation . . . . .	34

## *Contents*

4.2	Inertia tensor . . . . .	36
4.2.1	Results . . . . .	37
4.3	Thruster torque . . . . .	39
4.3.1	Results . . . . .	41
<b>5</b>	<b>Static control</b>	<b>43</b>
5.1	Control laws and attitude representation . . . . .	43
5.2	Linear Quadratic Regulator . . . . .	45
5.3	Results . . . . .	48
<b>6</b>	<b>Balancing</b>	<b>50</b>
6.1	Gravity disturbances . . . . .	50
6.1.1	Air mass unbalancing . . . . .	50
6.2	Off-line balancing . . . . .	51
6.3	On-line air mass variation correction . . . . .	52
6.3.1	Pressure-position model . . . . .	53
6.3.2	Spent gas estimation . . . . .	54
6.3.3	Closed-loop disturbance correction . . . . .	54
<b>7</b>	<b>Trajectory control</b>	<b>57</b>
7.1	Position . . . . .	58
7.1.1	Guidance . . . . .	58
7.1.2	Feedforward . . . . .	58
7.2	Attitude . . . . .	59
7.2.1	Guidance . . . . .	59
7.2.1.1	Simple pointing . . . . .	60
7.2.1.2	The “displaced pointing” problem . . . . .	61
7.2.1.3	Obtaining the solution . . . . .	62
7.2.1.4	Solution topology . . . . .	66
7.2.2	Feedforward . . . . .	67
<b>8</b>	<b>Conclusions</b>	<b>71</b>
8.1	Lessons learned . . . . .	71
8.2	Further work . . . . .	72
<b>References</b>		<b>73</b>
<b>A</b>	<b>Air mass inertia calculation</b>	<b>81</b>

# List of Figures

1.1	DLR sites . . . . .	3
1.2	Institute of Space Systems, Bremen. . . . .	4
1.3	TanDEM-X artistic depiction . . . . .	4
2.1	Disturbance sources . . . . .	10
2.2	Ames Research Center air bearing platform, 1959 . . . . .	11
2.3	Euler angles example . . . . .	12
3.1	Granite table . . . . .	15
3.2	How the DTrack system works . . . . .	16
3.3	DTrack camera . . . . .	16
3.4	DTrack reflective targets. . . . .	17
3.5	DTrack user software, main view. . . . .	17
3.6	Compressed air station . . . . .	18
3.7	Control room . . . . .	19
3.8	TEAMS_5D vehicle. . . . .	20
3.9	CAD drawings of the lower platform air bearings. . . . .	20
3.10	Attitude platform thrusters . . . . .	21
3.11	Thruster block geometrical configuration . . . . .	22
3.12	Compressed air system . . . . .	23
3.13	Reaction wheel . . . . .	24
3.14	Reaction wheels' specifications . . . . .	25
3.15	Power unit . . . . .	26
3.16	Onboard computer . . . . .	27
3.17	Inertial measuring unit . . . . .	27
3.18	Balancing system . . . . .	28
3.19	Laser . . . . .	29
3.20	Simulink model . . . . .	30
3.21	Simulation and test models . . . . .	31
4.1	DTrack body frame adjustment . . . . .	35
4.2	CoR identification . . . . .	36
4.3	Inertia tensor identification . . . . .	38
4.4	Thruster identification, method 1 . . . . .	40
4.5	Thruster identification, method 2 . . . . .	40
4.6	Thrust vectors . . . . .	42
5.1	Unwinding example . . . . .	45
5.2	3-DoF test . . . . .	48
5.3	5-DoF test . . . . .	49

*List of Figures*

6.1	PID with anti-windup . . . . .	52
6.2	Pressure-balancing position model . . . . .	53
6.3	Pressure estimation . . . . .	55
6.4	Pressure-balancing position, 3D . . . . .	55
7.1	Combined feedforward + feedback controller. . . . .	58
7.2	Simple pointing . . . . .	60
7.3	Displaced pointing . . . . .	61
7.4	Comparison between simple and displaced pointing problems. . . . .	61
7.5	Pointing correction for non-null displacement. . . . .	64
7.6	Solution set comparison . . . . .	66
7.7	5-DoF closed-loop + feedforward test: attitude reference and results. . . . .	69
7.8	Pointing error . . . . .	70

# Nomenclature

## Abbreviations

AP	Attitude Platform
ART	Advanced Realtime Tracking GmbH
CoG	Center of Gravity
CoR	Center of Rotation
DCM	Direction Cosine Matrix
DLR	Deutsches Zentrum für Luft- und Raumfahrt e.V. (German Aerospace Center)
DoF	Degree of Freedom
FF	Formation Flying
FOG	Fiber Optic Gyroscope
GEO	Geostationary Orbit
GNC	Guidance, Navigation and Control
HCW	Hill-Clohessy-Wiltshire equations
IR	Infrared
IRS	Institut für Raumfahrtsysteme (Institute of Space Systems)
JPL	Jet Propulsion Laboratory
LEO	Low Earth Orbit
LF	Leader Following
LISA	Laser Interferometer Space Antenna
LMI	Linear Matrix Inequality
LP	Lower Platform
LQR	Linear Quadratic Regulator
LSQ	Least Squares

## *List of Figures*

LTI	Linear Time-Invariant
LUT	Lookup Table
MEMS	Microelectromechanical System
MORABA	Mobile Raketenbasis (Mobile Rocket Base)
OBC	On-Board Computer
PID	Proportional-Integral-Derivative
PSU	Power Supply Unit
PWM	Pulse Width Modulation
RCS	Reaction Control System
SAR	Synthetic Aperture Radar
TanDEM-X	TerraSAR-X add-on for Digital Elevation Measurement
TEAMS	Test Environment for Applications of Multiple Spacecraft

### **Greek Symbols**

$\alpha$	Thruster mounting angle about $Z$ body axis
$\beta$	Thruster mounting angle about $X$ or $Y$ body axis
$\phi$	X-axis Euler angle (roll)
$\psi$	Z-axis Euler angle (yaw)
$\theta$	Y-axis Euler angle (pitch)

### **Mathematical Symbols**

$\cdot \subset \cdot$	Strict subset
$\cdot \supset \cdot$	Strict superset

# Chapter 1

## Introduction

### 1.1 Background

Since the beginning of the spacecraft era in the 1950's, the new applications enabled by artificial satellites have never ceased to amaze humanity. From Earth observation to data communications, from global navigation to disaster relief, the uses of space technology have been nothing short of revolutionary.

The high expectations put on space technology have one natural consequence: we have always required more of our space missions, never less. As a result, spacecraft complexity has increased exponentially over the decades (Wertz et al., 2011, p.9); this has brought costs up in all phases of development and operation. Already in the 1980's, the first serious discussions about alternatives to the then-current paradigm started to flourish: for example, Molette et al. (1984) argued that the expected increase in satellite mass would soon overtake launch vehicles' capabilities, and offered alternatives— one of them in the form of a “satellite cluster”. But humanity kept demanding more and more; soon, a launcher's volume and mass limits did not even represent the most stringent limits on spacecraft. Some current mission concepts call for configurations which would simply not be possible to build monolithically with current technology. The LISA scientific mission, for example, requires a triangular laser interferometer spanning millions of kilometers on its sides (Danzmann and Rüdiger, 2003). Because they so significantly transcend the established practices of the field, such missions require a completely new approach.

*Formation flying* is a concept which breaks the monolithic spacecraft paradigm, allowing multiple satellites to cooperate and act in some sense as a single, physically larger spacecraft. Discussions about the concept and the new possibilities it opens have been gaining ground in recent years (Sabol et al., 2001), as the traditionally risk-averse space technology establishment gradually embraces this enabling technology (Bristow et al., 2000). A considerable number of missions including a formation flying component have had a successful lifecycle, and many others are in planning phases (Bristow et al., 2000).

In a general way, for a formation flying cluster to act as an integrated system, common requirements are that the spacecraft should be able to:

- inter-communicate between themselves;
- coordinate experiments together;
- keep position within the formation, especially avoiding collisions.

Most or all of these requirements demand at least that the relative positions of the spacecraft be maintained or changed in some predetermined fashion. This creates novel challenges in the area of space guidance, navigation and control (GNC). A considerable amount of literature has been published on specific FF-related GNC topics: the Hill equations, which govern relative in-orbit motion between two spacecraft (Hill, 1878; Schaub and Junkins, 2009), were extensively studied in the early space era because of the (eventually conquered) rendezvous-and-docking problem (Schweighart and Sedwick, 2002). However, a study by Sabol et al. (2001) points out that the analysis for such a problem is “usually concerned with relatively short time spans”, and that more general tools are needed to analyze formation flying during the whole mission lifetime. Therefore, the open problems in formation flying GNC have attracted considerable scientific and technological interest; particularly, the last 15 years have seen a number of publications on the topic.

In any engineering discipline, and perhaps more so in space-related technologies, it is important for analytical results to be validated by testing. Space GNC problems are clearly no exception; this is motivated by cost, schedule and safety requirements. However, launching and operational costs very often establish in-orbit testing of space technologies as an uneconomical proposition. This gave rise to a plethora of techniques aiming to simulate space systems on the ground.

As defined by Eickhoff (2009, p.10),

“Simulation is an approach for analyzing a dynamic system for gaining an insight to its dynamic behavior. Simulation implies conducting experiments on a model of the system.”

This raises the question: what could be a suitable Earth-bound model for on-orbit satellites, which are mostly subject to force- and torque-free dynamics? For the torque-free half of the problem, one early solution which eventually gained wide acceptance was the use of spherical air bearing systems (Smith, 1965; Schwartz et al., 2003). Single-craft missions generally do not present a pressing need to simulate position displacement, so the force-free half of the issue was not as developed until the relatively recent interest in formation flying. In the last few years, numerous linear air bearing facilities have been introduced (Schwartz et al., 2003), and the technology has become the *de facto* standard for force-free dynamics simulation.

Of course, specialized facility infrastructure is only part of the answer: developing satellite simulation vehicles—the models themselves to which Eickhoff refers—presents many challenges of its own. In the pages that follow, this work aims to contribute to this growing area of research by providing some insight into these challenges. By following the steps taken towards developing a fully functional control system on a real 5-DoF air bearing testing platform, it is expected that the reader will become more acquainted with the tools and techniques of the modern formation flying GNC simulation landscape.

## 1.2 DLR

The work which led to this thesis has been performed at (and supported by) the Institute of Space Systems of the German Aerospace Center, the DLR. The Center’s

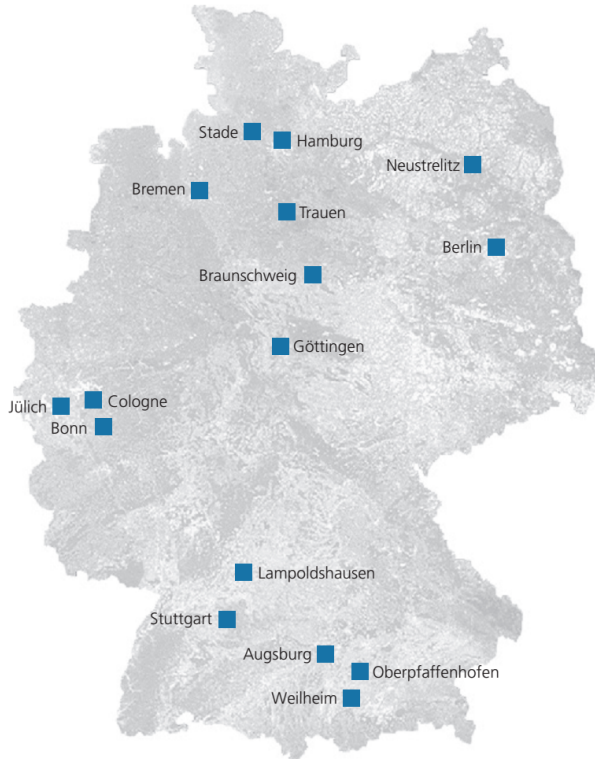


Figure 1.1: DLR locations in Germany (Deutsches Zentrum für Luft- und Raumfahrt e.V., 2014).

mission is most succinctly described in this excerpt:

“DLR, the German Aerospace Center, is Germany’s national research centre for aeronautics and space. Its research and development work in aeronautics, space, energy, transport, defence and security is integrated into national and international cooperative ventures. As Germany’s Space Agency, DLR is tasked with the planning and implementation of Germany’s space programme.” (Deutsches Zentrum für Luft- und Raumfahrt e.V., 2014)

Figure 1.1 shows the location of all DLR sites in Germany. The Institute of Space Systems (Institut für Raumfahrtssysteme— IRS) in Bremen (figure 1.2) has as its main lines of research the development of space systems and mission concepts, and the augmentation of scientific and commercial applications with space components (Deutsches Zentrum für Luft- und Raumfahrt e.V., 2014).

### 1.2.1 Formation flying and the TEAMS facility

DLR has been involved in spacecraft formation flying for years. As an example, the TanDEM-X mission (figure 1.3) uses a relatively conservative approach of a “track-following” tandem pair of spacecraft separated by a distance of hundreds of meters to achieve SAR imaging (Krieger et al., 2007). In other occasions more advanced orbit concepts have been tested, such as in the PRISMA mission, in which the distance

## *Chapter 1 Introduction*



Figure 1.2: Institute of Space Systems, Bremen.

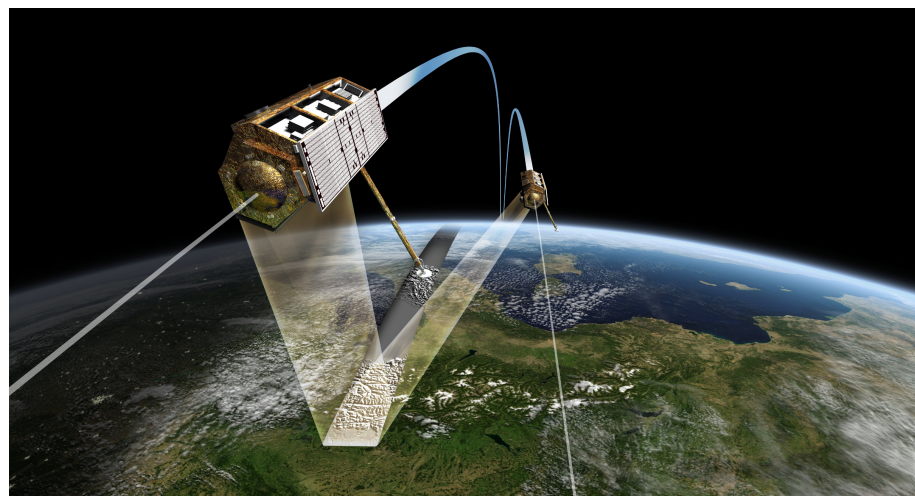


Figure 1.3: Artistic depiction of the TanDEM-X mission performing bistatic SAR imaging (Deutsches Zentrum für Luft- und Raumfahrt e.V., 2009).

between the spacecraft is on the order of a few meters and the relative maneuvering which can be attained is considerably more complex (Delpech et al., 2014; Faller et al., 2012).

In 2008, the TEAMS (Test Environment for Applications of Multiple Spacecraft) facility was built at the Institute of Space Systems. The infrastructure was designed specifically for GNC research in formation flying. According to the DLR web site,

“The main task of the TEAMS facility is to test satellite formation control algorithms on ground. However, sensors for relative attitude and position as well as spacecraft behaviour during berthing and docking maneuvers (contact dynamics) can also be investigated using this facility.” (Deutsches Zentrum für Luft- und Raumfahrt e.V., 2015)

More details about the facility’s capabilities and components are given in section 3.2.

## 1.3 Objectives

The main objective of this work is **to develop a combined attitude and position control system for a formation flying simulation air bearing platform**.

As explained in chapter 3, a number of steps would be required to reach this goal. Therefore, the main objective of this Individual Research Project was broken down into specific objectives thus defined:

- *To create automated procedures for identifying important platform parameters;*
- *To deliver controllers and associated testing procedures which will enable experimentation in higher-level coordinated formation flying algorithms at the facility; and*
- *To create a suitable demonstration for the achieved capabilities of the platform.*

A more detailed justification for this task breakdown can be found in section 3.5, Scope.

## 1.4 Report structure

This work can be roughly divided into two parts: a *preparation* part whose purpose is to situate the reader in the subject, and a *narrative* part where the reader will be guided through the work performed, from the first problem formulations until the final results.

In this introductory chapter— which also opens the preparation part— the importance, means and aim of the work have been described.

In chapter 2, the results of the literature review performed on the subject are described, with the objective of allowing the reader to understand where the current state of the art stands.

Chapter 3, System, gives a comprehensive description of the device to be controlled, as well as of the facility where the work was carried out.

## *Chapter 1 Introduction*

Chapter 4, Parameter identification, marks the start of the narrative part—readers who are already acquainted with the subject may wish to start reading here. This chapter describes the developed procedures for identifying unknown control parameters in the vehicle. The results obtained are presented.

Static control of the vehicle was the first practical stepping stone to the final goal. Chapter 5 presents how this was achieved.

In chapter 6, Balancing, approaches taken for eliminating one of the most important disturbances on torque-free simulations are presented.

Finally, chapter 7 shows how the ultimate goal of combined attitude and position control was achieved, and presents the results.

In chapter 8, Conclusions, the whole process is critically evaluated and, with the benefit of hindsight, some improvements are suggested for future related works.

# Chapter 2

## Literature review

Research into attitude and position control has a long and prolific history; were the full length of this work committed to a literature review of that area, it would not so much as scratch the surface. Therefore, only the studies most directly linked to the problem at hand are reviewed. To complete the picture, a few seminal works which have laid the groundwork for the area are mentioned. Some of the basic mathematics which enables these engineering advances is also presented.

A considerable amount of research has been published on formation flying during the past few decades. In order to put the present work into context, a few papers have been selected which highlight the most commonly faced challenges in control design for formation flying missions.

Spacecraft simulation facilities and devices have been known to exist since the late 1950's, and since the 1960's literature on them is publicly available. For the purpose of establishing a link between literature and the facility on which the work was developed, this review focuses on air bearing simulators.

### 2.1 Formation flying

For some time now, formation flying is set to fundamentally alter the way scientific data are collected (Bristow et al., 2000). Quoting Kapila et al. (2000), “a practical implementation of the [formation flying] concept relies on the control of relative distances and orientations between the participating spacecraft”. Here a distinction has to be made between the commonly confused concepts of *formation* flying and *constellation* flying. Between the two, formation flight is typically considered to require a higher level of autonomy and real-time coordination (Bristow et al., 2000). Because such coordination is generally impossible to achieve without closed-loop control—a main focus of this work—, this review focuses mainly on the challenges of formation flying.

**The rendezvous problem** Although the last 15 years have seen a spate of publications on the general subject, formation flying concepts have been used for quite some time; for example, the final phase of a rendezvous requires the involved spacecraft to fly in close formation— docking or capturing ideally with zero relative velocity—with stringent time constraints (Kapila et al., 2000). The theoretical groundwork for solving the rendezvous problem was first laid out by Hill (1878), at a time when space exploration was yet nowhere in sight. After the 1957 Sputnik-I

launch opened the door to the space era, interest in the subject increased immensely. In 1960, with spaceflight still in its infancy, the famous paper by Clohessy and Wiltshire rediscovered the equations of orbital relative motion, which today are called the Hill-Clohessy-Wiltshire equations (HCW). Later publications developed theories which allowed to loosen some of the restrictions on the original formulations; among them we can highlight for example the article by Yamanaka and Ankersen (2002), which generalizes the rendezvous problem to elliptical orbits (as opposed to the HCW formulation, which assumes near-circular orbits).

**Formation design** The widely-referenced paper by Sabol et al. (2001) presents several FF orbit designs, comparing their relative stabilities when perturbations are taken into account. Fasano and D'Errico (2009) propose an analytical model which is intended to bring the orbit design closer to mission requirements. Yelun (2003), by its turn, studies the motion equations in terms of relative orbital elements instead of a leader-defined coordinate frame; this formulation better suits mission-wide design instead of “local” relative position control problems.

**GNC** In Scharf et al. (2003) and Scharf et al. (2004) extensive surveys of guidance and control techniques applied to formation flying are presented. The 2003 publication deals with both reference trajectory generation and optimal open-loop control design, while the 2004 one deals with control design techniques and stability results. There we find a definition for formation flying which is rooted basically on GNC aspects. According to the authors, FF is defined as “a set of more than one spacecraft whose *dynamic states are coupled through a common control law*” (Scharf et al., 2003, 2004, emphasis in original source).

Because of the strict level of control demanded by some FF applications, some degree of autonomy may be required which goes beyond what traditional control system architectures provide. Beard et al. (2001) discuss a hierarchical subsumption architecture which allows both centralized and decentralized control. They demonstrate it by analyzing a space interferometer mission similar to LISA (Danzmann and Rüdiger, 2003). Bauer et al. (1997) offer an autonomous control architecture capable of housing many different control algorithms. Still focusing on autonomy, Ferguson et al. (2002) take a data-centric approach to testing coordination algorithms by interconnecting individual computers which act as networked satellites; an external computer integrates the equations of motion to perform orbit propagation.

Robertson et al. (1999) divide the formation flying discipline into *formation keeping*, which “initializes the desired formation and maintains it against disturbances” and *formation planning*, which “creates trajectories for the formation to follow during maneuvers such as re-sizing or re-targeting” (Robertson et al., 1999). Thus, formation keeping identifies most with the control discipline and formation planning naturally falls under the “guidance” label. According to the needs of the specific mission which is their study case, distributed control architectures are presented and analyzed.

Some works, like those by Schlotterer and Novoschilov (2012) and Camp et al. (2004), use potential fields for guidance and control, leveraging the fact that linear air bearing platforms are holonomic. Section 2.2 offers more information into these

platforms.

Mesbahi and Hadaegh (2001) concern their study with the feasibility of certain control paradigms within the most common formation flying methodology, the leader following (LF) approach.

**Fractionated spacecraft** A more radical approach to formation flying is the fractionated spacecraft concept, discussed by Brown and Eremenko (2006). In that paper, the authors take a mostly economic approach for analyzing the viability of selecting between a monolithic or a fractionated architecture. Nevertheless, technical challenges are also looked into, and the possibilities that the widespread utilization of fractionated spacecraft could bring are discussed. The much earlier publication by Molette et al. (1984), among the very first on the subject, follows a similar vein. In it the authors analyze the economics of a monolithic and a fractionated concept, although in a much narrower context—the specific use case of GEO communications spacecraft—and without considering any other far-reaching effects of the technology.

## 2.2 Satellite simulators

The simulation of torque-free dynamics poses considerable practical difficulties, and is a task not to be taken lightly (Kim et al., 2003). A considerable amount of literature has been published on the challenges it entails.

**Air bearing facilities, vehicles** One of the first reviews of air bearing simulation facilities was the paper by Smith (1965), which described both commercial and scientific installations of the time. Fosth (1967) and Moran and Dishman (1970) also give their accounts of early systems meant for testing of, respectively, a lunar orbiter and a space telescope. In more recent times, the article by Schwartz et al. (2003) compiles an extensive list of contemporary and historical facilities. Some of the main scientific air bearing facilities mentioned in modern literature are located at the Naval Postgraduate School, Monterey, CA (Agrawal and Rasmussen, 2001; Schwartz et al., 2003; Schwartz, 2004; Romano, 2005; Kim and Agrawal, 2006; Chesi et al., 2014); Jet Propulsion Laboratory (JPL), Pasadena, CA (Beichman et al., 2006; Keim et al., 2006); and Georgia Institute of Technology, Atlanta, GA (Jung and Tsiotras, 2003; Schwartz et al., 2003; Schwartz, 2004; Cho et al., 2009). Yang and Cao (2006) give an account of a modern air bearing facility in China.

A great deal of previous research on formation flying has focused on the utilization of 5-DoF vehicles. There have been a few 6-DoF simulation systems, like the one described by Nolet (2007), but even those normally are tested on a more conventional 3-DoF testbed at some stage (Chung et al., 2005). Viswanathan et al. (2012) proposes a 6-DoF vehicle with a more conventional approach. Choset et al. (1999) describe using a 3-DoF air bearing setup for autonomous guidance algorithm testing for a 6-DoF robot.

Although air bearing facilities are mostly used for GNC simulation of satellites, Leite Filho et al. (1999) document an air bearing application for launch vehicle

## DISTURBING TORQUES ON AN AIR-BEARING PLATFORM

I TORQUES ARISING FROM PLATFORM	III TORQUES FROM ENVIRONMENT
STATIC UNBALANCE	AIR DAMPING
DYNAMIC UNBALANCE	AIR CURRENTS
ANISOELASTICITY	MAGNETIC FIELDS
MATERIAL INSTABILITY	VIBRATION
STRESS-TEMPERATURE-HUMIDITY-	RADIATION PRESSURE
EVAPORATION	
GRAVITY GRADIENT	ELECTRICAL WIRES TO BASE
EQUIPMENT MOTION	MASS SHIFT IN BEARINGS
SOLENOIDS-RELAYS	AND LOOSE FITS
	BATTERY DISCHARGE
II TORQUES FROM BEARING	REACTION JET SUPPLY DIS-CHARGE
AERODYNAMIC TURBINE EFFECT	
EXHAUST AIR IMPINGEMENT	REPLACEMENT OF COMPONENTS

Figure 2.1: Main sources of disturbance torques on air bearing platforms (Smith, 1965).

testing. The DLR's Mobile Rocket Base (MORABA) also has a similar air bearing facility for sounding rocket testing (Stamminger et al., 2013).

**Disturbances** Smith (1965) lists many of sources of disturbing torques (figure 2.1). Group I disturbances are mainly dependent on the construction of the platform, and can (mostly) be compensated for. Those from group II, however, are related to the construction of the air bearing and mitigation of their effects can be quite complex (Smith, 1965). Wilcock (1965) describes in detail how imperfections on the bearing sphere result in disturbances. Group III are environmental disturbances whose elimination, although possible, is normally cost-prohibitive; some industrial facilities even place the system inside a vacuum chamber (Smith, 1965). Group IV torques arise from the use of the platform, and some of them can also be compensated for (see chapter 6, Balancing).

Balancing the platform to avoid gravity torques is a common theme in publications. Although some works, like those by Schwartz (2004) and Ustrzycki et al. (2011), mention the use of manual balancing, there seems to be a consensus in the literature that automated balancing procedures are required for any kind of useful precision to be achieved (Smith, 1965). Some of the works which describe automated balancing come from Chesi et al. (2014), Kim and Agrawal (2009), Kim and Agrawal (2006), and Hatcher and Young (1968).

A stiff construction of the platform is necessary to avoid gravity torques from anisoelastic effect disturbances; advanced facilities put a great amount of effort into minimizing this (Smith, 1965). Figure 2.2 shows an early (1959) air bearing platform where stiffened rib construction is evident.

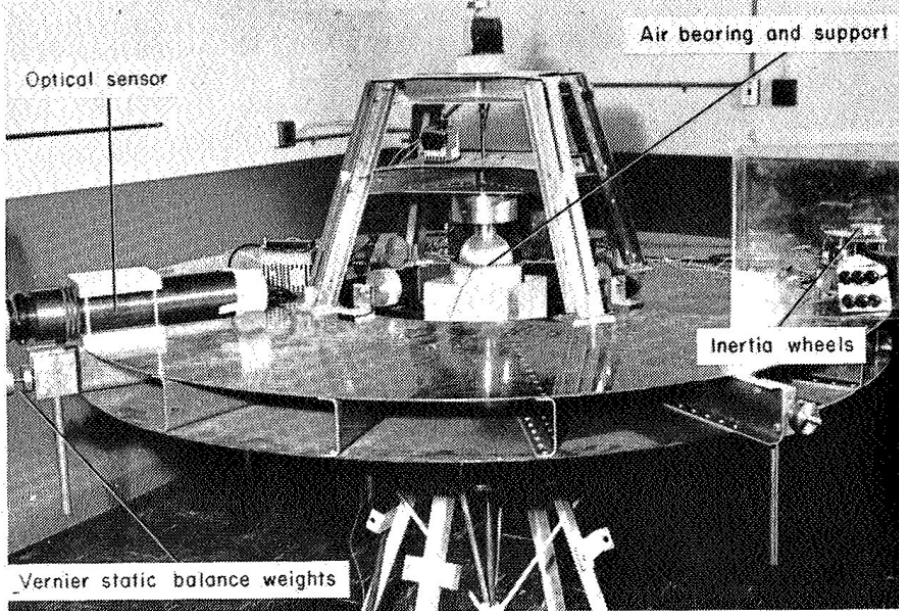


Figure 2.2: Early air bearing platform at Ames Research Center in 1959, showing a stiffened rib design (Smith, 1965).

## 2.3 Attitude

As will be discussed in chapter 5 (Static control), attitude control systems design is intimately linked to the attitude representation selected. Choosing a suitable representation may at first sight appear to be a simple task, but a quick perusal of the literature shows this not to be the case: Shuster (1993) presents an extensive survey of different attitude representations, totaling 12 different types—or 41 if all variants are counted.

The group of all rigid rotations about the origin of  $\mathbb{R}^3$  is called the 3-dimensional *special orthogonal group*, or  $\text{SO}(3)$ ; the group operation is transformation composition. As such rotations are linear transformations on  $\mathbb{R}^3$ , they can be *identified* with the  $3 \times 3$  real matrices of determinant 1, with matrix multiplication acting as the group operation. The identity matrix  $\mathbf{I}$  is the neutral element, and the inverse element of element  $\mathbf{R}$  is its transpose  $\mathbf{R}^{-1} = \mathbf{R}^T$  (Chaturvedi et al., 2011; Shuster, 1993). Because  $\text{SO}(3)$  has a smooth manifold structure and its group operation (including the inverse) is a smooth map, it is also a Lie group (Lee, 2012), endowed with a Lie algebra  $\mathfrak{so}(3)$ . This Lie algebra consists of the tangent space of  $\text{SO}(3)$  at the identity element, and can be identified with the group of  $3 \times 3$  real skew-symmetric matrices (Chaturvedi et al., 2011).

The importance of the word “identified” on the second sentence of the preceding paragraph can’t be stressed enough.  $\text{SO}(3)$  has a one-to-one, topologically equivalent correspondence with rigid body rotations, so it can be used to represent those rotations in an unrestricted manner; the properties of one are the properties of the other. However, the members of  $\text{SO}(3)$  have a total of 9 parameters, making them unwieldy to manipulate, and their physical representation is quite often non-intuitive.

The fact that all columns of a rotation matrix are unitary and mutually orthogo-

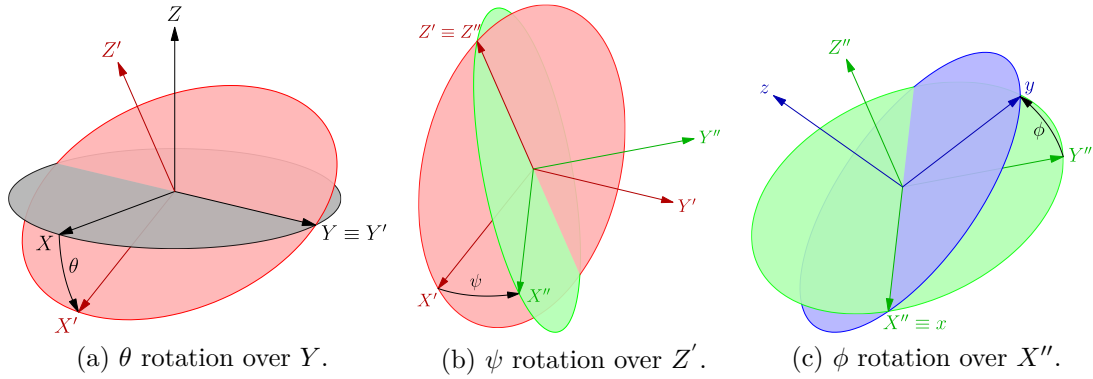


Figure 2.3: Euler angles example (2-3-1 sequence).

nal to each other (6 constraints) points to the possibility of the existence of simpler representations, which is indeed true. A well-known example are *Euler angles*, which is a 3-dimensional class of representations comprising 12 different possible sets (Sidi, 1997). An Euler angle transformation comprises 3 successive rotations over body-referenced axes (Shuster, 1993). Figure 2.3 illustrates this with a so-called 2-3-1 sequence of rotations. Euler angles are used mostly because they are a user-friendly representation for rotation data, and because of their obvious advantage of minimum dimensionality (Shuster, 1993). Nevertheless, a series of shortcomings limits their use in numerical models or analytical studies. For one, they are a non-global representation—that is, some configurations in  $\text{SO}(3)$  have no correspondence for a particular set of Euler angles. This can be mitigated by keeping two different sets for the representation; however, the low dimensionality advantage is lost this way. Also, as Shuster (1993) mentions, “the great disadvantage of three-dimensional representations (...) is the nonlinear nature of their composition rule, which leads also to a nonlinear kinematic equation”. This shortcoming is shared with all other minimal representations (Stuepnagel, 1964).

A non-minimal representation which has many advantages is the *unit quaternion* (Shuster, 1993). Notwithstanding their being commonly misunderstood, sometimes frowned upon, and occasionally even reviled (Altmann, 1989), the fact stands that quaternions are the ideal representation for digital rigid-body attitude simulations (Shuster, 1993). Quaternion space is isomorphic to the real 3-sphere  $\mathbb{S}^3 \subset \mathbb{R}^4$ —that is, a quaternion  $\mathbf{q}$  has 4 parameters  $q_1, q_2, q_3, q_4$  with the restriction that  $\|\mathbf{q}\| = 1$ . In relation to minimal representations, like the Euler angles, quaternions have two crucial advantages:

- they are endowed with a bilinear composition rule and, as a result, a linear kinematic equation (Shuster, 1993); and
- they are a global attitude representation, valid over the entire set of rigid rotations in  $\mathbb{R}^3$  (Chaturvedi et al., 2011).

However, in the last point the relation is not one-to-one: quaternion space  $\mathbb{S}^3$  double-covers  $\text{SO}(3)$ , in that any two quaternions  $\mathbf{q}, -\mathbf{q}$  represent the same rigid body attitude. Therefore, although global, quaternions are not a unique representation.

## *Chapter 2 Literature review*

The preceding paragraphs appear to raise a question: is it possible to have a global and unique representation of attitude with just 3 parameters? Sadly, the answer is no: Stuelpnagel (1964) shows this by means of a topological argument. How many parameters are required, then, to achieve that objective?

Some studies make use of 2 columns of the direction cosine matrix, in the form of a 6-element vector, as a representation for attitude (Stuelpnagel, 1964). This can easily be shown to be homeomorphical to the special orthogonal group  $\text{SO}(3)$ : since rotation matrices are orthogonal and mandatorily have a real eigenvalue equal to +1, the third column of the rotation matrix could be reconstructed uniquely from the other two. This is still not the most economical 1-to-1 parametrization of  $\text{SO}(3)$ , though. In fact, Hopf (1940) (as cited by Shuster, 1993; Stuelpnagel, 1964) has shown the minimum required number of parameters for that to be 5. As the composition rule for such a representation is nonlinear, it is of limited practical usefulness (Shuster, 1993).

# Chapter 3

# System

The complexity of air bearing vehicles and associated facilities can vary immensely, from the relatively simple to the exceedingly complex. Their capabilities range from very small academic projects made from COTS components to large, vacuum-domed industrial facilities built with nothing but space-graded parts. However small or large, they are most commonly a means to an end; accordingly, a profound understanding of the system is required for it to bring the results one expects.

In this chapter, the infrastructure of the TEAMS facility will be explained, and details will be presented about the plant to be controlled—the TEAMS\_5D vehicle. This groundwork will allow us to, in later chapters, analyze the system and propose solutions which enable the achievement of the laid-out goals.

## 3.1 Conventions

The global coordinate system is a right-handed coordinate system in which the  $Z$  axis is anticollinear to the local gravity vector  $\mathbf{g}$ . The  $X$  axis points along the “long” side of the granite table, from the compressed air filling station side towards the other side of the room (see facility description on section 3.2). The  $Y$  axis completes the right-hand-rule system. The origin is positioned on the top near corner of the division between the two granite blocks (refer to figure 3.1 for orientation). When clarification is necessary as to what system is being used, vectors represented in this system carry a left superscript  $g$ .

The body-fixed coordinate system is also a right-hand-rule system, fixed to the attitude platform. The attitude quaternion is defined to be  $[ 0 \ 0 \ 0 \ 1 ]^T$  when this system’s orientation coincides with that of the global coordinate system. The origin is defined to lie on the center of the air bearing’s sphere. When clarification is necessary as to what system is being used, vectors represented in this system carry a left superscript  $b$ .

Whenever Euler angles are mentioned, it shall be implicit that a  $Z \rightarrow Y \rightarrow X$  sequence ( $\psi \rightarrow \theta \rightarrow \phi$ ) was used.

## 3.2 Facility

This section describes the main components of the TEAMS facility at the Institute of Space Systems in Bremen. In many aspects TEAMS follows the modern norm in

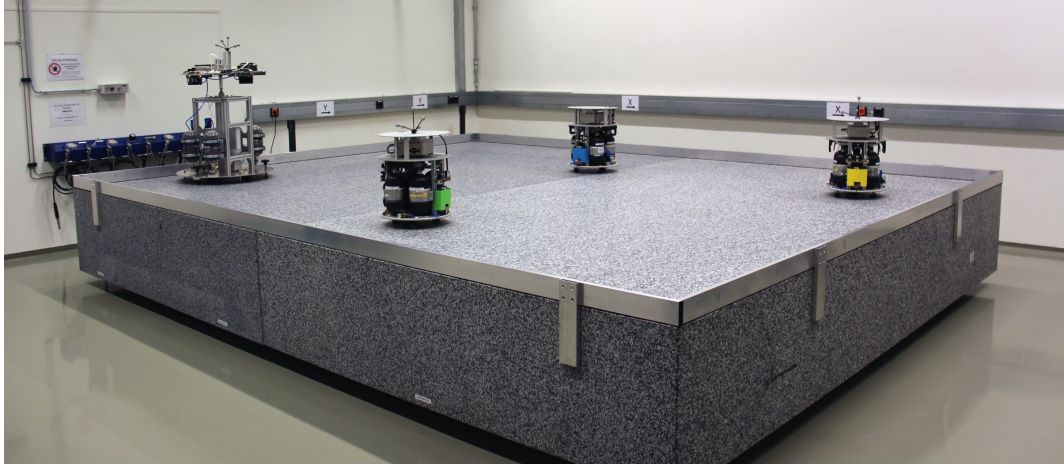


Figure 3.1: Granite table experiment area, populated with various test vehicles.

air bearing simulation facilities around the world. For example, Cho et al. (2009) describe in detail a similar facility for 5-DoF simulations.

### 3.2.1 Granite table

The facility's main arena for experiments is the granite table area, illustrated in figure 3.1. Two granite tables of 4 m by 2.5 m each are joined together to provide a total experiment area of 4 m by 5 m. The tables have a flatness of  $3 \mu\text{m}$ , with less than  $20 \mu\text{m}$  edge-to-edge deviation from the horizontal and less than  $10 \mu\text{m}$  deviation from table to table (Schlotterer and Novoschilov, 2012). Such smoothness is required for the objective of simulating a force-free environment in two degrees of freedom as faithfully as possible. A metallic rail is fixed to the boundaries of the table area, protecting the air bearing vehicles.

### 3.2.2 Optical tracking

Optical tracking and navigation systems are commonly used in satellite simulator facilities because they enable non-contact position and/or attitude sensing. This is important to avoid disturbances in the force- and torque-free simulation environment. An example is the ad-hoc optical navigation system for an air bearing table described by Wu et al. (2014).

The TEAMS facility uses an optical system called DTrack, from the German company Advanced Realtime Tracking GmbH. The system as deployed comprises six networked near-IR cameras equipped with synchronized IR flashing capability, a central controller, and passive targets composed of retroreflective markers. A typical camera for the system is shown in figure 3.3.

When a marker is in view of more than one camera, its position within the measurement space is calculated from the intersection of the pointing rays from each camera. Figure 3.2 shows an illustration of this process. The targets are composed by a number of markers, and different targets (identified by a unique name in the software) each have a different marker structure—that is, the positions of the mark-

### Chapter 3 System

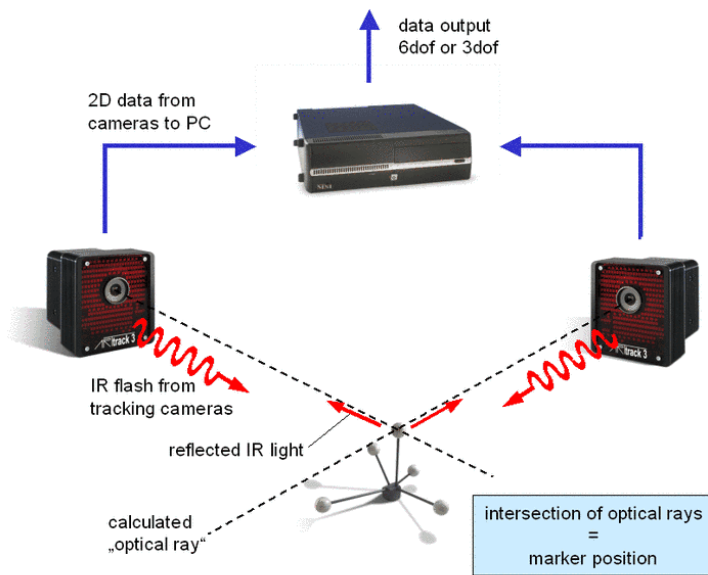


Figure 3.2: How the DTrack system works (Astro- und Feinwerktechnik Adlershof GmbH, 2015).



Figure 3.3: DTrack optical infrared tracking camera (Advanced Realtime Tracking GmbH, 2013).

### Chapter 3 System

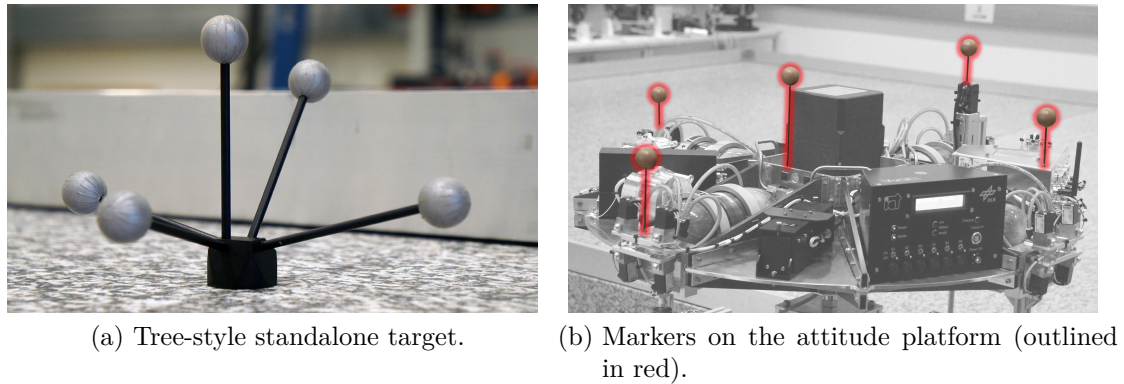


Figure 3.4: DTrack reflective targets.

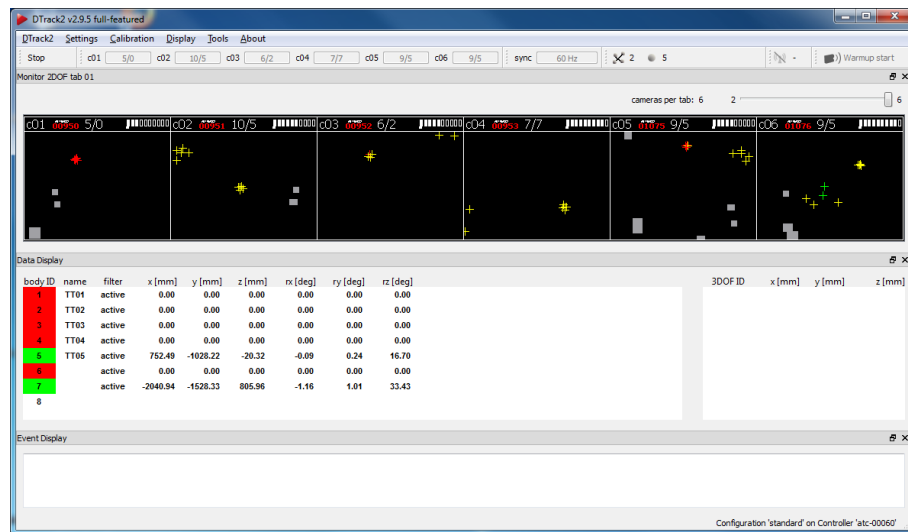


Figure 3.5: DTrack user software, main view.



Figure 3.6: Compressed air station: compressor and flow controls, pressure gauges, and filling nozzles.

ers within the local target reference frame are fixed for any given target, but vary from target to target. Figure 3.4 shows an example of a standard target and a target created by placing individual markers on top of the simulation vehicle.

The controller has the capability to obtain the positions and attitudes of many targets simultaneously, identifying each one, at a maximum update rate of 60 Hz. Figure 3.5 illustrates the user software environment, running in the control room's computer. This information can also be sent through the laboratory's network: in the TEAMS facility, the navigation data flow reaches the vehicle in real-time through a wireless network connection.

### 3.2.3 Compressed air system

As will be detailed in section 3.3, the simulation vehicles have onboard compressed air bottles for actuation and for running the air bearings. Accordingly, the laboratory has a specialized compressed air system for the purpose of safely filling these bottles up to a pressure of 300 atm. The compressor and high pressure external reservoir are located outside the experiment room, for increased safety. The filling station is illustrated in figure 3.6.

### 3.2.4 Control room

The control room is a separate room within the floorplan of the laboratory, adjacent to the experiment area, which contains the DTrack system controller and the host computer. The host computer is equipped with software tools which enable the operator to run different control models on the vehicles. A large glass window allows the operator to visualize the experiment area.



Figure 3.7: Control room with main computer and DTrack controller.

### 3.3 Plant

The object to be controlled is a vehicle of the TEAMS\_5D type (Schlotterer and Novoschilov, 2012). The overall vehicle comprises a *lower platform* (LP) which glides over the experiment area on air cushions, and an *attitude platform* (AP) which sits on top of a spherical air bearing connected to the lower platform. The vehicle is depicted in figure 3.8. This configuration is well explored in the literature: Cho et al. (2009), Keim et al. (2006), Viswanathan et al. (2012), Schwartz et al. (2003) and Schwartz (2004) all describe similar systems.

The attitude platform uses an “umbrella” configuration (Schwartz et al., 2003). This allows complete freedom of movement in yaw. Pitch and roll excursion are limited to around  $\pm 30^\circ$  each.

In this work, the upper rotating part will be referred to as “attitude platform” or simply as “the platform”, the lower part as “position platform” and the composition of both as a functional 5-DoF unit will commonly be referred to as “the vehicle”. In the next subsections, each major subsystem is described.

#### 3.3.1 Air bearings

The main components responsible for the creation of a force- and torque-free environment are the air bearings attached to the lower platform, illustrated on figure 3.9. The spherical air bearing cup is a hemispherical cavity, smoothly finished to a high tolerance. It is made of a porous material through which compressed air is injected into the cavity. A matching sphere is fixed to the attitude platform; when the bearing is assembled and provided with compressed air, a thin air film holds the weight of the attitude platform and constrains its linear displacement while causing (ideally) no reaction torques whatsoever.

The linear air bearings on the bottom of the lower platform perform an equivalent function for displacement. They consist of smoothly finished pads, also provided

### *Chapter 3 System*

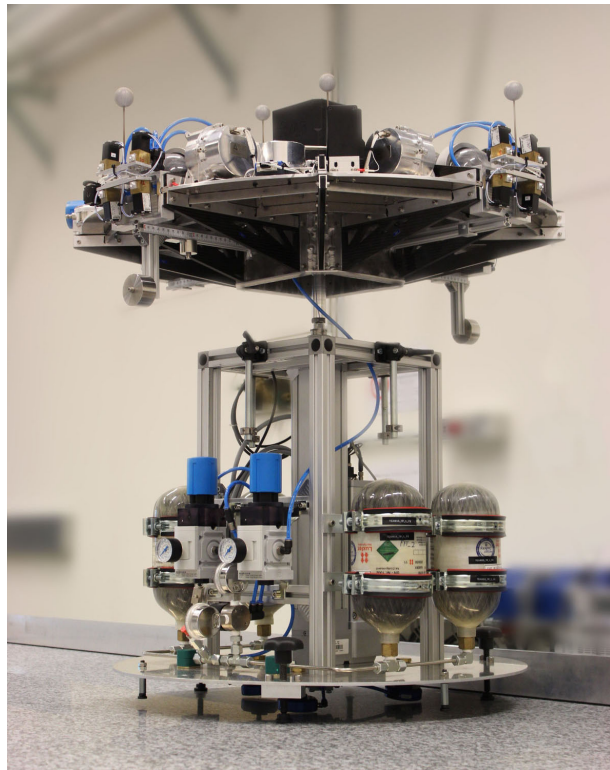
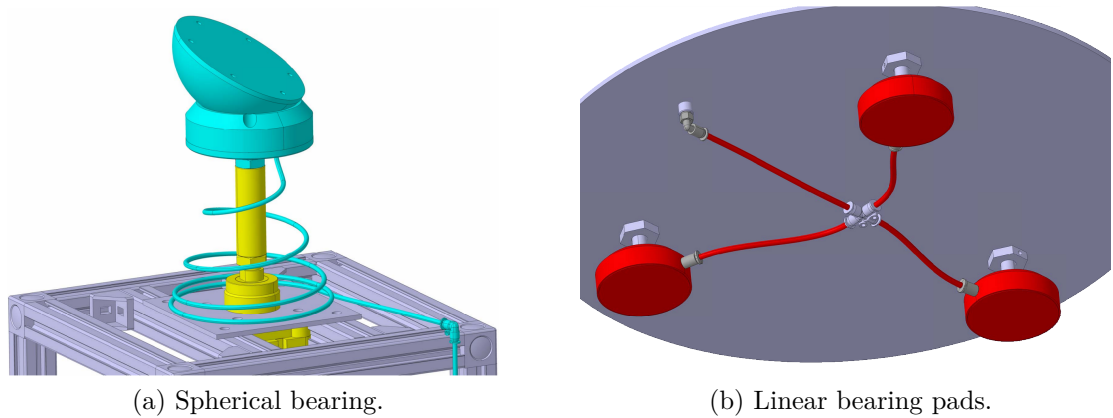


Figure 3.8: TEAMS\_5D vehicle.



(a) Spherical bearing.

(b) Linear bearing pads.

Figure 3.9: CAD drawings of the lower platform air bearings.

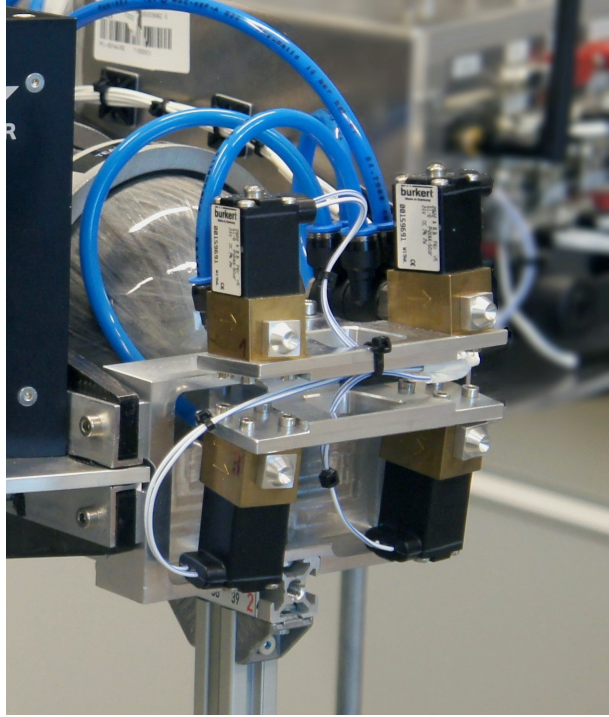


Figure 3.10: The attitude platform has 16 cold gas thrusters in groups of 4;  $+Y$  group is pictured.

with a series of small holes. The compressed air creates a thin film between the pads and the highly polished granite table, constraining only its linear displacement in the  $Z$  axis (parallel to the gravity vector) and causing no reaction forces on the  $X$  and  $Y$  axes. Because there are 3 pads in total, they also constrain torques on the  $X$  and  $Y$  axes, while leaving  $Z$ -axis angular movement unimpeded.

### 3.3.2 Cold gas thrusters

The attitude platform is equipped with a reaction control system (RCS) composed of 16 cold gas thrusters. The nozzles are grouped in 4 sections of four thrusters each, at the  $+X$ ,  $-X$ ,  $+Y$  and  $-Y$  sides of the platform. Each group is structurally the same as all others, only differing in position and direction. Inside each group, the thrusters are each angled from the main central reference axis by angles  $\pm\alpha$  and  $\pm\beta$ , as illustrated in figure 3.11. This allows the thruster system to simultaneously apply arbitrary torques and forces to the attitude platform. Each thruster is capable of generating a maximum force of around 0.06 N, and can be individually throttled by pulse width modulation (PWM), on a 2 kHz modulation frequency, from 0 % to 100 % in 256 steps. The resulting thrust curve is highly nonlinear; therefore, the control models apply a lookup table (LUT) to the signal for output linearization.

Crouch (1984) uses nonlinear geometric control to study the controllability of spacecraft with a number of actuator configurations. The study confirms that three noncollinear pairs of gas jets, or three noncollinear momentum exchange devices, are enough to guarantee controllability.

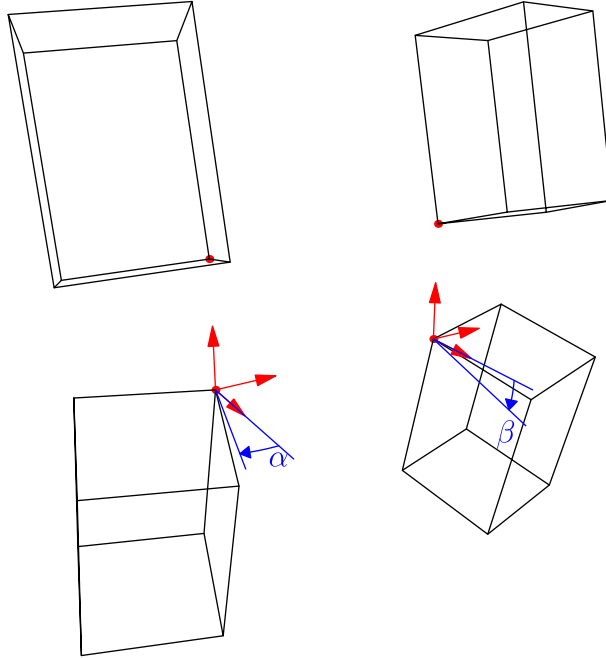


Figure 3.11: Each block is composed by four thrusters, angled from the centerline (here  $\alpha$  and  $\beta$  are exaggerated for visualization).

### 3.3.2.1 Thruster allocation

As is commonly found in the literature (Cho et al., 2009; Jung and Tsiotras, 2003; Ledebuhr et al., 2001), the thrusters' positions and directions are fixed in the body frame by construction. This means some mapping must be used that, given arbitrary desired force and torque vectors as inputs, the outputs are the individual thrusters' *settings* to match the desired actuation:

$$M : \mathbb{R}^3 \times \mathbb{R}^3 \rightarrow \mathbb{R}^{16} \quad (3.1)$$

Such a mapping must also behave in a convenient manner when the desired actuation lies outside its output space. All of this starts to not look as such a trivial task if we take into account all the required details: for one, thrusters are not bidirectional (i.e., they act in “forward” but not in “reverse”), which in and of itself is a major complicating factor. A more accurate mapping representation is, then,

$$M : \mathbb{R}^3 \times \mathbb{R}^3 \rightarrow \{(x_i \mid 0 \leq x_i \leq 1, 1 < i < 16) \in \mathbb{R}^{16}\} \quad (3.2)$$

where the range  $[0; 1]$  represents 0 % to 100 % thrust. What's more, generally speaking the solution to a given allocation problem is not unique. In general, different mappings may give different outputs for the same input, even if all constraints are respected. This is easy to see for the particular case of this vehicle: because of its symmetry, if the thrusters are all set at the same thrust level (for example), no net forces or torques will be produced on the platform. Clearly, such a vector belongs to the null space of the “inverse mapping”<sup>1</sup>

$$N : \{(x_i \mid 0 \leq x_i \leq 1, 1 < i < 16) \in \mathbb{R}^{16}\} \rightarrow \mathbb{R}^3 \times \mathbb{R}^3 \quad (3.3)$$

---

<sup>1</sup> $N$  represents the actual physical effect of the thruster settings on the platform; as such, it's determined by the laws of physics and obviously can't be freely chosen.  $M$ , on the other hand,



Figure 3.12: Pressure regulators and gauges for the onboard compressed air system. The refilling nozzle (lower left) is also shown.

so that this setting vector can be added to any other, without altering the actuation vectors (provided the boundaries of the space are respected). This makes it clear that another deciding factor must be used: for example, we can choose a mapping which is the most economical in terms of “fuel” (pressurized gas) spent (Durham, 1993; Tang et al., 2011).

Most commonly, such a mapping is realized by an algorithm. For instance, Cho et al. (2009) describe the use of linear programming to solve the control allocation for a similar vehicle; Servidia and Pena (2005) use a subgradient optimization formulation. In the case of the TEAMS\_5D vehicle, the individual thruster settings are controlled by a real-time convex optimizer called CVXGEN, described by Mattingley and Boyd (2012). In the words of its authors, “CVXGEN takes a high-level description of a convex optimization problem family, and automatically generates flat, library-free C code that can be compiled into a high speed custom solver for the problem family” (Mattingley and Boyd, 2012). The obtained optimizer function receives as inputs the requested force and torque and outputs individual thruster settings that correspond as closely as possible to that which was requested. If the output can’t precisely follow the input, the convex program reduces the actuation magnitude but keeps the same actuation direction. A secondary directive is to minimize the air flow, which—besides allowing the platform to run longer—solves the nonuniqueness dilemma.



Figure 3.13: One of the reaction wheels (depicted next to a 1 Euro coin for size reference).

### 3.3.3 Compressed air system

The vehicle has two separate air systems: one for the lower platform and one for the attitude platform. The LP air system supplies the spherical and linear bearings, while the AP air system supplies the thrusters. Apart from that, both systems are very much the same: through a common distribution line four 300 atm air bottles supply a high pressure regulator, which drops the air pressure to around 8 atm. A second, higher-accuracy regulator reduces again the pressure to about 6 atm. From there, the thrusters (in the case of the AP) or the bearings (LP) are directly supplied. Figure 3.12 shows a section of the attitude platform's system.

### 3.3.4 Reaction wheels

In addition to the thrusters, 3 reaction wheels are installed for supplementary torque actuation. Manufactured by the German company Astro- und Feinwerktechnik Adlershof GmbH, these space-rated actuators are capable of supplying a maximum 0.015 Nm torque; maximum angular momentum capability is 0.36 Nms. It is important to highlight its very low maximum torque deviation is only  $6 \cdot 10^{-5}$  Nm. For its well-known characteristics, the reaction wheels are used for identifying certain parameters on the platform (see chapter 4, Parameter identification). An overview of the reaction wheel specifications is displayed on figure figure 3.14.

---

is an arbitrary mapping between the two vector spaces concerned— so it's not necessarily true that  $N_b^{-1} \supset M$ , although we certainly would like it to be. Here,  $N_b$  is some convenient bijective subset of  $N$ — because of the null space phenomenon,  $N$  itself is clearly noninvertible.

Parameter	RW 90
angular momentum	0.36 Nms @ 7800 rpm
nominal rotation speed	6000 rpm
max. rotation speed	ca. 7820 rpm
resolution	0.12 rpm (1 LSB)
speed deviation – rms value <sup>1</sup>	0,26 rpm
speed deviation – max. value <sup>1</sup>	$\pm 0,96$ rpm
nominal torque (max. commandable)	0.015 Nm
torque deviation – rms value <sup>2</sup>	$< 2 \cdot 10^{-5}$ Nm
torque deviation – max. value <sup>2</sup>	$< 6 \cdot 10^{-5}$ Nm
mass	< 0.9 kg
moment of inertia (rotating mass)	$4.5 \cdot 10^{-4}$ kgm <sup>2</sup>
supply voltage	18 V to 24 V
power consumption stand by (motor off)	< 1.2 W
conservation of nominal rotation speed <sup>3</sup> max. <sup>3</sup>	< 3.5 W < 17 W
operation temperature range	-20°C to +50°C
storage temperature	-30°C to +60°C
operation lifetime	2 years in low earth orbit
storage time	1 year (incl. 240 h of ground operation)

1...value determined in OMEGA\_STRAT (PI-controller) → conservation of 6000 rpm, steady state

2...value determined in DEOMEGA\_ADAPT (state controller) → const. acceleration, steady state

3... values determined at ambient temperature (~23 °C), vacuum and power mode 4

Figure 3.14: Specifications for the reaction wheels (Astro- und Feinwerktechnik Adlershof GmbH, 2008).



Figure 3.15: Each of the switches on the power unit (depicted) controls power flow to a certain part of the system.

### 3.3.5 Power subsystem

The power subsystem supplies all the other subsystems through a power supply unit (PSU), shown in figure 3.15. The PSU also serves as a charge/discharge unit for the onboard rechargeable lithium batteries. A frontal connector on the PSU allows the operator to connect a 25.2 V supply line for battery charging. The onboard batteries can keep the system supplied for at least 2 hours.

### 3.3.6 Onboard computer

The onboard computer (OBC) centralizes the entire control and data flow of the platform. The PC-104 format motherboard houses a x86-architecture processor and 1 GB of RAM. Figure 3.16 shows the computer within its enclosure, together with the many connectors required to communicate with the other subsystems.

### 3.3.7 Inertial measuring unit

The attitude platform has an inertial measuring unit (IMU) attached to it and connected to the onboard computer. Manufactured by the German company iMAR, the iVRU-FC uses fiber optic gyroscopes and MEMS accelerometers as its inertial sensors.

In the torque-free environment of space, a spacecraft's movement is purely inertial, corresponding to a double-integrator system. It follows that the dynamics do not depend on the angular displacement; therefore, it's impossible to stabilize the platform's angular displacement by simple positional feedback—a derivative term (or equivalent) is required. Although the DTrack system provides the vehicle's position and attitude to a high precision, instantaneous angular velocity information

### Chapter 3 System

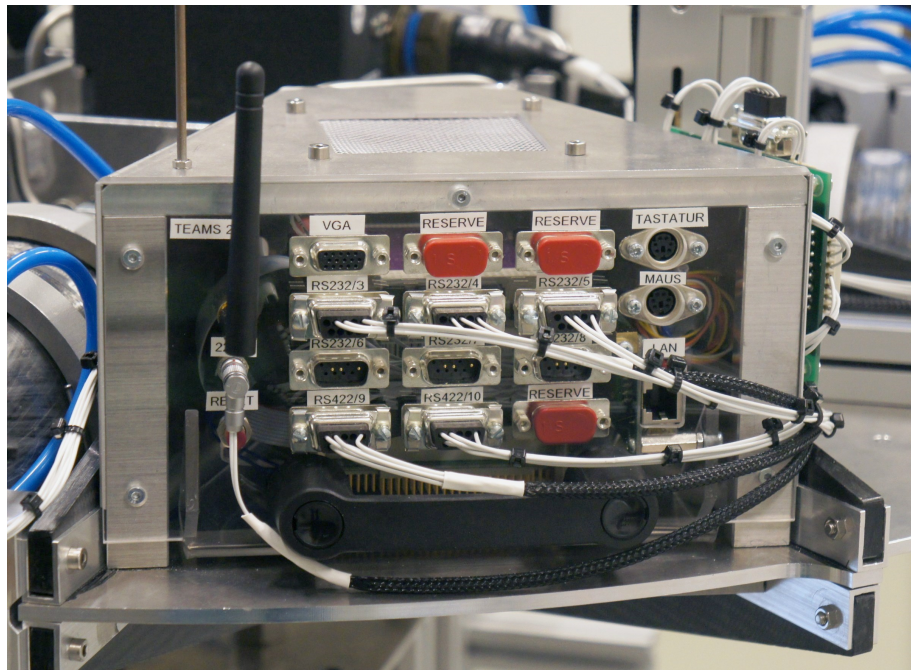


Figure 3.16: The vehicle's onboard computer.

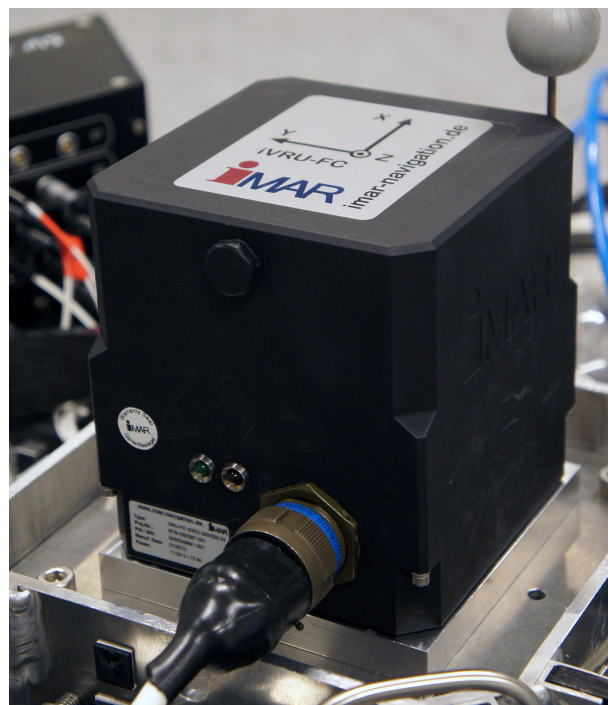


Figure 3.17: Inertial measuring unit attached to the attitude platform.

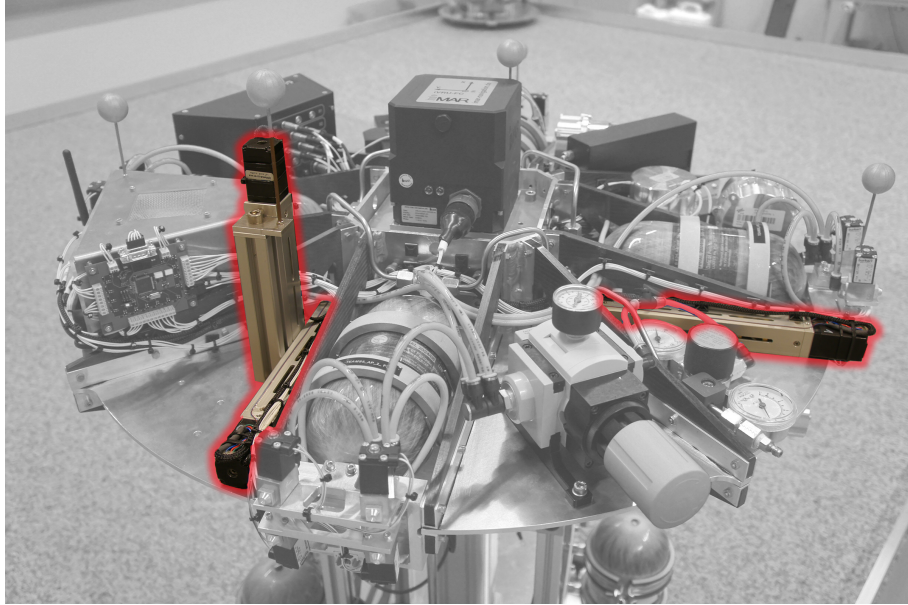


Figure 3.18: Balancing system for the attitude platform. Note the 3 independent actuation axes.

must be obtained by some other process— either direct numerical differentiation or a state observer<sup>2</sup>. Inertial sensors, on the other hand, can supply that information directly.

### 3.3.8 Balancing system

To maintain an environment as free as possible from torques, it becomes necessary to avoid gravity-related disturbance torques. To this end, it is imperative to make the attitude platform’s center of gravity (CoG) and the spherical bearing’s center of rotation (CoR) coincide. The balancing system is an actuator which makes it possible to displace the platform’s center of gravity by the precise linear movement of metallic weights.

There are three separate actuation systems, one for each platform axis. Each one is composed by a 100 g brass weight mounted to a spindle; the spindle is turned by a step motor connected to one of its ends. This arrangement allows the onboard computer to move each weight independently, with sub-millimeter precision. Their location on the attitude platform is illustrated on figure 3.18.

More details on the balancing procedures can be found in chapter 6.

### 3.3.9 Laser

The attitude platform is equipped with a laser diode for pointing purposes. Its power is supplied directly by the platform’s power subsystem and can be manually turned on and off by a front panel switch.

---

<sup>2</sup>Salcudean (1988) shows that attitude information is all that is required to construct a stable observer for  $\omega$ .

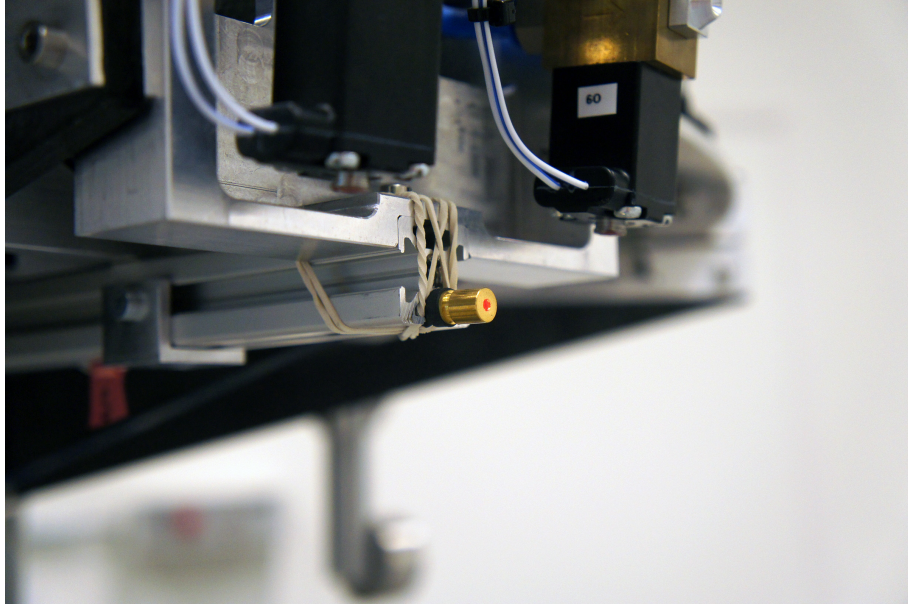


Figure 3.19: The laser diode is attached to the attitude platform.

### 3.4 Simulink

For the vehicle as described to perform its intended activities, its onboard computer must run a program which should be responsible, at a minimum, for the following tasks:

- getting navigation information and parameter values from the wireless network;
- communicating with the onboard sensors (IMU gyro and accelerometer, reaction wheel RPM sensors) and reading their information;
- running a control algorithm which will determine actuator output signals;
- communicating with the actuators and sending the outputs to them;
- sending telemetry data to the wireless network.

Additionally the host computer must show telemetry data to the operator and perform tasks on this data, such as analyses, persistent recording, among others.

There are many ways in which such a scheme could be implemented. At the TEAMS facility, the chosen solution was to use MATLAB and Simulink<sup>3</sup> models. Such models, containing control blocks for the vehicle, can be modified as desired. At run time, the Simulink Coder package on the host computer automatically generates equivalent C code for the Simulink models; the cross-compiled binary is uploaded through the wireless network to the platform's onboard computer, where it runs in real-time. During the test, bidirectional communication ensures that both telemetry data is sent back to the host computer and automatically presented in Simulink, and model parameters which get modified in the host computer are updated in the OBC.

---

<sup>3</sup>MATLAB® and Simulink® are registered trademarks of The Mathworks, Inc.

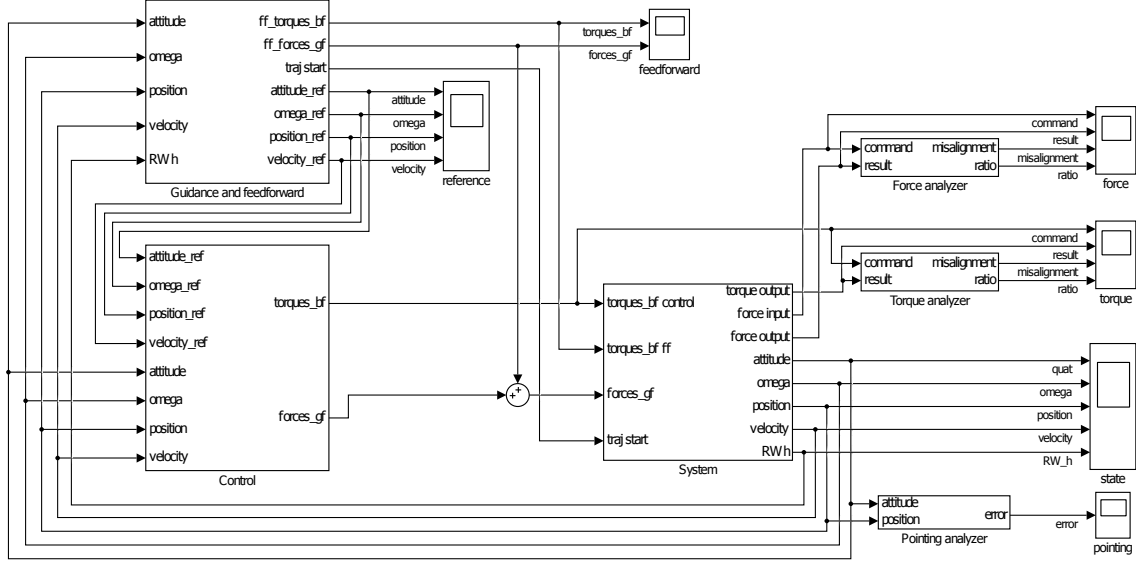


Figure 3.20: Top-level Simulink model for the 5-DoF pointing experiments.

## 3.5 Scope

With the vehicle and facility satisfactorily introduced, it's possible to convey how the system was to be found at the start of the work, and the drawn objectives.

### 3.5.1 Initial state

At the start of the work, the hardware subsystems for the 5-DoF simulation vehicle were completely developed and physically integrated—although the AP and the LP, the two main constituent parts of the vehicle, had not yet been joined, they could be separately tested. The onboard computer's real-time operating system was integrated, and wireless communication between the platform and the host computer was working. There was already a process in place for uploading programs from the host computer to the platform's OBC. Simulink libraries were available which took care of the low-level interfacing between the OBC and the platform components.

### 3.5.2 Final desired state

The platform had been physically integrated, but in this process there are a lot of tolerances involved. Some of these tolerances affect parameters which directly influence its control characteristics—for example, thruster force direction and magnitude. Thus, these important platform parameters were still considered unknown.

As mentioned, the low-level libraries represented different subsystems inside the vehicle already existed, and had been tested on smaller vehicles (Schlotterer and Novoschilov, 2012), but they were still not glued together to form a coherent whole—in other words, an actual computational model of the platform was needed. Moreover, attitude and position control on the 5-DoF vehicles were still to be achieved before the platform would have any actual usefulness. After the achievement of these milestones, a demonstration of the capabilities of the platform would be desirable;

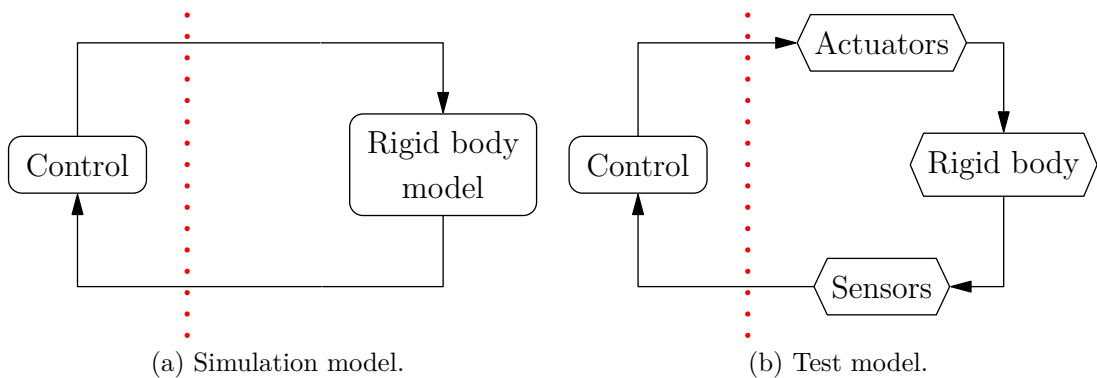


Figure 3.21: The change to a computational rigid body model is automatic.

therefore, the platform should be commanded to actually do something useful and/or impressive in itself, to show that with the control system in place the platform is more than just the sum of its parts.

A number of steps would be required to reach the top-level goal. Therefore, the main objective of this Individual Research Project was broken down into specific objectives mentioned in the Introduction chapter and repeated here:

- To create automated procedures for identifying important platform parameters;
  - To deliver controllers and associated testing procedures which will enable experimentation in higher-level coordinated formation flying algorithms at the facility; and
  - To create a suitable demonstration for the achieved capabilities of the platform.

### 3.6 Methodology

From the start, it was decided that the best way to achieve the required goals in the limited time available was to use a high degree of automation. Automating all aspects of testing procedures—from replacing simulation blocks with real subsystem blocks when needed to recording and archiving testing results—was fundamental to improve repeatability, accelerate data analysis and increase testing cadency.

It is convenient that the models used for purely digital simulation are precisely the same ones used for testing. This enables a direct comparison of the results from both. By its turn, such comparison helps validate the model, and allows a significant share of parameter tuning to be done in pure simulation. As simulation can be run significantly faster than real-time, this speeds up the whole process.

Now one is faced with the question: how can a simulation model and a test model be the same, if one is purely digital and the other trades information with physical reality? The answer is to limit the differences between them to a small and well-defined *interface*.

This interface separates what is physically present in the system—rigid-body dynamics, actuators, sensors—from the glue logic and algorithms. This way, physical

parts can be seamlessly replaced by computational models during simulation, leaving the main logic untouched. This certainly requires that simplifying assumptions are made, and that such models are validated separately—but their simplicity makes it straightforward to do so. After this relatively small price has been paid, the model can be used in rather complex simulations, and their results can be trusted to be as close to reality as the assumptions we made.

To achieve this, variant model blocks are used in Simulink. These blocks contain two or more internal component blocks with a common input/output interface. At runtime, the component block to be used is selected by a logic expression. This way, for example, a given model block can contain two component blocks—one is used when a `simulation` boolean flag is true, and the other is used when the flag is false. This makes it easy to automate the back-and-forth between simulation and testing, and enables a direct comparison between simulation results and test results. All resulting data is stored, and can be subsequently analyzed and post-processed. As the input parameters are stored together with the results, a test can be re-ran in the same original software environment if the results appear suspicious.

### 3.7 Dynamics, kinematics

The familiar notion of a 6DOF body can be identified with an object which lives in the configuration space  $\text{SO}(3) \times \mathbb{R}^3$  (Koditschek, 1988). In this respect, all considerations made in this work shall refer only to the attitude platform. While the lower platform contributes translational inertia and has an extra degree of freedom (rotation over the  $Z$  axis), it has no actuators or sensors, and it is assumed that its center of gravity lies directly below the center of the spherical air bearing. Therefore, it is considered not to contribute anything to the rotational dynamics.

Translational dynamics follow the classical equation

$$\mathbf{f} = m\ddot{\mathbf{x}} \quad (3.4)$$

and are considered to happen only in two dimensions.

In relation to attitude, Bhat and Bernstein (2000) remind us that the Lie group structure of  $\text{SO}(3)$ —with its associated Lie algebra  $\mathfrak{so}(3)$ —allows us to write the rigid body equations of motion on the vector bundle  $\text{SO}(3) \times \mathbb{R}^3$  directly. The equations (Bhat and Bernstein, 2000) are

$$\begin{aligned}\dot{\mathbf{R}} &= -(\boldsymbol{\omega}^\times)\mathbf{R} \\ \mathbf{t} &= \mathbf{I}\dot{\boldsymbol{\omega}} + (\boldsymbol{\omega}^\times)\mathbf{I}\boldsymbol{\omega}\end{aligned}$$

where  $\mathbf{I}$  is the real, symmetric, positive-definite inertia tensor

$$\mathbf{I} = \begin{bmatrix} I_{xx} & I_{xy} & I_{xz} \\ I_{xy} & I_{yy} & I_{yz} \\ I_{xz} & I_{yz} & I_{zz} \end{bmatrix} \quad (3.5)$$

and  $\mathbf{R} \in \text{SO}(3)$ ,  $\boldsymbol{\omega}^\times \in \mathfrak{so}(3)$ .  $\boldsymbol{\omega}^\times$  is linked to the angular velocity vector  $\boldsymbol{\omega} \in \mathbb{R}^3$

### Chapter 3 System

(Chaturvedi et al., 2011) by the isomorphism

$$\boldsymbol{\omega}^{\times} \equiv \sum_{k=1}^3 \epsilon_{ijk} \omega_k = \begin{bmatrix} 0 & \omega_3 & -\omega_2 \\ -\omega_3 & 0 & \omega_1 \\ \omega_2 & -\omega_1 & 0 \end{bmatrix} \quad (3.6)$$

where  $\epsilon_{ijk}$  is the *Levi-Civita symbol*, defined as  $\epsilon_{123} = \epsilon_{231} = \epsilon_{312} = 1$ ,  $\epsilon_{132} = \epsilon_{213} = \epsilon_{321} = -1$ , 0 otherwise (Shuster, 1993).

For the interested reader, Cho et al. (2009) obtains the equations of motion for a similar vehicle by an analytical mechanics standpoint. Also, Cho et al. (2001) develop the rotational equations of motion for a rigid body testbed with provisions for “auxiliary bodies which deform or move relative to the base body”. This has a direct correspondence with the TEAMS\_5D vehicle’s balancing system.

# Chapter 4

## Parameter identification

In the manufacturing processes of the platform’s components, such as the thrusters, there are inaccuracies involved. Moreover, the platform assembly process also has inaccuracies of its own. This contrasts with the high level of accuracy required in the determination of parameters such as the magnitude and direction of thruster forces, or the platform’s inertia tensor. The physical tolerances involved mean the mechanical design documents alone are unable to supply us with that information.

A solution to this is determining the unknown parameters by devising a procedure for the vehicle’s operation which will conveniently expose these parameters—or a known function of the parameters—in some way through telemetry data. This is called a *parameter identification procedure*. A considerable amount of literature has been published on this topic. For example, Keim et al. (2006), Bergmann et al. (1987), Kim and Agrawal (2006), and Tanygin and Williams (1997) describe methods for parameter identification applied to vehicles in experimental facilities. Lee and Wertz (2002) even describe a method applied to a real spacecraft during its mission.

It is conceivable also that, as components age, their characteristics will change. For example, the thrusters’ control valves are electromechanical systems: the opening range and switching velocity characteristics might drift over time, interfering on the PWM process and altering the thrust. Therefore, it’s in our scientific best interests that such procedures be *automated*. Automation reduces the human resources required to run the procedure, as well as increases repeatability by minimizing the effect of one of the most common experimental error sources: human intervention.

With all this in mind, identification procedures were devised in order to satisfy the precision requirements for each identified parameter. This chapter will explain such procedures.

### 4.1 Center of rotation

As explained in the previous chapter, the DTrack system determines the attitude and position of a given coordinate system within the measuring volume by calculating the position of individual reflective markers. For its factory-built “tree-style” targets, information about the position of the origin of the local coordinate frame with respect to the markers is already built into the software, and no further calibration is needed. The attitude platform, on the other hand, uses a system with five custom-placed markers (refer back to figure 3.4b). This is so that the markers can be as spaced from each other as possible, which improves attitude determination accuracy.

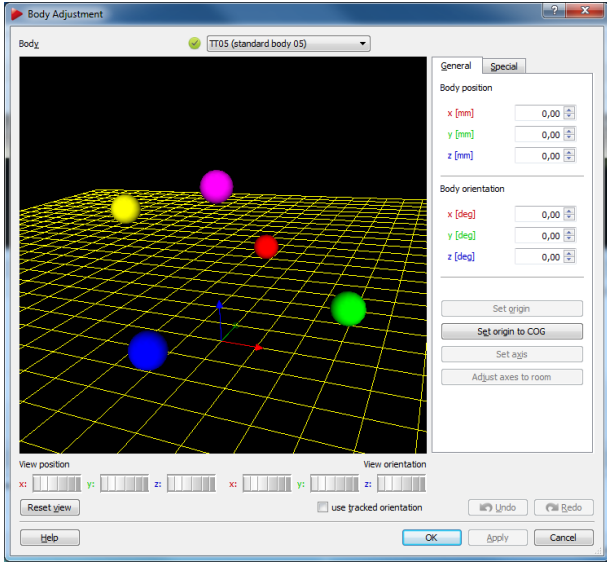


Figure 4.1: DTrack user software, body frame adjustment.

A custom system like this must first be properly calibrated in the DTrack software before being used (figure 4.1). First the body and global (room) coordinate frames were aligned in attitude by a laborious manual procedure, leaving the origin position to be adjusted. The software initially put the frame origin on the centroid of the markers, which was quite far from the bearing’s center of rotation where it should lie.

To solve this, a least squares (LSQ) problem was formulated (Lawson and Hanson, 1974). Consider  $\mathbf{T}_k$  the instantaneous  $3 \times 3$  direction cosine matrix for the body frame’s attitude in relation to the global frame, and  $\mathbf{p}_k$  the body frame’s position in the global frame. Both are updated by the DTrack system at each of the  $n$  recorded timesteps. Consider also that  $\mathbf{1}$  is the  $3 \times 3$  identity matrix,  $\mathbf{r}$  is the position of the current body frame origin in relation to the center of rotation, and  $\mathbf{b}$  is the position of the air bearing in the global frame. A least squares estimate is then obtained for  $\mathbf{r}$  and  $\mathbf{b}$  by minimizing the 2-norm of the residual

$$\boldsymbol{\varepsilon}_c = \underbrace{\begin{bmatrix} \mathbf{T}_0 & \mathbf{1} \\ \mathbf{T}_1 & \mathbf{1} \\ \vdots & \vdots \\ \mathbf{T}_n & \mathbf{1} \end{bmatrix}}_{3n \times 6} \cdot \underbrace{\begin{bmatrix} \mathbf{r} \\ \mathbf{b} \end{bmatrix}}_{6 \times 1} - \underbrace{\begin{bmatrix} \mathbf{p}_0 \\ \mathbf{p}_1 \\ \vdots \\ \mathbf{p}_n \end{bmatrix}}_{3n \times 1} \quad (4.1)$$

The data to be input into this problem was collected by manually pitching, rolling and yawing the platform in a variety of ways while maintaining its position fixed and letting the DTrack system capture the attitude and position. Figure 4.2 shows the recorded position of the (displaced) body frame as the platform went through those motions.

The results were used to calibrate the body frame position in the software. Subsequent tests showed that a similar motion did not produce any position displacement; therefore, the body frame origin coincides with the center of rotation.

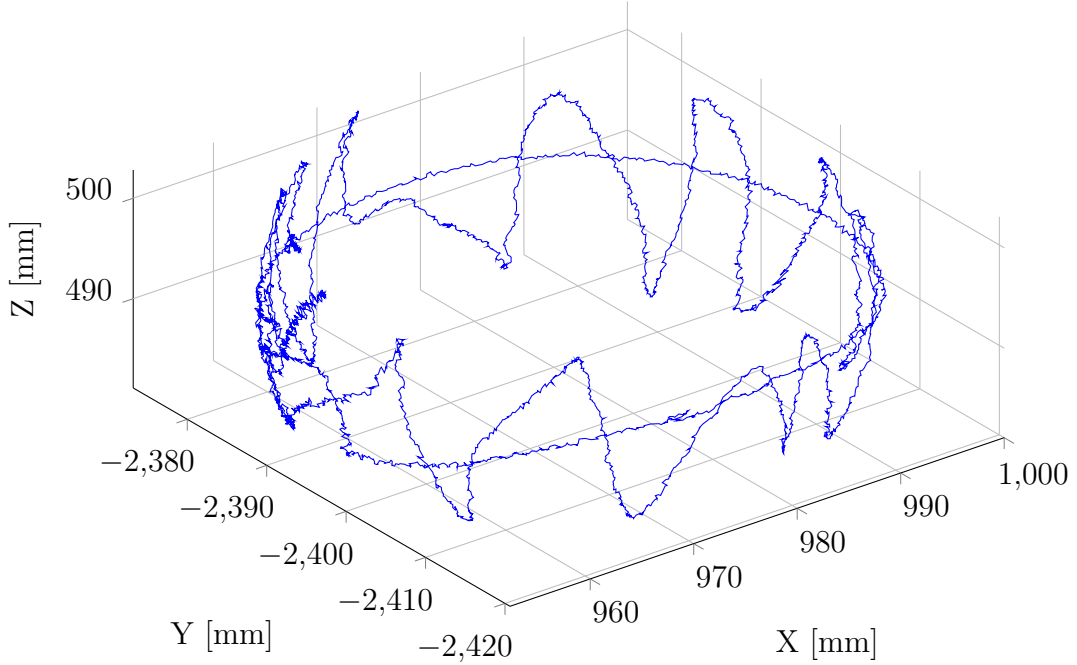


Figure 4.2: Path of the displaced body frame origin during data acquisition in global frame coordinates.

## 4.2 Inertia tensor

A reliable identification of the inertia tensor is necessary to guarantee simulation results will be as faithful as possible. It's also essential for getting a good performance out of the control system, by allowing us to correctly calculate the gains.

For this, the solution was also to use a least squares procedure. Consider Euler's equation on a momentum-biased rigid body (Sidi, 1997)

$$\mathbf{t} - \mathbf{t}_w = \mathbf{I}\dot{\boldsymbol{\omega}} + \boldsymbol{\omega} \times (\mathbf{I}\boldsymbol{\omega} + \mathbf{h}_w) \quad (4.2)$$

where  $\mathbf{h}_w$  is the reaction wheels' stored momentum and  $\mathbf{t}_w$  their commanded torque. Here the external torque  $\mathbf{t}$ —mainly from air bearing disturbances and aerodynamic drag—is considered negligible. Isolating the inertia tensor components, for any timestep we can calculate the residual

$$\boldsymbol{\varepsilon}_i = \begin{bmatrix} \dot{\omega}_x & -\omega_y\omega_z & \omega_y\omega_z & \dot{\omega}_y - \omega_x\omega_z & \dot{\omega}_z + \omega_x\omega_y & \omega_y^2 - \omega_z^2 \\ \omega_x\omega_z & \dot{\omega}_y & -\omega_x\omega_z & \dot{\omega}_x + \omega_y\omega_z & \omega_z^2 - \omega_x^2 & \dot{\omega}_z - \omega_x\omega_y \\ -\omega_x\omega_y & \omega_x\omega_y & \dot{\omega}_z & \omega_x^2 - \omega_y^2 & \dot{\omega}_x - \omega_y\omega_z & \dot{\omega}_y + \omega_x\omega_z \end{bmatrix} \cdot \begin{bmatrix} I_{xx} \\ I_{yy} \\ I_{zz} \\ I_{xy} \\ I_{yz} \\ I_{xz} \end{bmatrix} + \mathbf{t}_w \quad (4.3)$$

In a similar fashion to the method used in the previous section,  $n$  timesteps can be taken into account by expanding the matrices downwards with the additional timestep information—making the number of rows  $3n$ —, and applying the LSQ

procedure by minimizing the 2-norm of the resulting  $3n \times 1$  residual vector. The components  $\dot{\omega}_x$ ,  $\dot{\omega}_y$ ,  $\dot{\omega}_z$  are obtained by numerical differentiation.

The quality of the obtained results and the uncertainty of the output parameters in this calculation depends significantly on the data fed into the model. For example, if the maneuvers manage to excite movement on a certain axis much less than the others, it's likely that its related inertia components will have a higher uncertainty—although the many cross-products between the angular velocity components alleviate this a bit, coupling the factors and making it less likely that information for any one axis will be much weaker than for the others.

The chosen sequence of identification maneuvers is as follows. The platform starts with zero pitch and roll angles—we'll call this the *attitude origin*. A “U-shaped” open-loop bipolar torque command (approximately 20 seconds total duration) is sent to one of the reaction wheels; afterwards, a closed-loop phase<sup>1</sup> brings the platform back to the attitude origin. The process is then repeated on a different axis, until all 3 have been tested. Figures 4.3a and 4.3b illustrate an actual test: in the first figure the commanded reaction wheel torque is shown, while on the second one the resulting angular velocity is displayed.

One important point of this procedure is that we use only timesteps where the premises are good enough. For example, if the platform hits a stop, the “no external torques” assumption will not hold anymore. Therefore, it's necessary to post-process the time history and discard timesteps where the approximations are not good. It's important also that such a post-processing be automatic, to prevent the operator from biasing the data.

For collisions against the stops, the developed code detects this by setting limits on the second time derivative of  $\boldsymbol{\omega}$  (angular jerk). If those limits are hit, a few timesteps before and after the collision are discarded. Also, because of issues in the communication bus between the reaction wheels and the onboard computer, the reaction wheels have a time delay in responding to torque commands. Therefore, a few timesteps are discarded after a reaction wheel has been sent a new command.

### 4.2.1 Results

The final inertia tensor result is

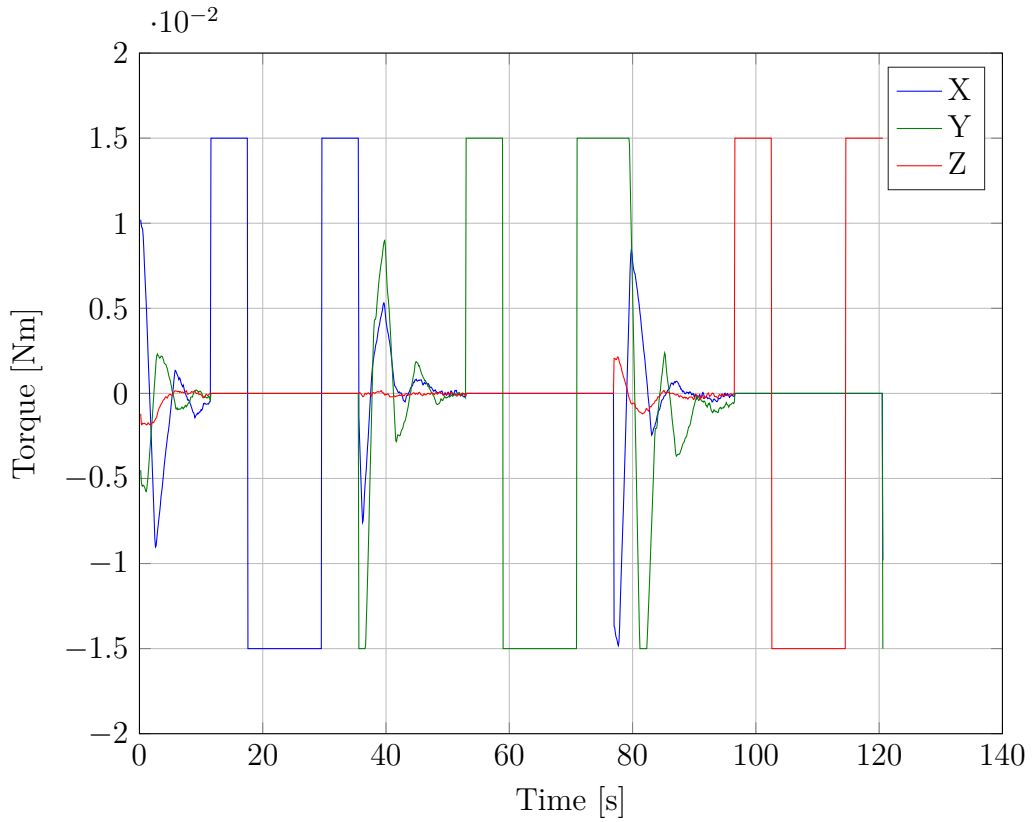
$$\mathbf{I} = \begin{bmatrix} 2.13 & -.03 & .00 \\ -.03 & 1.89 & -.03 \\ .00 & -.03 & 3.61 \end{bmatrix} \pm (.05) \text{ Nms}^2 \quad (4.4)$$

For comparison, before completion of the identification an approximated inertia model was used in which the attitude platform was represented by a 50 kg cylinder. The resulting inertia tensor was, then,

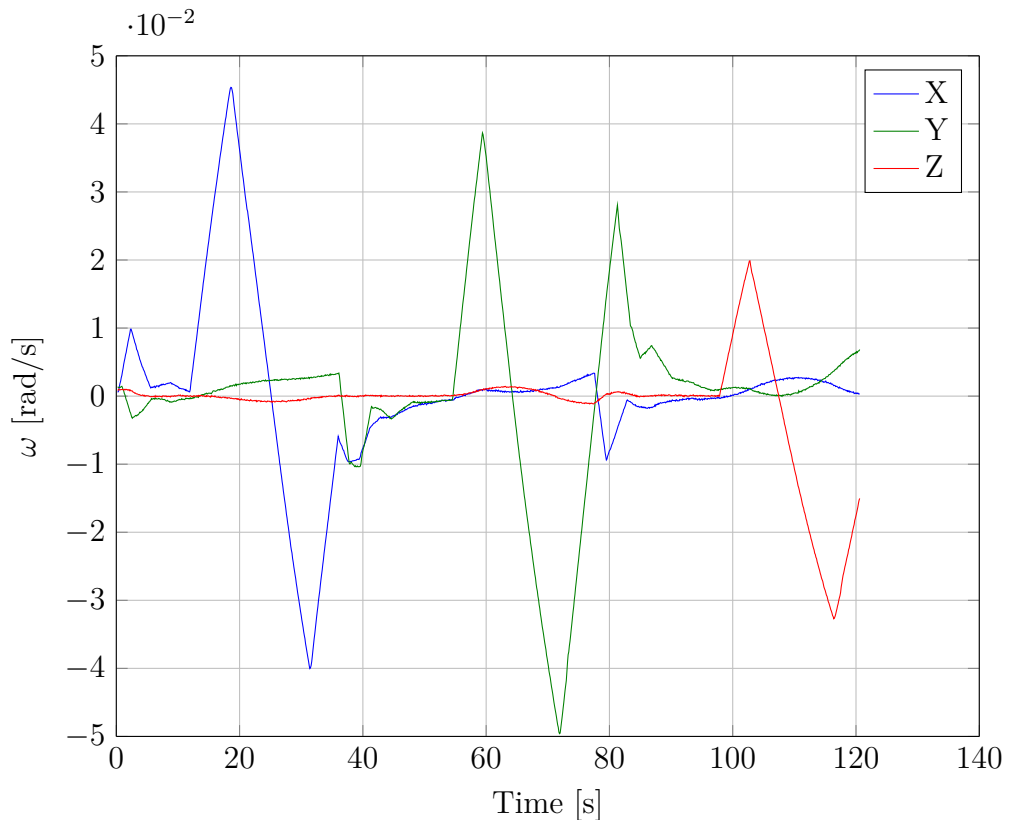
$$\mathbf{I} = \begin{bmatrix} 2.57 & 0 & 0 \\ 0 & 2.57 & 0 \\ 0 & 0 & 4.62 \end{bmatrix} \text{ Nms}^2 \quad (4.5)$$

---

<sup>1</sup>See chapter 5, Static control, for details on the control loop.



(a) Reaction wheel torque.



(b) Angular velocity.

Figure 4.3: Data from an inertia tensor identification procedure.

As the air mass varies, the inertia tensor will also vary over time. To determine the maximum extent of this effect, an approximate calculation for the air mass inertia was done, and is shown in appendix A. The maximum inertia of the air mass is determined to be very small—less than 4% of the principal axis inertia for each axis—and was, as an approximation, disregarded.

### 4.3 Thruster torque

The identification of the torque vectors for each thruster is fundamental to assure the control allocation strategy will work as intended<sup>2</sup>. Similarly to the inertia tensor, discrepancies between model and reality affect the performance of the system. Contrary to what we have seen in the previous section, though, here if the discrepancies are too large they may severely affect the system's stability. For example, if the torque vector for a certain thruster is inverted between the model and the real platform (a very severe discrepancy indeed), it's possible that a stable pole will become unstable. This will happen only for certain torque demands sent to the control allocator, which will undoubtedly make problem diagnostic/debugging very difficult.

To identify thruster torque direction and magnitude, two different identification methods were compared. In the first method—henceforth called *method 1*—, the thruster to be identified is set to maximum; all the others are set to 0%. The attitude platform, thus, runs free under the action of that single thruster for a determined time, while its motion data is recorded. Angular velocity data for such a test is illustrated in figure 4.4. Then, similarly to the inertia tensor identification, Euler's equations are used to assemble a least squares problem. In this case, we want simply to minimize the 2-norm of the residual

$$\varepsilon_t = \mathbf{I}\dot{\boldsymbol{\omega}} + \boldsymbol{\omega} \times (\mathbf{I}\boldsymbol{\omega}) - \mathbf{t} \quad (4.6)$$

where  $\mathbf{t}$  is the unknown torque we are identifying.

In the second method (henceforth to be called *method 2*), the thruster to be identified is likewise set to maximum for a determined time while all others are kept turned off. This time however we prevent the platform from turning, using the reaction wheels in a closed control loop (PI velocity regulator) to hold the platform static under thruster action. This is maintained for a determined time, enough for the system to reach a steady state. After steady-state is reached, the thruster torque can simply be read out as the opposite of the control effort torque. Figure 4.5 illustrates a typical test. The advantage of this method when compared to method 1 is that the closed loop keeps  $\boldsymbol{\omega}$  null, so the inertia tensor does not influence the result at all; we therefore trade inertia tensor uncertainty for reaction wheel output uncertainty, which is relatively smaller. It also eliminates the need for estimating  $\dot{\boldsymbol{\omega}}$ .

---

<sup>2</sup>For the very same reason, a complete identification of the thrusters' force vectors would be extremely important. The possibility of including that task into the scope of this work was considered; nevertheless, because of time constraints, this was pushed into the realm of future work.

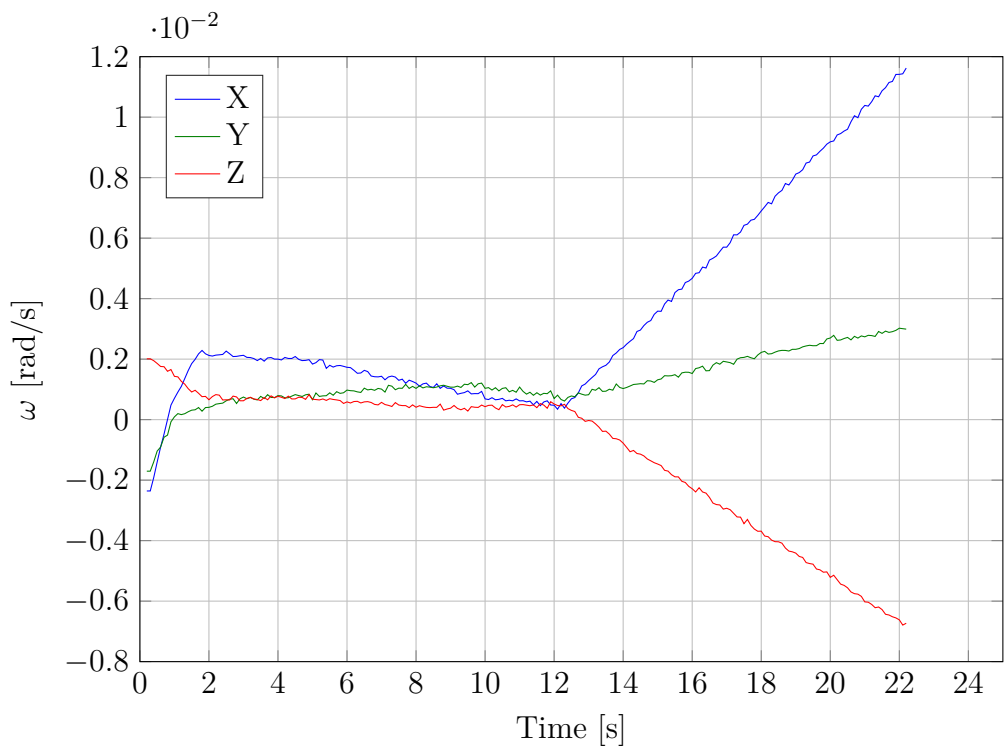


Figure 4.4: Angular velocity during method 1 thruster identification.

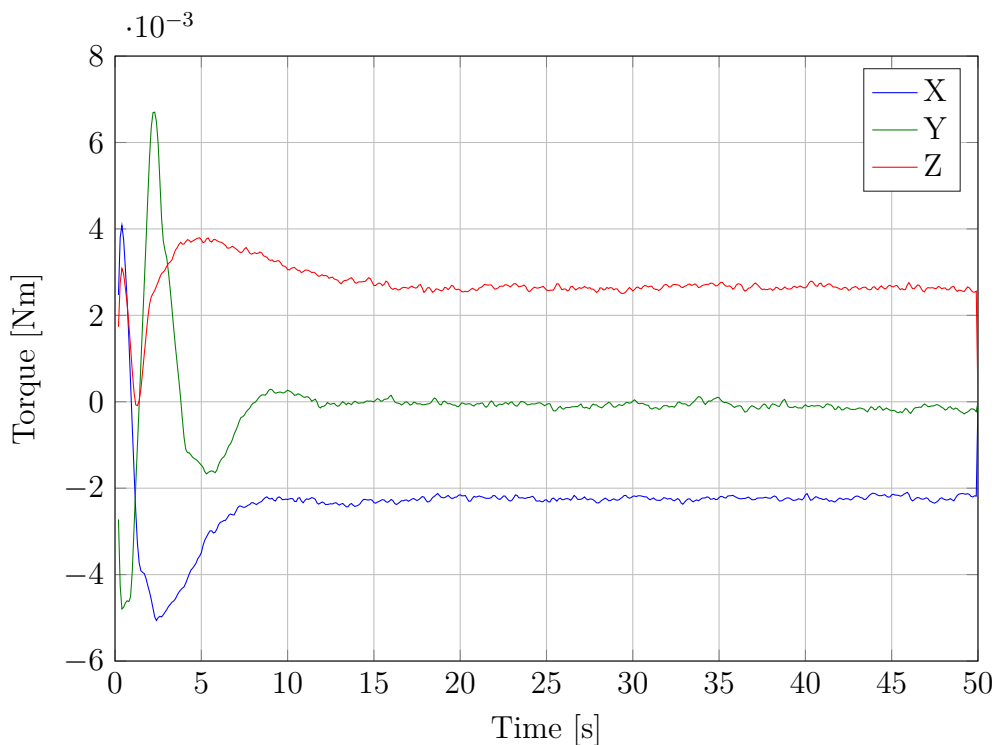


Figure 4.5: Reaction wheel torque during method 2 thruster identification.

Considering the thrusters' manufacturing method and their mounting process onto the platform's chassis, the magnitude of the force from a thruster and its direction in body frame coordinates allow, in principle, the possibility of a large inaccuracy. Nevertheless, in regard to the position vector  $\mathbf{r}_i$  of a given thruster in the body frame, the tolerances are comparatively small— so the vector  $\mathbf{r}_i$  is relatively well-known. By the well-known equation

$$\mathbf{t} = \mathbf{r} \times \mathbf{f} \quad (4.7)$$

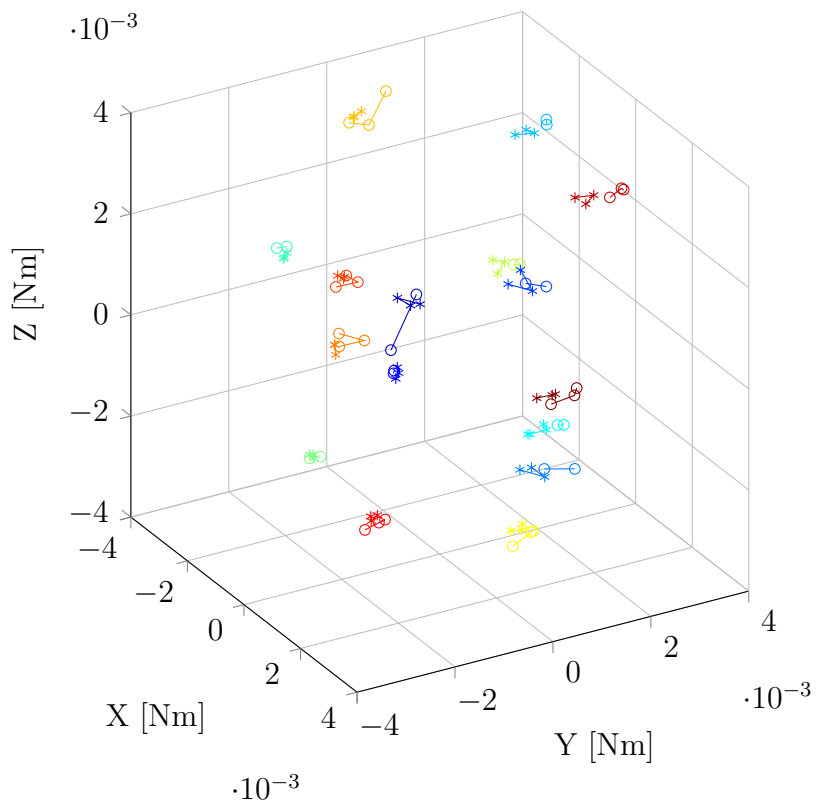
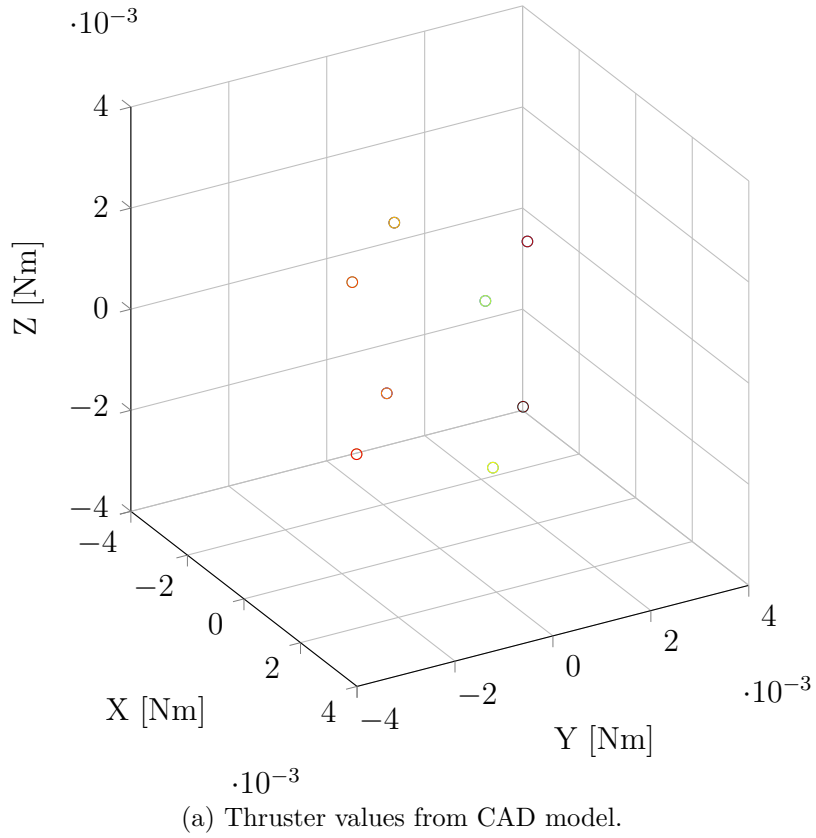
it's evident that the torque vector  $\mathbf{t}_i$  must be perpendicular to the position  $\mathbf{r}_i$ — that is, it has to lie on a plane  $\mathcal{P}$  that includes the origin and has  $\mathbf{r}_i$  as its normal vector. The distance from  $\mathbf{t}_i$  to  $\mathcal{P}$  thus represents a lower bound for thruster torque identification inaccuracy: a torque vector lying directly on the theoretical plane  $\mathcal{P}$  might correspond to reality, but one far from its corresponding  $\mathcal{P}$  is non-physical and indicates a high level of disturbance on the measurement.

### 4.3.1 Results

The torque values derived directly from the CAD model are shown in figure 4.6a. The figure reveals a very organized pattern, which is to be expected. Only 8 points are visible because each of them represents a pair of overlapping thrusters. By design there are 8 pairs with similar torques, but different force vectors.

For the identification both methods 1 and 2 were tested. As expected, it was observed that method 2's repeatability was better than that of method 1. This can be seen in figure 4.6b. It was also observed that method 2 returned results which were, for all thrusters, generally closer to the theoretical  $\mathcal{P}$  plane than method 1's results. This is a good indication that method 2 produces results which are closer to reality than method 1.

Considering the observed better repeatability and theorized lower uncertainty of method 2, it was decided that the final result of the identification for each thruster should be the average between runs of the  $\mathcal{P}$ -projections of method 2's results. As such an average will be within the convex hull of the projections, it will itself be contained in the plane  $\mathcal{P}$  also, giving a consistent value with the geometrical constraints of the problem.



(b) Comparison between thruster identification methods: method 1 (circle markers) and method 2 (star markers).

Figure 4.6: Thrust vectors plot. Different colors correspond to different thrusters.

# Chapter 5

## Static control

Generally, a system is said to be *tracking* a reference when the output of such a system is controlled to reach the (well-known, albeit arbitrary) reference (Koditschek, 1988). Considering a LTI system, the only way to achieve tracking is by the use of inverse dynamics (Koditschek, 1988); an example of such is feedback control. This chapter shows how position and attitude tracking was achieved for the TEAMS\_5D vehicle.

### 5.1 Control laws and attitude representation

The proportional-integral-derivative (PID) controller and its variations have been a mainstay of control engineering for decades. Despite the many advances obtained in control theory since the beginning of the space age, the PID still finds wide use in space applications—precisely because of its simplicity and extensive heritage in the field. It is not at all surprising, then, that a linear controller was used in this work. Still, although achieving position control on  $\mathbb{R}^2$  is—at least in theory—mostly a trouble-free endeavour, some complications arise when dealing with control on non-Euclidean manifolds such as  $\text{SO}(3)$ , the set of rigid rotations in three dimensions.

Feedback control is based on the concept of minimizing some error measure—generally the *distance* from the reference. While on  $\mathbb{R}^2$  the concept of distance is natural enough, on  $\text{SO}(3)$  the error measure depends on the chosen parametrization. Therefore, the first design decision is which attitude parametrization to choose. For this work quaternions, also known as the Euler-Rodrigues symmetric parameters, were chosen. As mentioned in chapter 2, quaternions are the ideal attitude representation for simulation. Although they require 4 storage parameters instead of the minimum 3, this poses no problem at all for modern computers. It can be considered a small price to pay in return for their most important advantages—globality and linear kinematics. These two points make quaternions the optimal choice for this work.

With our attitude representation chosen, we are still faced with the choice of control law to be used. Staying true to tradition, a PID variant will be used. This is not the end of the story, however: using quaternions, there is more than one control law which could be called “proportional” because in a non-Euclidean vector space like that of rigid body attitude configurations, there’s more than one useful way of quantifying error (Koditschek, 1988; Shuster, 1993).

Sidi (1997) defines an *error quaternion* and then presents a quaternion control law which ultimately derives from the Euler axis-angle representation. Considering

a starting quaternion  $\mathbf{q}_S$  and a target quaternion  $\mathbf{q}_T$ , the error quaternion  $\mathbf{q}_E$  is

$$\mathbf{q}_E = \mathbf{q}_S^{-1} \mathbf{q}_T \quad (5.1)$$

The quaternion can be interpreted as a hypercomplex 4-dimensional vector (Sidi, 1997)

$$\mathbf{q} = \hat{\mathbf{i}}q_1 + \hat{\mathbf{j}}q_2 + \hat{\mathbf{k}}q_3 + q_4 \quad (5.2)$$

where the complex components are subject to the following equations:

$$\begin{aligned} \mathbf{i}^2 &= \mathbf{j}^2 = \mathbf{k}^2 = -1 \\ \mathbf{ij} &= -\mathbf{ji} = \mathbf{k} \\ \mathbf{jk} &= -\mathbf{kj} = \mathbf{i} \\ \mathbf{ki} &= -\mathbf{ik} = \mathbf{j} \end{aligned} \quad (5.3)$$

By using these properties, a matrix representation for this equation is found to be

$$\mathbf{q}_E = \begin{bmatrix} q_{T4} & q_{T3} & -q_{T2} & q_{T1} \\ -q_{T3} & q_{T4} & q_{T1} & q_{T2} \\ q_{T2} & -q_{T1} & q_{T4} & q_{T3} \\ -q_{T1} & -q_{T2} & -q_{T3} & q_{T4} \end{bmatrix} \cdot \begin{bmatrix} -q_{S1} \\ -q_{S2} \\ -q_{S3} \\ q_{S4} \end{bmatrix} \quad (5.4)$$

This is what could be considered the most natural error measure on  $\text{SO}(3)$  using quaternion representation.

Using the error measure from 5.4, Sidi (1997) suggests the following proportional-derivative law to be used:

$$\mathbf{t} = 2K_p q_{E4} \begin{bmatrix} q_{E1} \\ q_{E2} \\ q_{E3} \end{bmatrix} + K_d \boldsymbol{\omega} \quad (5.5)$$

where the gains  $K_p, K_d$  need not be the same for all components, but here a simplified form is shown.

Wen and Kreutz-Delgado (1991) analyze equation 5.5 and show it to be almost globally asymptotically stable on the rigid body state space  $\text{SO}(3) \times \mathbb{R}^3$ —there's an (unstable) equilibrium when the error angle is exactly  $\pi$  and  $\boldsymbol{\omega} = \mathbf{0}$ . It is compared to another similar-looking quaternion control law (Wen and Kreutz-Delgado, 1991),

$$\mathbf{t} = 2K_p \begin{bmatrix} q_{E1} \\ q_{E2} \\ q_{E3} \end{bmatrix} + K_d \boldsymbol{\omega} \quad (5.6)$$

Note that the scalar part of the quaternion does not appear on the error measure anymore. This law is shown to be globally asymptotically stable<sup>1</sup>, and to have

---

<sup>1</sup>Bhat and Bernstein (2000) show that no smooth time-invariant law can be globally stable on the vector bundle  $\text{SO}(3) \times \mathbb{R}^3$ . So how can this law achieve global stability? The answer is that the law is in fact time-variant, although it does not appear to be so. As Wen and Kreutz-Delgado (1991) tell us, “[the implementation of this law] would require memory since the sign ambiguity in  $\mathbf{q}$  cannot be resolved from the attitude kinematic equation [on  $\text{SO}(3)$ ]”. A quaternion kinematic equation must be used, and that implies relying on the state history in order to make some choice which will resolve the sign ambiguity. Note that it *is* possible to create a smooth time-invariant globally stable control law on  $\mathbb{S}^3 \times \mathbb{R}^3$ , but as quaternion space double-covers rigid body attitude space this does not contradict the previous result (Chaturvedi et al., 2011).

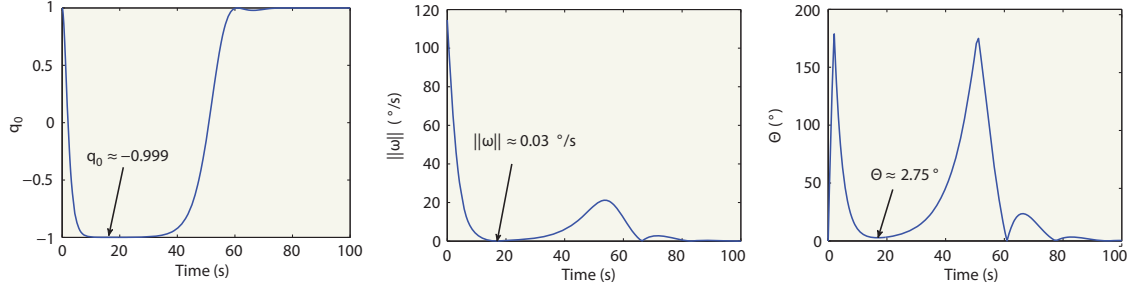


Figure 5.1: An example of the unwinding phenomenon (Chaturvedi et al., 2011): the rigid body initially comes to within  $2.75^\circ$  of the reference—only to move away, turn back and close on again (here the quaternion scalar component is  $q_0$ ).

generally better performance than equation 5.5 for large error angles (Wen and Kreutz-Delgado, 1991). However, this law projects  $\mathbf{q}_E$  and  $-\mathbf{q}_E$  onto different  $\mathbb{R}^3$  error measure vectors, although they represent the same configuration on  $\text{SO}(3)$ . This can lead to the undesirable phenomenon of *unwinding* (illustrated in figure 5.1), which is characterized by a large, wasteful excursion in attitude through a homoclinic-like orbit in state space when the attitude is already close to the reference (Bhat and Bernstein, 2000; Chaturvedi et al., 2011). The law described by equation 5.5 does not suffer from this problem, projecting antipodal error quaternions onto the same error measure vector. For this reason, which was considered to outweigh its relative weaknesses against 5.6, equation 5.5 was chosen to be implemented in the TEAMS\_5D vehicle.

For the position control, as mentioned before, we are not faced with any curved-space dilemmas: the error measure  $\boldsymbol{\epsilon} \in \mathbb{R}^2$  is simply the difference between the position reference and the body frame position within the room coordinate system. Therefore, the force control effort is

$$\mathbf{f} = K_p \boldsymbol{\epsilon} + K_d \mathbf{v} \quad (5.7)$$

where  $\mathbf{v} \in \mathbb{R}^2$  is the linear velocity of the vehicle<sup>2</sup>.

## 5.2 Linear Quadratic Regulator

Having selected the control structure, our attention can now be turned to quantifying  $K_p$  and  $K_d$ . The well-known linear quadratic regulator method (LQR) is convenient here because it provides a systematic way to calculate these gains (Ogata, 2001).

Given the state equation for a general linear system

$$\dot{\mathbf{x}} = \mathbf{Ax} + \mathbf{Bu} \quad (5.8)$$

the LQR problem (Ogata, 2001) is to find an optimal state-feedback matrix  $\mathbf{K}$  in

$$\mathbf{u} = -\mathbf{Kx} \quad (5.9)$$

---

<sup>2</sup>The gains for both attitude and position will be called simply  $K_p$  and  $K_d$ , although they may of course be different for each case. Hopefully the context shall prevent any possibility of confusion.

such that the performance index functional

$$J = \int_0^\infty (\mathbf{x}^* \mathbf{Q} \mathbf{x} + \mathbf{u}^* \mathbf{R} \mathbf{u}) dt \quad (5.10)$$

is minimized with respect to the given weights  $\mathbf{Q}$  and  $\mathbf{R}$ . It can be shown that if a positive-definite matrix  $\mathbf{P}$  can be found by solving the *reduced-matrix Riccati equation*

$$\mathbf{A}^* \mathbf{P} + \mathbf{P} \mathbf{A} - \mathbf{P} \mathbf{B} \mathbf{R}^{-1} \mathbf{B}^* \mathbf{P} + \mathbf{Q} = \mathbf{0} \quad (5.11)$$

then the solution to the LQR problem (Ogata, 2001) is

$$\mathbf{K} = \mathbf{R}^{-1} \mathbf{B}^* \mathbf{P} \quad (5.12)$$

and the resulting closed-loop system (given that  $\mathbf{A} - \mathbf{B}\mathbf{K}$  is stable) has infinite gain margin and at least  $60^\circ$  phase margin. These desirable characteristics, obtained in a systematic way instead of manual tuning, make the LQR a popular choice for many kinds of systems.

We will now obtain the gains for our system by means of solving a LQR problem. Consider a 1-DoF system of pure rotational inertia

$$\begin{bmatrix} \ddot{\theta} \\ \dot{\theta} \end{bmatrix} = \begin{bmatrix} 0 & 0 \\ 1 & 0 \end{bmatrix} \begin{bmatrix} \dot{\theta} \\ \theta \end{bmatrix} + T \begin{bmatrix} 1/I \\ 0 \end{bmatrix} \quad (5.13)$$

where  $\theta$  is the angular displacement,  $T$  is the torque input and  $I$  is the rotational inertia. The performance index functional is

$$J = \int_0^\infty (\mathbf{x}^T \mathbf{Q} \mathbf{x} + R u^2) dt \quad (5.14)$$

where

$$\mathbf{Q} = \begin{bmatrix} q_1 & 0 \\ 0 & q_2 \end{bmatrix}; q_1, q_2 \in \mathbb{R}^+, \quad R \in \mathbb{R}^+ \quad (5.15)$$

Assume

$$\mathbf{P} = \begin{bmatrix} p_1 & p_2 \\ p_2 & p_3 \end{bmatrix} \quad (5.16)$$

a real symmetric positive-definite matrix. Then the Riccati equation 5.11 becomes

$$\begin{aligned} & \begin{bmatrix} 0 & 1 \\ 0 & 0 \end{bmatrix} \begin{bmatrix} p_1 & p_2 \\ p_2 & p_3 \end{bmatrix} + \begin{bmatrix} p_1 & p_2 \\ p_2 & p_3 \end{bmatrix} \begin{bmatrix} 0 & 0 \\ 1 & 0 \end{bmatrix} - \\ & - \begin{bmatrix} p_1 & p_2 \\ p_2 & p_3 \end{bmatrix} \begin{bmatrix} 1/I \\ 0 \end{bmatrix} R^{-1} \begin{bmatrix} 1/I & 0 \end{bmatrix} \begin{bmatrix} p_1 & p_2 \\ p_2 & p_3 \end{bmatrix} + \begin{bmatrix} q_1 & 0 \\ 0 & q_2 \end{bmatrix} = \mathbf{0} \end{aligned} \quad (5.17)$$

Multiplying out, we get

$$\begin{bmatrix} 2p_2 & p_3 \\ p_3 & 0 \end{bmatrix} - \frac{1}{RI^2} \begin{bmatrix} p_1^2 & p_1 p_2 \\ p_1 p_2 & p_2^2 \end{bmatrix} + \begin{bmatrix} q_1 & 0 \\ 0 & q_2 \end{bmatrix} = \mathbf{0} \quad (5.18)$$

which results in the system of nonlinear equations

$$\begin{cases} \frac{p_2^2}{RI^2} - q_2 = 0 \\ p_3 - \frac{p_1 p_2}{RI^2} = 0 \\ 2p_2 - \frac{p_1^2}{RI^2} + q_1 = 0 \end{cases} \quad (5.19)$$

Using the fact that  $\mathbf{P}$  must be positive-definite, the solution is found to be

$$\mathbf{P} = \begin{bmatrix} I\sqrt{R(2I\sqrt{q_2 R} + q_1)} & I\sqrt{q_2 R} \\ I\sqrt{q_2 R} & \sqrt{q_2(2I\sqrt{q_2 R} + q_1)} \end{bmatrix} \quad (5.20)$$

from which we finally get  $\mathbf{K}$ :

$$\mathbf{K} = R^{-1}\mathbf{B}^T\mathbf{P} = \begin{bmatrix} \sqrt{2I\sqrt{\frac{q_2}{R}} + \frac{q_1}{R}} & \sqrt{\frac{q_2}{R}} \end{bmatrix} \quad (5.21)$$

From our definition of  $\mathbf{x}$ , the proportional and derivative gains come directly from  $\mathbf{K}$ :

$$K_p = \sqrt{\frac{q_2}{R}} \quad K_d = \sqrt{2I\sqrt{\frac{q_2}{R}} + \frac{q_1}{R}} \quad (5.22)$$

It is worth noting that the proportional gain  $K_p$  does not depend on the inertia  $I$ ; only on  $q_2$  (which controls the effect of the displacement on the performance index functional) and  $R$  (the control effort weighting). Also, for each of the 3 axes,  $I$  was considered as the inertia tensor main diagonal component for that axis, resulting in different derivative gains for  $X$ ,  $Y$  and  $Z$ .

The LQR process says nothing about how to choose the weights  $\mathbf{Q}$  and  $R$ ; they are entirely the designer's choice. In our case, the weights were chosen in order to have a critically damped response (damping ratio  $\zeta = 1/\sqrt{2}$ ) and minimize the actuation effort, while keeping rise time below 5 s to allow reasonable performance.

In order to obtain the gains through the LQR procedure, we have heavily simplified the system model, ignoring cross-coupling between the axes, for example. Moreover, our linear system model (5.13) assumes the control effort in our chosen control law to be linearly related to the error angle  $\varphi$  (in an axis-angle attitude error representation sense). Wen and Kreutz-Delgado (1991) show that this is not true; in fact, the proportional feedback term in equation 5.5 varies with  $\sin \varphi$ . Nevertheless, the approximation gets better as the error angles get smaller, and extensive simulation has shown the performance of the system not to be greatly affected.

In the case of position control, it is easily shown that the same system model (5.13) can be used—of course, replacing the torque  $T$ , inertia  $I$ , and angular displacement  $\theta$  with the force  $\mathbf{f}$ , mass  $m$ , and linear displacement  $\boldsymbol{\epsilon}$ . The LQR problem then yields the gains

$$K_p = \sqrt{\frac{q_2}{R}} \quad K_d = \sqrt{2m\sqrt{\frac{q_2}{R}} + \frac{q_1}{R}} \quad (5.23)$$

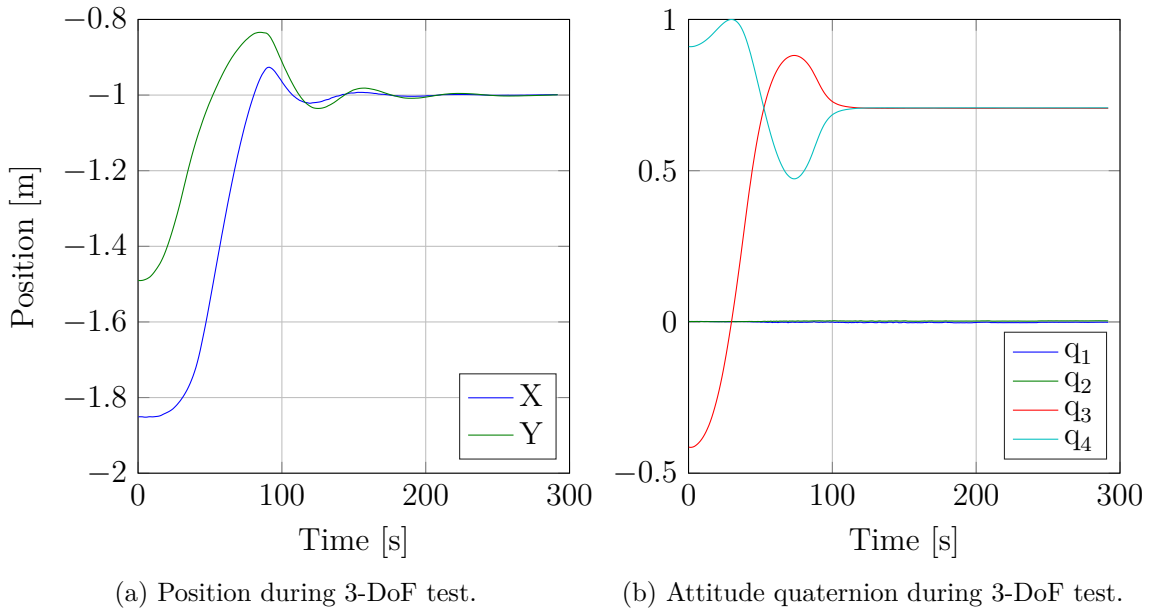


Figure 5.2: 3 degree-of-freedom (2 positional, 1 rotation) closed-loop test results.

The advantage here is that the linear system in this case is a much better approximation for the real system dynamics than in the attitude case, and the error measure corresponds exactly to the “real” error. Therefore, theoretical LQR properties like infinite gain margin and minimum 60° phase margin are expected here to be closely followed by the closed-loop system.

### 5.3 Results

Initially, experiments were performed in that the lower platform was fixed to the attitude platform, forming a 3DOF unit. This allowed jumping from pure simulation to testing on a reasonably low-complexity system, helping to iron out any transitional “teething problems”. In this initial phase, the vehicle traversed over the granite table to its reference position and attitude under thruster action, starting from many different initial states. Figure 5.2 shows the results from one such test.

In a second testing phase, the spherical air bearing was activated, and the platform became a 5-DoF vehicle. Various experiments were performed in which the platform, starting from a reasonably random initial attitude and angular velocity, had to reach the attitude and position references under thruster action. A typical example is illustrated on figure 5.3.

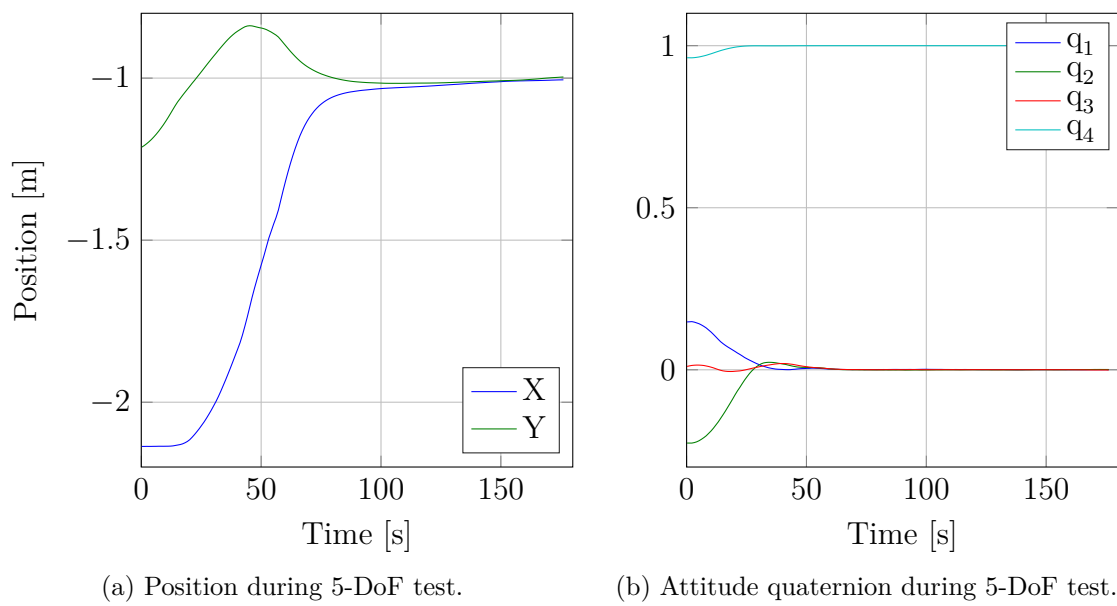


Figure 5.3: 5 degree-of-freedom closed-loop test results.

# Chapter 6

## Balancing

As explained in chapter 2, simulation of torque-free dynamics is not a simple endeavour. This chapter details one of the most important steps to be followed in order to get faithful dynamics in torque- and force-free simulations: the elimination of (most) gravity disturbances.

### 6.1 Gravity disturbances

In the simulation of a torque-free environment, perhaps the most important obstacle to be overcome is the elimination of gravity-related disturbances (Smith, 1965). This issue was raised in chapter 2, together with descriptions of many other sources of disturbing torques. The gravity disturbance sources can be roughly divided into two categories: those which can be equated to a mass unbalancing (for example, replacement of components) and those which can't, because for example their effect on the system varies as the gravity vector changes in relation to the body frame (anisoelastic torques, gravity gradient).

In this chapter we focus on how the first, simpler class of gravity disturbances can be eliminated (or at least diminished) by a *balancing procedure*. A balancing procedure uses the sliding mass balance system described in chapter 3 to collocate both the center of gravity and the center of rotation of the attitude platform, thus eliminating gravity torques. This can be done “off-line” (before testing) or “on-line” (during testing); both are based on the same principles, but use slightly different methods.

The (re)placement of components on the platform has a definite impact on the balancing state. Moreover, in a research environment, it is expected that some aspects of the experiment will change over time. Still in the 1960's, Smith (1965) recognizes the impact these (possibly frequent) changes have by telling us that, for research purposes, “the requirements for frequent modification of equipment are so important that some sort of automatic or semi-automatic balance system is needed”.

#### 6.1.1 Air mass unbalancing

Consider for a moment that it would be possible to put the platform in a state where gravity unbalances are completely eliminated. Nevertheless, as the platform is ran through a test and the thruster system is used, this balance would soon be disturbed.

The attitude platform carries four compressed air bottles positioned in a symmetric fashion. However, it's well recognized in the literature that, when fine balancing is taken into account, "even carefully balanced pairs of compressed gas tanks with a common manifold are still troublesome as they expand under pressure and shift slightly" (Smith, 1965). This means that it's almost certain that the centroid of the air mass inside the bottles will not be collocated with the air bearing's center of rotation, and as the compressed air is depleted, unbalancing will appear. As for the magnitude of the effect, Smith (1965) highlights that "unbalance torques due to unsymmetrical depletion of tanks as compressed gas is used for reaction thrust can be appreciable". This was confirmed in testing with the TEAMS\_5D vehicle: attitude control accuracy was noted to decrease towards the end of test runs, especially for long tests.

The body frame origin is defined to be located at the center of the spherical air bearing. As the whole pneumatic circuit (bottles, conduits) is fixed to the body, consider that the (variable) air mass  $m_a$  has its center of gravity located at a fixed position  $\mathbf{r}_a$  in the body frame. We can then see there's a disturbing torque

$$\mathbf{t}_a = m_a (\mathbf{r}_a \times \mathbf{g}) \quad (6.1)$$

which continuously varies, both because  $\mathbf{g}$  varies in the body frame as the attitude changes (while  $\mathbf{r}_a$  is fixed in the body frame, as previously said), and because  $m_a$  varies as the thrusters are used and the compressed air reservoirs are depleted.

## 6.2 Off-line balancing

As mentioned before, in order to improve results it is important to reduce gravity torques as much as possible. It would be desirable if we could start each test with a balanced platform. Therefore, before each test run the platform goes through an automatic balancing procedure.

The procedure sequence is as follows. Initially, the attitude platform is brought to a neutral attitude ( $\theta = 0, \phi = 0$ ), using the reaction wheels in a closed loop. The controller described in chapter 5 is used; however here an integral factor is added, turning it into a PID controller:

$$\mathbf{t} = 2K_p q_{E4} \begin{bmatrix} q_{E1} \\ q_{E2} \\ q_{E3} \end{bmatrix} + K_d \boldsymbol{\omega} + 2K_i \int_{t_0}^t q_{E4} \begin{bmatrix} q_{E1} \\ q_{E2} \\ q_{E3} \end{bmatrix} dt \quad (6.2)$$

where  $t_0$  indicates when last the magnitude of the positional error was over a certain threshold. This effectively disables the integral factor for large positional errors, such that the response to large slews is not adversely affected performance-wise. Nevertheless, the system keeps the most desirable property given by a PID controller: null steady-state error. The integral gain  $K_i$  is chosen in order to allow a reasonably unbalanced platform to reach a small enough attitude error in less than about 15 s. Since the actuators have a strictly limited torque range, anti-windup correction is used. The model is shown in figure 6.1.

After the platform's angular velocity and attitude error are small enough, the balancing system is turned on. The control effort signal from the balancing loop is

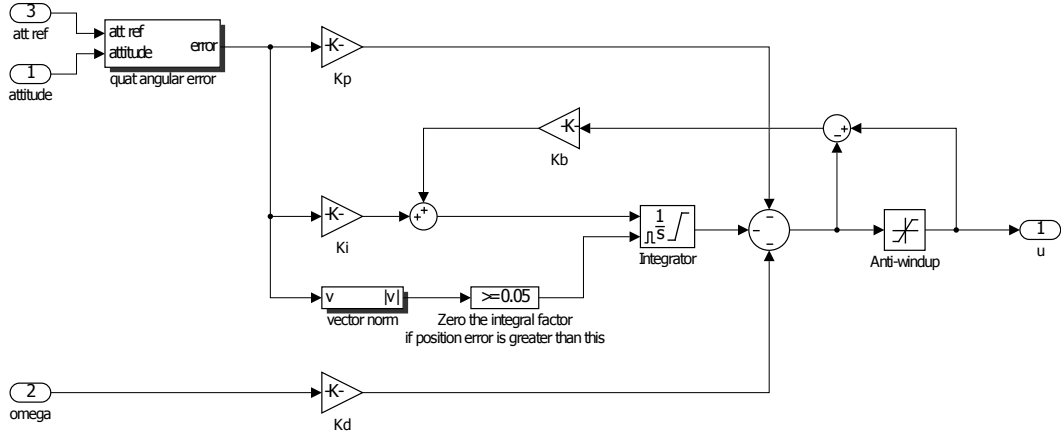


Figure 6.1: Simulink model block for the attitude PID controller with anti-windup.

used to move the horizontal balancing weights, while the  $Z$ -axis weight position is kept unchanged. The model calculates a sliding window RMS value for the control effort; after the RMS value is reduced below a set threshold, the platform is deemed balanced in the  $X$  and  $Y$  axes. The balancing system is then turned off, and the platform's attitude reference is changed to a banked position (fixed  $\theta \neq 0, \phi = 0$ ). After the platform stabilizes, the process repeats—this time moving only the  $Z$ -axis balancing weight position. When the procedure finishes, we have

$$m_b \mathbf{r}_b = -m_a \mathbf{r}_a \quad (6.3)$$

where  $m_b$  is the mass of a balancing weight (all three weigh the same) and  $\mathbf{r}_b$  is their displacement vector. The origin of  $\mathbf{r}_b$  is placed at the balanced position when  $m_a = 0$ ; this changes when, for example, equipment is added to/taken from the platform.

Since the yaw angle is irrelevant for this procedure, the IMU's accelerometer was used for attitude determination instead of the DTrack system.

### 6.3 On-line air mass variation correction

With the off-line balancing procedure, the platform starts each test run in a balanced state. However, as the test progresses and the compressed air supply depletes itself, the attitude platform becomes progressively unbalanced—the term  $m_a$  in equation 6.3 changes over time, breaking the equality. As in testing a PD attitude controller is used, the gravity torque thus created causes a growing steady-state error. Correcting this unbalancing during the experiment is important to maintain the quality of the results.

As early as the 1960's, Hatcher and Young (1968) discuss an automatic balancing technique based on using the time-averaged control effort signal during limit-cycle operation to move balancing weights and balance an air bearing platform during a test. Ultimately, it's needed to change the paradigm of how the balancing system is seen: from a simple fixed “adjustment” system more akin (from an experiment perspective) to manually adding weights to the platform for balancing, to an extra

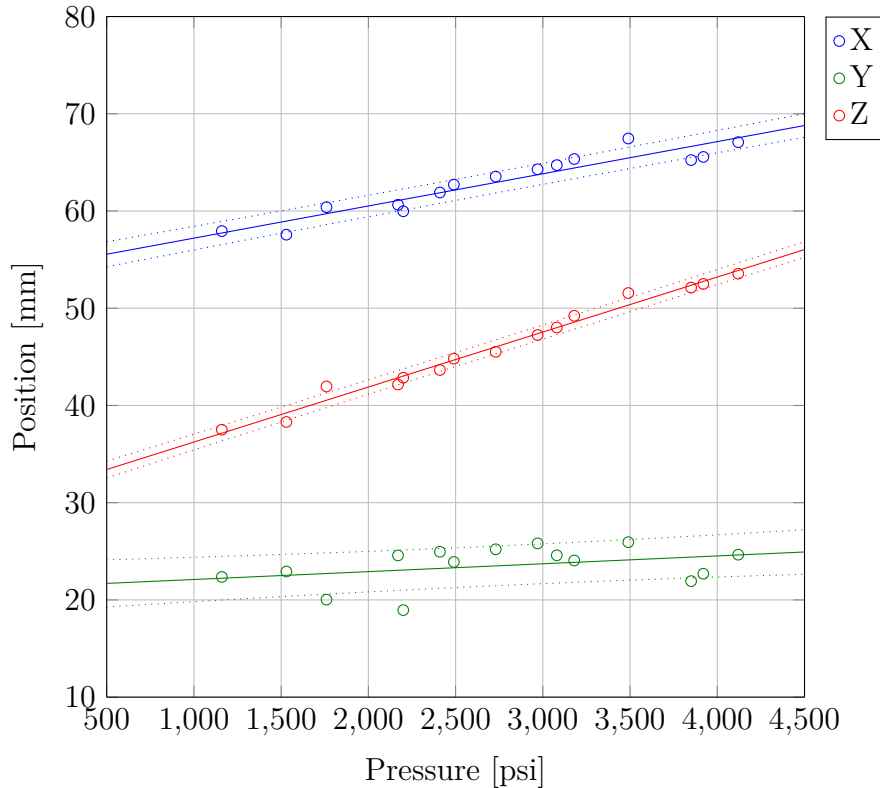


Figure 6.2: Correlation model between reservoir pressure and balancing position, for each axis.

actuator system (albeit a very low-bandwidth one). In fact, Cho and McClamroch (2002) describe a technique to attain triaxial attitude stabilization using only linear mass actuators, similar to the TEAMS\_5D balancing system. Shen et al. (2002) study the controllability properties of such a setup.

The on-line correction problem is solved by the action of three components:

- a model which relates bottle pressure with balancing weights' positions;
- an open-loop estimation of pressure variation; and
- a closed-loop correction.

### 6.3.1 Pressure-position model

It is clear that  $m_a$  can't be directly measured, so the reservoir pressure is taken as a measure for it. Considering a fixed air mass temperature,  $m_a$  is proportional to the manometric pressure indicated by the platform's pressure gauge. As the laboratory's temperature is controlled, this is generally a good approximation. Under certain conditions (immediately after filling the bottles, or after rapid discharging) the air mass temperature changes significantly from the ambient temperature, so it's necessary to let the temperature stabilize before taking pressure readings.

At every balancing, data is recorded (bottle pressure and balancing weights' positions) and fed into a linear model that correlates both sets. This is consistent with

our unbalancing model, explained previously. The populated model is illustrated in figure 6.2. This model relates variations in reservoir pressure with the balancing weights' positions. Accordingly, if we can get a reliable estimate for the pressure variation during a test, we can command position changes on the weights directly and eliminate the need for a separate balancing procedure. However, the platform is not equipped with pressure transducers on the pneumatic circuit, and somehow reading the pressure gauges during the test and inputting the value into the model would be unpractical. Subsections 6.3.2 and 6.3.3 describe how to obtain a pressure estimate through other means.

### 6.3.2 Spent gas estimation

We will make the approximation that exhaust velocity on the cold gas thrusters does not change with the set thrust level<sup>1</sup>. This means that thrust is proportional to mass flow. As the thruster output signal is linearized, we can integrate the thruster actuation  $u(t)$  (which, because of the constant exhaust velocity approximation, has a dimension of [mass/time]) over time since the beginning of the run to get an estimate  $\Delta\tilde{m}_a$  of the air mass difference:

$$\Delta\tilde{m}_a = \int_0^{t_f} u(t) \, dt \quad (6.4)$$

Testing data was collected over many different test runs to correlate  $\Delta\tilde{m}_a$  with the actual pressure difference between the beginning and the end of the run. A sample from this data is illustrated in figure 6.3. From these curves, an empirical correlation curve was obtained which is used to correct the estimate  $\Delta\tilde{m}_a$  and relate it to the estimated variation in bottle pressure. This *open-loop estimate*  $\Delta\tilde{p}_1$  starts at 0 at the beginning of the test and increases monotonically during the experiment.

### 6.3.3 Closed-loop disturbance correction

Going back to the air mass gravity disturbance torque equation 6.1, we will now consider how to take advantage of some properties in this unbalancing model in order to design a closed-loop pressure variation estimator.

Consider the air mass distance vector  $\mathbf{r}_a = \|\mathbf{r}_a\| \hat{\mathbf{r}}_a$ , where  $\hat{\mathbf{r}}_a$  is its unitary direction vector. Although the (varying) unbalancing air mass  $m_a$  and the absolute distance of the air mass from the origin  $\|\mathbf{r}_a\|$  cannot be precisely known, there *is* a way to determine  $\hat{\mathbf{r}}_a$ . Looking at figure 6.2 again, we can see that the angular coefficients of the three lines  $\gamma_X$ ,  $\gamma_Y$ ,  $\gamma_Z$  determine a  $\mathbb{R}^3$  direction vector over which a single weight should move in order to perform the same balancing as the three-weight balancing system<sup>2</sup>. A 3D plot of the balancing data, which should further help to visualize

---

<sup>1</sup>This is admittedly a rough approximation, however a more adequate investigation of the thrusters' characteristics would take considerable time; not getting mired in this (considering the control-focused scope of this work) relatively minor point is all the more reason for the addition of a closed-loop correction.

<sup>2</sup>Note, again, that here the origin of the vector is largely unimportant because it's determined by the mass distribution of the rest of the platform, but its direction depends only on the properties of the compressed air system.

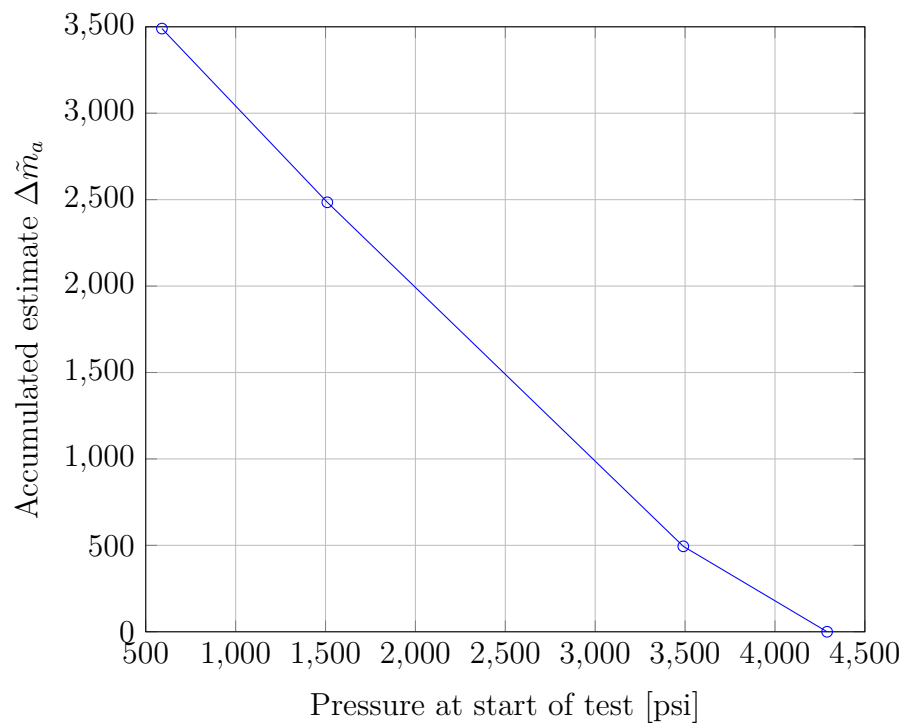


Figure 6.3: Data from one of the pressure estimation sequences. Each of the points is a separate test run.

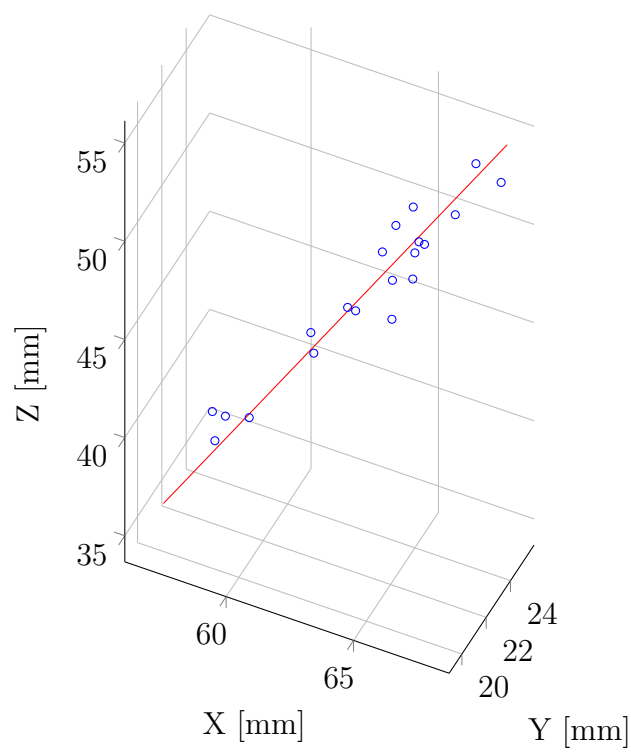


Figure 6.4: 3D plot of the pressure-position model data.

this, is displayed in figure 6.4. From these observations, it is clear that

$$\hat{\mathbf{r}}_a = -\frac{\langle \gamma_X, \gamma_Y, \gamma_Z \rangle}{\|\langle \gamma_X, \gamma_Y, \gamma_Z \rangle\|} \quad (6.5)$$

Also, at any point in time the platform's current attitude is known, therefore we know  $\mathbf{g}$  in body frame coordinates. From 6.1 we are then able to know the unitary direction vector  $\hat{\mathbf{t}}_a$

$$\hat{\mathbf{t}}_a = \frac{\hat{\mathbf{r}}_a \times \mathbf{g}}{\|\hat{\mathbf{r}}_a \times \mathbf{g}\|} \quad (6.6)$$

so that  $\mathbf{t}_a = \|\mathbf{t}_a\| \hat{\mathbf{t}}_a$ . We can now get the projection of the actual disturbance torque  $\hat{\mathbf{t}}_d$  (taken directly from the attitude control effort signal) on the direction vector  $\hat{\mathbf{t}}_a$ :

$$\vartheta = \hat{\mathbf{t}}_a \cdot \mathbf{t}_d \quad (6.7)$$

In a sense the correlation  $\vartheta$  determines, from all disturbance torques currently affecting the control loop, not the fraction that could be attributed to air mass unbalancing, but the fraction that could be reasonably corrected by the balancing system, although the distinction here is not important<sup>3</sup>. After going through a sliding-window average filter of length  $w$ ,  $\hat{\vartheta}$  can be seen as an estimate of the average air mass unbalancing disturbance over the last  $w$  seconds<sup>4</sup>. This information is then used (together with the pressure-position model) to get the *closed-loop estimate*  $\Delta\tilde{p}_2$  of the current unbalancing, in air pressure units.

The sum of open- and closed-loop pressure difference estimates is input into the linear model to determine how much the balancing weights should be moved in order to restore balancing to the attitude platform. The result is used to change the balancing weights' positions in real time during the experiment.

Testing indicates that the unbalancing over a test run is greatly diminished by the use of the correction, and the pressure estimates are generally quite close to the actual pressure variation. This can be assessed by the fact that, after a long test, the off-line balancing procedure makes much smaller changes to the balancing weights' positions if the test was done with the corrections.

---

<sup>3</sup>In fact, if there is any other closely-correlated but unmodelled disturbance that can be corrected this way, all the better.

<sup>4</sup>In the case of trajectory control (chapter 7)  $w$  should be large enough that  $\hat{\vartheta}$  is not affected by local trajectory features, as it can be expected that the torque disturbances will in general exhibit at least *some* locality relative to the attitude configuration.

# Chapter 7

## Trajectory control

For the intended use of the TEAMS facility, performing trajectory control on the air bearing platforms is extremely important: the test of formation flying algorithms requires that each vehicle stick to its intended trajectory, so that the overall configuration can be analyzed. Accordingly, after the platform was successfully controlled to reach a static reference, the next step was to make it follow a given trajectory in state space.

As previously mentioned in chapter 3, one of the objectives for the project was to produce a demonstration of the capabilities of the platform. To fulfill this requirement, an experiment was devised in which the attitude platform's laser pointer should be aimed at a fixed spot somewhere in the laboratory while the vehicle moves around the table in a predetermined fashion. This test emulates, for example, requirements for laser communication between satellites flying in formation.

A brief distinction has to be made here about the difference between *path following* and *trajectory tracking* (Aguiar and Hespanha, 2007). Path following generally refers to a class of problems in which the configuration reference is given in a time-free parametrization, while in trajectory tracking the reference state space trajectory is given as a function of time (Pascoal and Aguiar, 2011). According to Pascoal and Aguiar (2011), “path-following is motivated by applications in which spatial errors are more critical than temporal errors”. For formation flying specifically, both spatial and temporal errors are very important due to the need of simulating relative orbital motion between the spacecraft; therefore, only trajectory control will be considered here.

Position trajectory control will be addressed first; after that, work done on the more challenging attitude trajectory control will be described. Test trajectories had to be selected for each case, and this will be approached on the guidance subsections. For control, a combination of feedback and feedforward was used. As the feedback controllers used are the same as described on chapter 5, the control subsections will focus mainly on the feedforward part of the controller. Oosting and Dickerson (1988), studying the control of a robotic manipulator, report on the advantages of using feedforward control on nonlinear systems.

The implemented feedforward control takes information about the state space trajectory  $\xi(t) = \langle \mathbf{x}_\xi(t); \mathbf{R}_\xi(t); \dot{\mathbf{x}}_\xi(t); \dot{\mathbf{R}}_\xi(t) \rangle$  and uses a inverse dynamics model of the system to find the control effort  $\nu_f$  which will make the system follow the prescribed trajectory.  $\nu_f$  is added to actuator input directly, together with the feedback control effort  $\nu_b$ . An illustrative block diagram of feedforward control is displayed on figure 7.1.

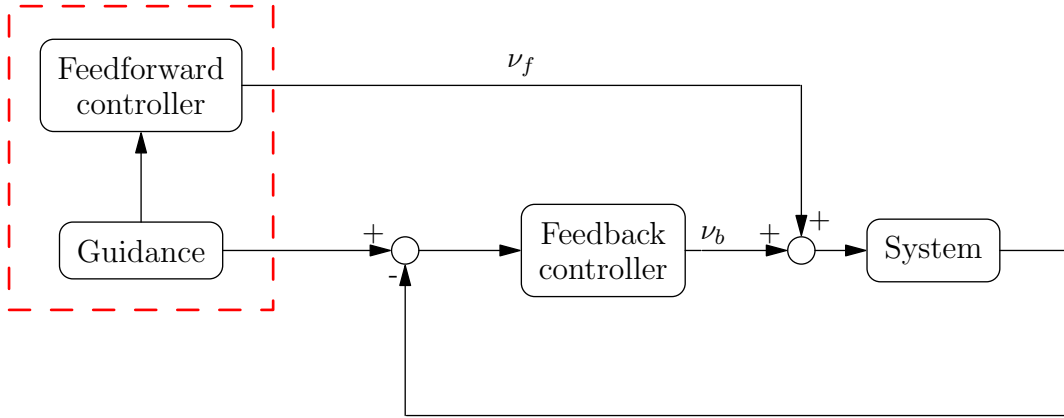


Figure 7.1: Combined feedforward + feedback controller.

## 7.1 Position

### 7.1.1 Guidance

For the laser pointing experiment, the chosen position trajectory over the table was a circle of radius  $r_\xi = 0.5$  m, traversed in a period of  $T_\xi = 180$  s. Although the period is shorter than that of characteristic timescales for LEO formation flying maneuvers, a small period was desirable in order to test the limits of the vehicle. Faster periods and larger trajectory radii were tested, but during the course of the trajectory sometimes the control allocator hit a limit and would have to scale down torque, force, or both. The values shown were found to allow the thruster allocation to fully cope with the simultaneous torque and force requests, with an added safety margin.

### 7.1.2 Feedforward

Although a great many possible parametrizations for the circle exist, here the most common one will be used; the trigonometric parametrization

$$\mathbf{x}_\xi(\tau) = r_\xi \begin{bmatrix} \cos(\omega_\xi \tau + \varphi) \\ \sin(\omega_\xi \tau + \varphi) \end{bmatrix} \quad (7.1)$$

where  $\omega_\xi$  is the trajectory angular velocity,  $\varphi$  is a freely chosen phase constant and  $\tau$  is a *trajectory time* parameter  $\tau = \tau(t)$ . The need for such a parameter arises in that the parametrization used has a velocity vector

$$\dot{\mathbf{x}}_\xi(\tau) = \omega_\xi r_\xi \dot{\tau} \begin{bmatrix} -\sin(\omega_\xi \tau + \varphi) \\ \cos(\omega_\xi \tau + \varphi) \end{bmatrix} \quad (7.2)$$

whose magnitude is

$$\|\dot{\mathbf{x}}_\xi(t)\| = \omega_\xi r_\xi \dot{\tau} \quad (7.3)$$

It is clear that 7.3 is constant over time if we use the trivial choice  $\tau(t) = t$ . As the initial velocity of the system is in general not equal to  $\dot{\mathbf{x}}_\xi(0)$ , this causes a step in the velocity reference when the trajectory starts. This is clearly impossible for the

system to follow; it's likely that the vehicle will take a long time to "catch up" to the moving position reference, considering it is able to do it at all. The problem is solved by choosing  $\tau(t)$  such that  $\dot{\tau}(0) = 0$ , and make it rise smoothly during a defined *ramp-up time*  $t_r$ . One possible solution—which was the one implemented in the system—is choosing  $\tau(t)$  to be a cubic polynomial in  $t$  until  $t = t_r$ , and from then on making  $\dot{\tau}(t) = 1$ . The polynomial coefficients were thus chosen such that

$$\begin{aligned}\tau(0) &= 0 \\ \dot{\tau}(0) &= 0 \\ \dot{\tau}(t_r) &= 1 \\ \ddot{\tau}(t_r) &= 0\end{aligned}\tag{7.4}$$

in order to satisfy the previous requirements and, additionally, make the force continuous after  $t = 0_+$ . This last requirement serves to avoid exciting the platform's structure and creating unnecessary vibrations. The final polynomial is

$$\tau(t) = -\frac{t^3}{3t_r^2} + \frac{t^2}{t_r}\tag{7.5}$$

Taking  $\tau(t)$  into account, the expression for the feedforward force vector  $\mathbf{f}_\xi$  as a function of time can be found through the chain rule:

$$\mathbf{f}_\xi(t) = m \left[ \frac{d\mathbf{x}_\xi}{d\tau} \frac{d^2\tau}{dt^2} + \frac{d^2\mathbf{x}_\xi}{d\tau^2} \left( \frac{d\tau}{dt} \right)^2 \right]\tag{7.6}$$

## 7.2 Attitude

### 7.2.1 Guidance

As has been the common thread in this work, the position guidance was developed in a relatively simple way, but the attitude guidance will require a bit more thought.

In principle, an attitude trajectory  $\mathbf{R}_\xi(t)$  could be designed specifically for the chosen position trajectory in order to attain the required pointing. In this case however, if we wanted to change the position trajectory then the attitude trajectory would also have to be recalculated. Such a scheme also allows little in the way of keeping pointing precision: if a disturbance moves the vehicle slightly away from the intended position trajectory, the attitude platform has no way of adjusting its pointing. This is so because its attitude reference changes only with time and not with position.

A more flexible (and realistic, considering hypothetical formation flying scenarios) alternative is to determine the attitude reference  $\mathbf{R}(t)$  at each instant, based on knowledge about the current position  $\mathbf{x}(t)$  of the platform. If, additionally,  $\dot{\mathbf{x}}_\xi(t)$  and  $\ddot{\mathbf{x}}_\xi(t)$  are known—which they are, since the position trajectory has already been designed at this point—, then we should be able to calculate  $\dot{\mathbf{R}}_\xi(t)$  and  $\ddot{\mathbf{R}}_\xi(t)$ . This information can then be used to calculate feedforward torques in order to (together with feedback) keep the pointing.

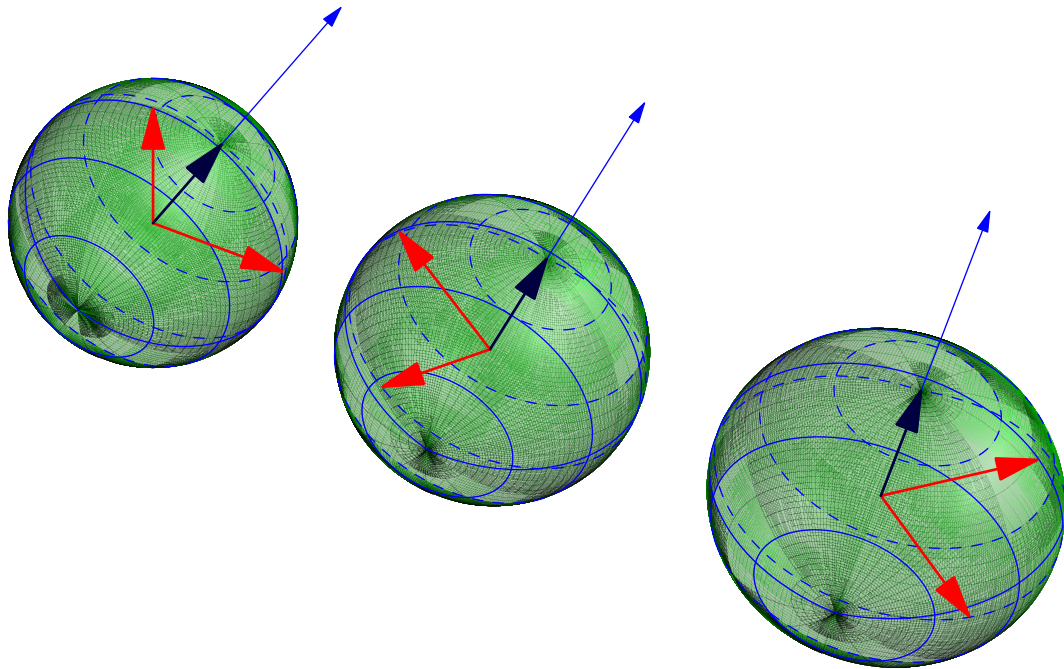


Figure 7.2: Simple pointing problem: the solution set contains a multitude of reduced-attitude configurations.

### 7.2.1.1 Simple pointing

Consider first the simple pointing problem, which Chaturvedi et al. (2011) refer to as the “reduced-attitude problem”. As we know, rigid-body attitude configurations are defined on  $\text{SO}(3)$ . A *reduced-attitude configuration* arises when the matter of interest is not fully defining the attitude, but orienting some body frame-defined direction of interest relatively to a global frame-defined direction. This configuration space is defined on the 2-sphere  $\mathbb{S}^2$ . Such a formulation (illustrated in figure 7.2) is interesting in cases where rotations about the body-frame defined direction are not relevant to the problem (Chaturvedi et al., 2011).

In the case of the TEAMS\_5D vehicle, the body frame-defined direction of interest is represented by the laser ray unitary vector  $\hat{\rho}$ . A statement of the simple pointing problem in this case would be to make the laser ray direction  $\hat{\rho}$  and the (global frame-fixed) target position direction coincide in the body frame. Accordingly, it is easy to see that not only one particular  $\text{SO}(3)$  attitude configuration solves this problem—after the platform is pointing to the right direction, the body frame can be freely rotated about the laser ray pointing vector  $\hat{\rho}$ , and the laser will still illuminate the target. Therefore, the solution set  $\mathcal{S} \subset \text{SO}(3)$  to the simple pointing problem corresponds to a single *point* on the 2-sphere  $\mathbb{S}^2$ . The solution is, as it must, a (strict) subset of the full configuration space  $\text{SO}(3)$ , but it’s also relevant to note that it’s a smooth one-dimensional manifold (Chaturvedi et al., 2011). For the application being implemented, it is interesting to minimize roll angle because the force the thrusters on the attitude platform can exert in the body frame  $Z$  direction is much lower than in the other directions; this means that controlling the position of a banked platform is much harder than doing so when the platform in a

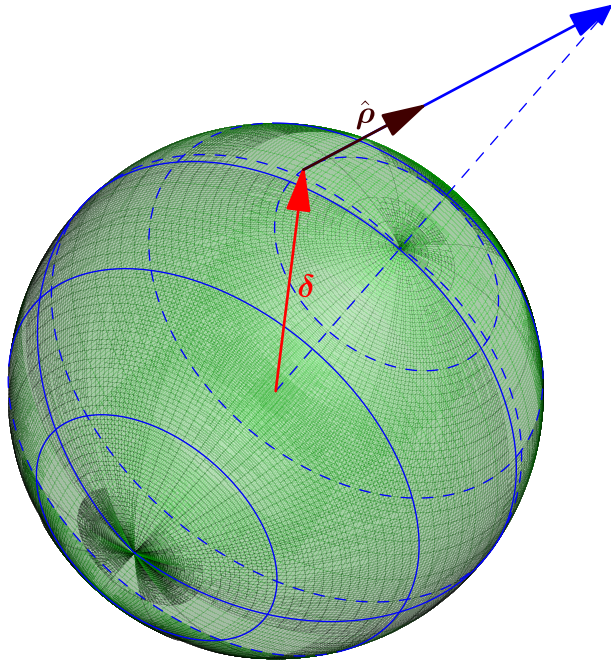


Figure 7.3: Displaced pointing problem: the solution cannot be expressed as a reduced-attitude set.

level position. The degree of freedom afforded by the solution set's topology would enable us to do just that—pick a solution where the roll angle  $\phi$  is minimal.

#### 7.2.1.2 The “displaced pointing” problem

Consider the laser affixed to the attitude platform, with its unitary direction vector  $\hat{\rho}$ . Let  $\mathcal{L}$  be the body-fixed 3-dimensional laser ray line—the locus of the laser ray in case it stretched to infinity both forwards and backwards. For the pointing of the laser to be able to be represented in reduced-attitude form, it is necessary that  $\mathcal{L}$  contains the body frame origin—the attitude platform's center of rotation. It is easy to see that, if this requirement is not attained, in general a rotation about  $\hat{\rho}$  will change the pointing; consequently, the problem can't be represented on  $\mathbb{S}^2$ .

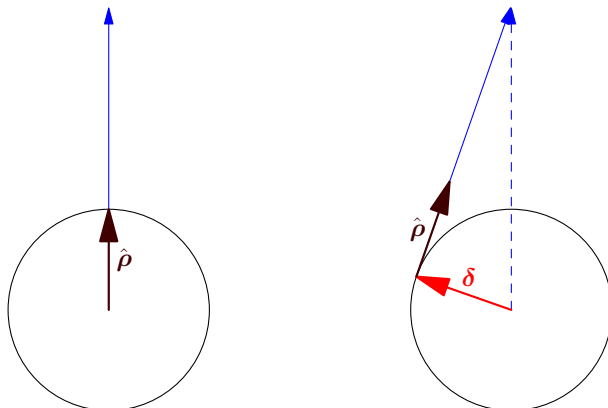


Figure 7.4: Comparison between simple and displaced pointing problems.

That is exactly the case as it happens with the TEAMS\_5D vehicle. Because of physical constraints, it would be unfeasible to mount the laser such that  $\mathcal{L}$  contains the body frame origin. Moreover, even if possible, such a solution would not be robust against mounting tolerances. The requirements indicate the need for a pointing solution which will allow the laser ray line  $\mathcal{L}$  to be *displaced* from the body frame origin—such a solution will henceforth be called the *displaced pointing problem* (as opposed to the *simple* pointing problem).

A new parameter is introduced now to allow the problem formulation to reflect the platform's physical reality. Consider  $\kappa$ , the point of closest approach to the origin of the laser ray line  $\mathcal{L}$ . Let the distance vector from the origin to  $\kappa$  be named  $\boldsymbol{\delta}$ , the *displacement vector*. Any body frame laser mounting can be fully represented by its set  $\{\hat{\boldsymbol{\rho}}; \boldsymbol{\delta}\}$ : if  $\mathbf{r}_l$  is the laser pointer position within the body frame, then

$$\boldsymbol{\delta} = \mathbf{r}_l - (\mathbf{r}_l \cdot \hat{\boldsymbol{\rho}}) \hat{\boldsymbol{\rho}} \quad (7.7)$$

This definition of  $\boldsymbol{\delta}$  allows a precise mathematical description for the laser ray line as

$$\mathcal{L} = \{\mathbf{l} \in \mathbb{R}^3 \mid \mathbf{l} = \boldsymbol{\delta} + w\hat{\boldsymbol{\rho}}, -\infty < w < \infty\} \quad (7.8)$$

Also, it's immediately clear that  $\hat{\boldsymbol{\rho}}$  and  $\boldsymbol{\delta}$  are mutually orthogonal by construction.

### 7.2.1.3 Obtaining the solution

The statement of the problem is as thus:

*Given* the displacement vector  $\boldsymbol{\delta}$ , laser ray direction  $\hat{\boldsymbol{\rho}}$ , target position

$\mathbf{r}_T$  and body frame position  $\mathbf{r}_B(t)$ ;

*Find* a pointing attitude  $\mathbf{R}_\xi(t)$  which illuminates the target.

An algorithm will be now presented which solves the displaced pointing problem. The reader is reminded that the final objective was to implement this solution as a Simulink model. With this in mind many compromises were made and, from a purely analytical standpoint, this solution may not be the most straightforward way to solve the problem as posed.

First, a new body-fixed coordinate frame  $m$  will be defined in which  ${}^m\hat{\boldsymbol{\rho}} = [1 \ 0 \ 0]^T$ . In this new frame also  ${}^m\boldsymbol{\delta}$  has the same  $Z$ -axis coordinate as  ${}^b\boldsymbol{\delta}$  and its  $X$  component is zero (the  $Y$ -axis component completes the unitary vector). The main part of the algorithm assumes this in order to simplify the calculations. This does not cause a loss of generality, because a simple coordinate change assures the results apply in the general case<sup>1</sup>. This will henceforth be called the *model problem*. For the purposes of the solution the choice for  ${}^m\hat{\boldsymbol{\rho}}$  is more or less arbitrary, but certainly having two null components and a unitary component makes the resulting equations simpler. The specific choice for  ${}^m\boldsymbol{\delta}$  (out of all unitary vectors perpendicular to  ${}^m\hat{\boldsymbol{\rho}}$ ) is related to minimizing roll angle during the trajectory, and will be explained further ahead.

---

<sup>1</sup>To verify this, it is sufficient to see that any pair of unitary vectors can be transformed to any other unitary pair with the same angle between them by a pure rotation—see, for example, Tanygin and Shuster (2007); Makley (1999). From their definition, it's immediately clear that  ${}^m\hat{\boldsymbol{\rho}}$  and  ${}^m\boldsymbol{\delta}$  are orthogonal, as are  ${}^b\hat{\boldsymbol{\rho}}$  and  ${}^b\boldsymbol{\delta}$  because of equation 7.7.

Define the global frame vector

$$\mathbf{r}_P(t) = \mathbf{r}_T - \mathbf{r}_B(t) \quad (7.9)$$

where  $\mathbf{r}_T$  is the position of the target, and  $\mathbf{r}_B(t)$  is the position of the body frame<sup>2</sup>. The vector  $\mathbf{r}_P(t)$  can be written as a time-varying unitary vector multiplied by a time-varying scalar length:

$$\mathbf{r}_P(t) = R(t) \begin{bmatrix} R_x(t) \\ R_y(t) \\ R_z(t) \end{bmatrix} \quad (7.10)$$

Similarly, the displacement vector  ${}^m\boldsymbol{\delta}$  will be written as a unitary direction vector multiplied by a scalar length:

$${}^m\boldsymbol{\delta} = \delta \begin{bmatrix} 0 \\ \delta_y \\ \delta_z \end{bmatrix} \quad (7.11)$$

The first step is to calculate a rotation matrix  $\mathbf{R}_p(t)$  which will point  ${}^m\hat{\boldsymbol{\rho}}$  directly at the target using only the first two rotations of the Euler sequence (that is,  $\phi = 0$ ). We use the popular TRIAD attitude determination algorithm (Black, 1964) in the formulation of Wertz (1978), where it goes by the name “algebraic method”. Consider  $\mathbf{M} = [\hat{\mathbf{q}} \ \hat{\mathbf{r}} \ \hat{\mathbf{s}}]$  to be a matrix representation of an orthonormal basis, built from the unitary noncollinear vectors  $\hat{\mathbf{u}}$  and  $\hat{\mathbf{v}}$  where

$$\begin{aligned} \hat{\mathbf{q}} &= \hat{\mathbf{u}} \\ \hat{\mathbf{r}} &= \frac{\hat{\mathbf{u}} \times \hat{\mathbf{v}}}{\|\hat{\mathbf{u}} \times \hat{\mathbf{v}}\|} \\ \hat{\mathbf{s}} &= \hat{\mathbf{q}} \times \hat{\mathbf{r}} \end{aligned} \quad (7.12)$$

Then a matrix  $\mathbf{R}_p(t)$  which satisfies the requirements is

$$\mathbf{R}_p(t) = \mathbf{M}_B \mathbf{M}_R^T \quad (7.13)$$

where the matrices  $\mathbf{M}_B$  and  $\mathbf{M}_R$  are, respectively, built through the algebraic method from the vector pairs  $\hat{\mathbf{u}}_B, \hat{\mathbf{v}}_B$  and  $\hat{\mathbf{u}}_R, \hat{\mathbf{v}}_R$  with

$$\begin{aligned} \hat{\mathbf{u}}_B = {}^m\hat{\boldsymbol{\rho}} &= \begin{bmatrix} 1 \\ 0 \\ 0 \end{bmatrix} & \hat{\mathbf{v}}_B &= \begin{bmatrix} 0 \\ 0 \\ -1 \end{bmatrix} & \hat{\mathbf{u}}_R &= \begin{bmatrix} R_x(t) \\ R_y(t) \\ R_z(t) \end{bmatrix} & \hat{\mathbf{v}}_R &= \begin{bmatrix} 0 \\ 0 \\ -1 \end{bmatrix} \end{aligned} \quad (7.14)$$

The matrix  $\mathbf{R}_p(t)$  is a direct pointing matrix—that is,  $\mathbf{R}_p(t) {}^m\hat{\boldsymbol{\rho}}$  would now point directly at the target if the displacement vector  ${}^m\boldsymbol{\delta}$  had zero length. To take our finite  ${}^m\boldsymbol{\delta}$  into account, the pointing must be altered by a axis-angle rotation<sup>3</sup>  $\mathbf{R}_d(\hat{\boldsymbol{\eta}}, \varphi(t))$

---

<sup>2</sup>A left superscript will not be used to denote the frame, because  $\mathbf{r}_P(t)$  is always expressed in the global frame  $g$ .

<sup>3</sup>The corresponding rotation matrix follows from Euler’s formula (Shuster, 1993):

$$\mathbf{R}(\hat{\boldsymbol{\eta}}, \varphi) = \mathbf{I} + \sin \varphi \hat{\boldsymbol{\eta}}^\times + (1 - \cos \varphi) (\hat{\boldsymbol{\eta}}^\times)^2 \quad (7.15)$$

where  $\hat{\boldsymbol{\eta}}^\times$  is defined in a similar way to  $\boldsymbol{\omega}^\times$  in equation 3.6.

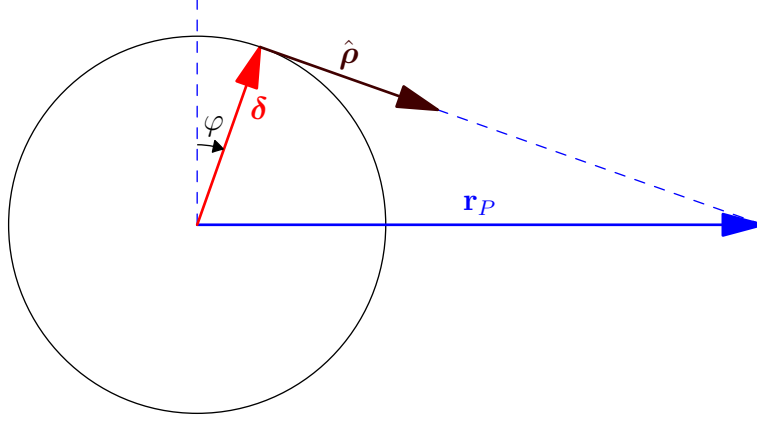


Figure 7.5: Pointing correction for non-null displacement.

where the rotation axis  $\hat{\mathbf{n}}$  is perpendicular both to  ${}^m\hat{\boldsymbol{\rho}}$  and  ${}^m\boldsymbol{\delta}$ , and the angle  $\varphi(t)$  is

$$\varphi(t) = \arcsin \frac{\delta}{R(t)} \quad (7.16)$$

This correction is illustrated in figure 7.5.

The resulting DCM for the model problem is

$$\mathbf{R}(t) = \mathbf{R}_d(t) \mathbf{R}_p(t) = \begin{bmatrix} \mathbf{R}_{11} & \mathbf{R}_{12} & \mathbf{R}_{13} \\ \mathbf{R}_{21} & \mathbf{R}_{22} & \mathbf{R}_{23} \\ \mathbf{R}_{31} & \mathbf{R}_{32} & \mathbf{R}_{33} \end{bmatrix} \quad (7.17)$$

where the individual terms  $\mathbf{R}_{ij}$  are:

$\mathbf{R}_{11}$ :

$$R_x(t) \sqrt{1 - \frac{\delta^2}{R(t)^2}} + \frac{\delta_y \delta R_y(t) + \delta_z \delta R_x(t) R_z(t)}{R(t) \sqrt{R_x(t)^2 + R_y(t)^2}} \quad (7.18)$$

$\mathbf{R}_{12}$ :

$$R_y(t) \sqrt{1 - \frac{\delta^2}{R(t)^2}} - \frac{\delta_y \delta R_x(t) - \delta_z \delta R_y(t) R_z(t)}{R(t) \sqrt{R_x(t)^2 + R_y(t)^2}} \quad (7.19)$$

$\mathbf{R}_{13}$ :

$$R_z(t) \sqrt{1 - \frac{\delta^2}{R(t)^2}} - \frac{\delta_z \delta \sqrt{R_x(t)^2 + R_y(t)^2}}{R(t)} \quad (7.20)$$

$\mathbf{R}_{21}$ :

$$\begin{aligned} & \frac{\delta_y \delta R_x(t)}{R(t)} - \\ & - \frac{R_y(t) \left( \delta_z^2 + \delta_y^2 \sqrt{1 - \frac{\delta^2}{R(t)^2}} \right) + \delta_y \delta_z R_x(t) R_z(t) \left( -1 + \sqrt{1 - \frac{\delta^2}{R(t)^2}} \right)}{\sqrt{R_x(t)^2 + R_y(t)^2}} \quad (7.21) \end{aligned}$$

**R**<sub>22</sub>:

$$\begin{aligned} & \frac{\delta_y \delta R_y(t)}{R(t)} + \\ & + \frac{R_x(t) \left( \delta_z^2 + \delta_y^2 \sqrt{1 - \frac{\delta^2}{R(t)^2}} \right) + \delta_y \delta_z R_y(t) R_z(t) \left( 1 - \sqrt{1 - \frac{\delta^2}{R(t)^2}} \right)}{\sqrt{R_x(t)^2 + R_y(t)^2}} \end{aligned} \quad (7.22)$$

**R**<sub>23</sub>:

$$\frac{\delta_y \delta R_z(t)}{R(t)} - \delta_y \delta_z \left( 1 - \sqrt{1 - \frac{\delta^2}{R(t)^2}} \right) \sqrt{R_x(t)^2 + R_y(t)^2} \quad (7.23)$$

**R**<sub>31</sub>:

$$\begin{aligned} & \frac{\delta_z \delta R_x(t)}{R(t)} - \\ & - \frac{R_x(t) R_z(t) \left( \delta_y^2 + \delta_z^2 \sqrt{1 - \frac{\delta^2}{R(t)^2}} \right) + \delta_y \delta_z R_y(t) \left( -1 + \sqrt{1 - \frac{\delta^2}{R(t)^2}} \right)}{\sqrt{R_x(t)^2 + R_y(t)^2}} \end{aligned} \quad (7.24)$$

**R**<sub>32</sub>:

$$\begin{aligned} & \frac{\delta_z \delta R_y(t)}{R(t)} - \\ & - \frac{R_y(t) R_z(t) \left( \delta_y^2 + \delta_z^2 \sqrt{1 - \frac{\delta^2}{R(t)^2}} \right) + \delta_y \delta_z R_x(t) \left( 1 - \sqrt{1 - \frac{\delta^2}{R(t)^2}} \right)}{\sqrt{R_x(t)^2 + R_y(t)^2}} \end{aligned} \quad (7.25)$$

**R**<sub>33</sub>:

$$\frac{\delta_z \delta R_z(t)}{R(t)} + \left( \delta_y^2 + \delta_z^2 \sqrt{1 - \frac{\delta^2}{R(t)^2}} \right) \sqrt{R_x(t)^2 + R_y(t)^2} \quad (7.26)$$

To get to the required result, the final step is to apply the coordinate change which will transform the original  ${}^b\hat{\rho}$  and  ${}^b\delta$  vectors (based on the physical parameters from the attitude platform) into the special parameters  ${}^m\hat{\rho}$  and  ${}^m\delta$  required for the model problem. To this end, one simply uses the algebraic method again with

$$\mathbf{R}_c = \mathbf{M}_B \mathbf{M}_R^T \quad (7.27)$$

where the vectors  $\hat{\mathbf{u}}_B$ ,  $\hat{\mathbf{v}}_B$  are, respectively,  ${}^b\hat{\rho}$  and  ${}^b\delta$  (the “real”  $\hat{\rho}$  and  $\delta$  vectors); and  $\hat{\mathbf{u}}_R$ ,  $\hat{\mathbf{v}}_R$  are the  ${}^m\hat{\rho}$  and  ${}^m\delta$  vectors used in the model problem calculation. The final result for the pointing is, then,

$$\mathbf{R}_\xi(t) = \mathbf{R}_c \mathbf{R}(t) \quad (7.28)$$

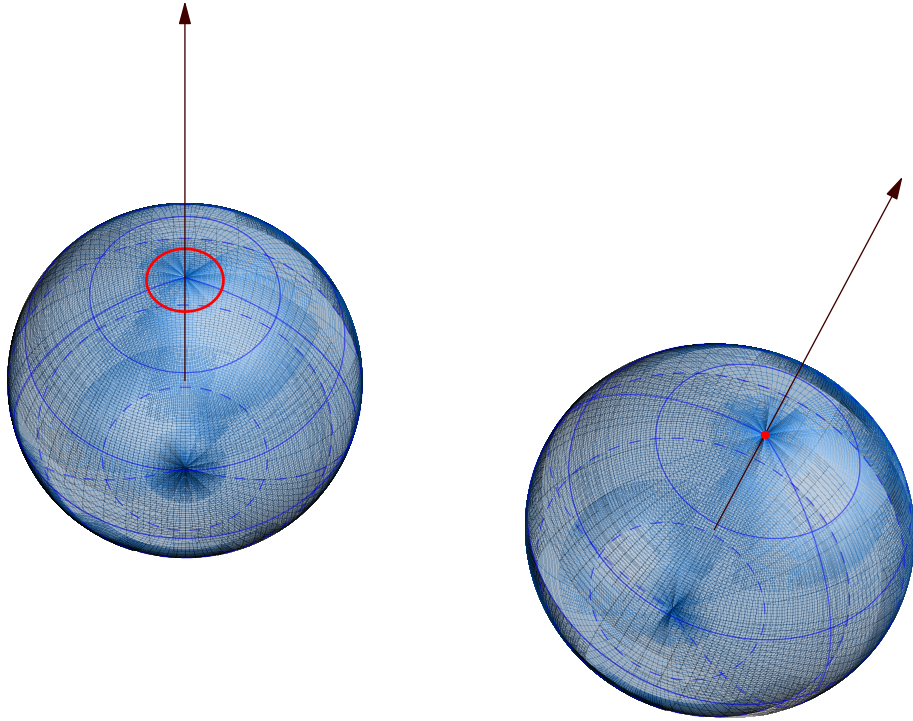


Figure 7.6: Comparison of the solution sets (in red; here shown projected on  $\mathbb{S}^2$ ): displaced pointing on the left, simple pointing on the right.

#### 7.2.1.4 Solution topology

As stated before, the solution set  $\mathcal{S}$  for the simple pointing problem has a degree of freedom inside the configuration space  $\text{SO}(3)$ . This is also the case for the displaced pointing problem and its solution set. To arrive at this conclusion, it's enough to think about the global frame vector  $\mathbf{r}_P(t) = {}^g\mathbf{r}_P(t)$  (which points from the body frame origin to the target) in body frame coordinates,  ${}^b\mathbf{r}_P(t)$ . Under a condition in which the target is already illuminated by the laser, any rotation about  ${}^b\mathbf{r}_P(t)$  will maintain that.

However, we are actually interested in finding out more about the solution set  $\mathcal{D} \subset \text{SO}(3)$  in terms of the transformations  $\mathbf{R}$  which bring the platform from a “natural” initial state—for example, where  ${}^b\hat{\rho}$  and  ${}^b\mathbf{r}_P(t)$  are coincident—to a situation of correct pointing as previously. Any such transformation  $\mathbf{R} \in \mathcal{D}$  can be seen as composed of a *fixed* transformation which brings the platform to a correct pointing, then a subsequent “free” rotation about  ${}^b\mathbf{r}_P(t)$ , as previously mentioned, confirming that  $\mathcal{D}$  indeed has a degree of freedom. If we project  $\mathcal{D}$  onto the 2-sphere  $\mathbb{S}^2$ , we get not a point containing a closed path over  $\text{SO}(3)$  as in the simple pointing problem, but a “ring” or “halo” where each point corresponds to a single configuration on  $\text{SO}(3)$ . The ring radius size is related only to the magnitude of the angle  $\varphi(t)$  (see equation 7.16), which by its turn depends only on the ratio between the displacement vector length and the current distance to the target. Consequently, as before, the solution set is also a one-dimensional smooth manifold contained in  $\text{SO}(3)$ —this time however the algebraic relationship between the components is not as simple. Figure 7.6 compares  $\mathcal{D}$  and  $\mathcal{S}$ .

The practical implication of this is that we can still minimize roll angle, but for this the solution had to be constructed with a little more effort. What defines this is the choice for  ${}^m\boldsymbol{\delta}$  in the model problem. It was constructed from the real platform displacement vector  ${}^b\boldsymbol{\delta}$  through what amounts to a  $Z$ -axis rotation precisely because this does not induce an extra roll angle in the solution. It is easy to see that any other possible choice for the model problem  ${}^m\boldsymbol{\delta}$  vector would cause the equivalent of a non-null rotation over  ${}^b\mathbf{r}_P(t)$  being applied to the platform at all moments. This would make force actuation by the thrusters much less effective, as explained in 7.2.1.1.

### 7.2.2 Feedforward

In the last section the importance of minimizing roll angle was made clear. However, the algorithm above does not guarantee the roll angle will be always null. Because of the way the solution algorithm was constructed, we gave up the opportunity to precisely control roll angle (and make it null) in exchange for separating  $\mathbf{R}_\xi(t)$  into a composition of  $\mathbf{R}_c$  and  $\mathbf{R}(t)$ . The reason for this was simplicity: for calculating the attitude feedforward references and torques, we have to obtain  $\dot{\mathbf{R}}_\xi(t)$  and  $\ddot{\mathbf{R}}_\xi(t)$ . By separating  $\mathbf{R}_\xi(t)$  into a constant part and a time-dependent part, getting analytical derivatives for the expressions becomes feasible.

Still, depending on the physical properties of the specific attitude platform, the roll angle can be made very small throughout the entire trajectory. This is certainly true for the TEAMS\_5D vehicle. With the selected trajectory, roll angle stays between  $-0.4^\circ$  and  $-0.6^\circ$ , which is not enough to affect force actuation in any significant way.

On obtaining  $\dot{\mathbf{R}}_\xi(t) = \mathbf{R}_c \dot{\mathbf{R}}(t)$  and  $\ddot{\mathbf{R}}_\xi(t) = \mathbf{R}_c \ddot{\mathbf{R}}(t)$ , the first and second time derivatives of  $R(t)$ ,  $R_x(t)$ ,  $R_y(t)$ ,  $R_z(t)$  will be required (equation 7.10). As analytical expression for  $\mathbf{r}_P(t)$  and its derivatives can be easily found from the expression for  $\mathbf{x}(t)$  and the target position, the required terms for  $R(t)$  are simply

$$\begin{aligned} R(t) &= \|\mathbf{r}_P(t)\| \\ \dot{R}(t) &= \frac{\mathbf{r}_{Px}(t) \dot{\mathbf{r}}_{Px}(t) + \mathbf{r}_{Py}(t) \dot{\mathbf{r}}_{Py}(t)}{\|\mathbf{r}_P(t)\|} \\ \ddot{R}(t) &= \frac{\mathbf{r}_{Px}(t) \ddot{\mathbf{r}}_{Px}(t) + \mathbf{r}_{Py}(t) \ddot{\mathbf{r}}_{Py}(t) + \dot{\mathbf{r}}_{Px}^2(t) + \dot{\mathbf{r}}_{Py}^2(t)}{\|\mathbf{r}_P(t)\|} \\ &\quad - \frac{(\mathbf{r}_{Px}(t) \dot{\mathbf{r}}_{Px}(t) + \mathbf{r}_{Py}(t) \dot{\mathbf{r}}_{Py}(t))^2}{\|\mathbf{r}_P(t)\|^3} \end{aligned} \tag{7.29}$$

It's useful to remember that, as the 5-DoF movement takes place on a horizontal plane,  $\dot{\mathbf{r}}_{Pz}(t) = \ddot{\mathbf{r}}_{Pz}(t) = 0$ .

The required terms for the other functions will be illustrated with the example

for  $R_x(t)$ :

$$\begin{aligned} R_x(t) &= \frac{\mathbf{r}_{Px}(t)}{R(t)} \\ \dot{R}_x(t) &= \frac{\dot{\mathbf{r}}_{Px}(t) - R_x(t) \dot{R}(t)}{R(t)} \\ \ddot{R}_x(t) &= \frac{\ddot{\mathbf{r}}_{Px}(t) - 2\dot{R}_x(t) \dot{R}(t) - R_x(t) \ddot{R}(t)}{R(t)} \end{aligned} \quad (7.30)$$

With the expressions for  $\mathbf{R}_\xi(t), \dot{\mathbf{R}}_\xi(t)$  and  $\ddot{\mathbf{R}}_\xi(t)$  it is possible to calculate the angular velocity reference and feedforward torque

$$\boldsymbol{\omega}_r = \begin{bmatrix} \omega_{rx} \\ \omega_{ry} \\ \omega_{rz} \end{bmatrix} \quad \mathbf{t}_r = \mathbf{I} \cdot \begin{bmatrix} \dot{\omega}_{rx} \\ \dot{\omega}_{ry} \\ \dot{\omega}_{rz} \end{bmatrix} + \boldsymbol{\omega}_r \times (\mathbf{I}\boldsymbol{\omega}_r) \quad (7.31)$$

First, let the matrices  $\boldsymbol{\Omega}$  and  $\dot{\boldsymbol{\Omega}}$  be:

$$\begin{aligned} \boldsymbol{\Omega} &= \dot{\mathbf{R}}_\xi(t) \mathbf{R}_\xi(t)^T \\ \dot{\boldsymbol{\Omega}} &= \ddot{\mathbf{R}}_\xi(t) \mathbf{R}_\xi(t)^T - \left( \dot{\mathbf{R}}_\xi(t) \mathbf{R}_\xi(t)^T \right)^2 \end{aligned}$$

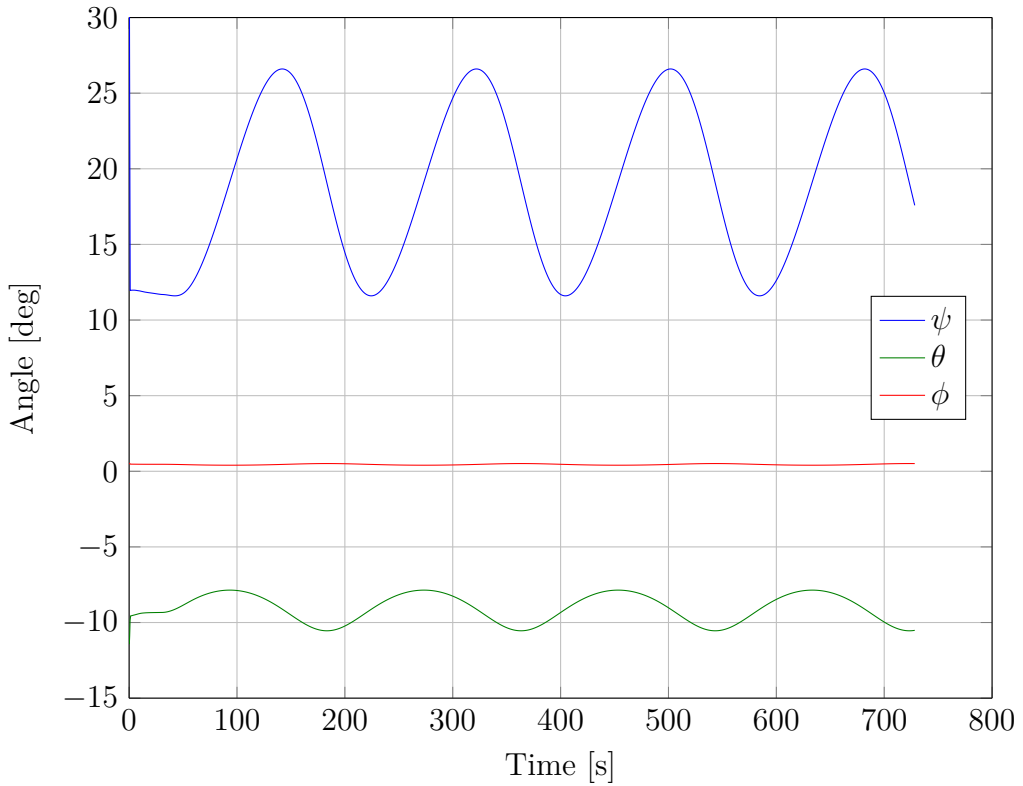
It can be shown (Wertz, 1978) that, then,

$$\boldsymbol{\Omega} = \begin{bmatrix} 0 & \omega_{rz} & -\omega_{ry} \\ -\omega_{rz} & 0 & \omega_{rx} \\ \omega_{ry} & -\omega_{rx} & 0 \end{bmatrix} \quad \dot{\boldsymbol{\Omega}} = \begin{bmatrix} 0 & \dot{\omega}_{rz} & -\dot{\omega}_{ry} \\ -\dot{\omega}_{rz} & 0 & \dot{\omega}_{rx} \\ \dot{\omega}_{ry} & -\dot{\omega}_{rx} & 0 \end{bmatrix} \quad (7.32)$$

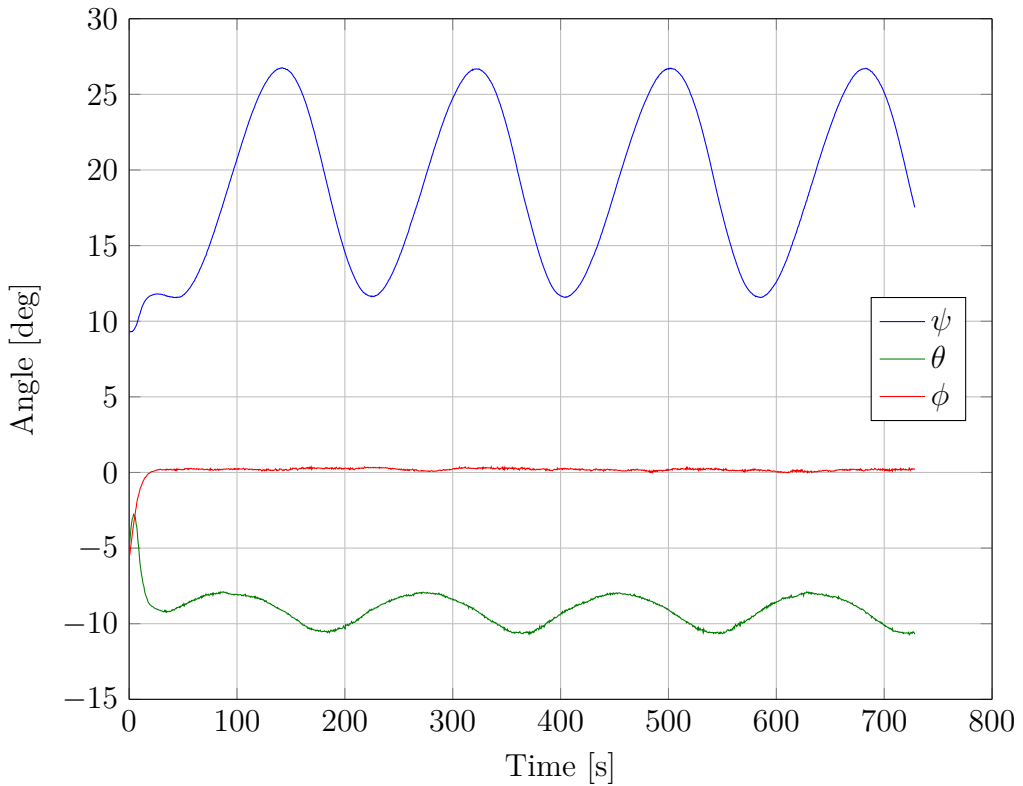
Therefore, vectors  $\boldsymbol{\omega}_r$  and  $\dot{\boldsymbol{\omega}}_r = \mathbf{I}^{-1}(\mathbf{t}_r - \boldsymbol{\omega}_r \times (\mathbf{I}\boldsymbol{\omega}_r))$  can be directly assembled from the components of  $\boldsymbol{\Omega}$  and  $\dot{\boldsymbol{\Omega}}$ .

As the parametrization uses trajectory time—albeit indirectly—it inherits equivalent properties from the position parametrization: continuous angular velocity reference at all times and continuous torque after  $t = 0_+$ .

Figure 7.7 shows the Euler angles of the attitude platform for a typical 5-DoF test. In this test, the vehicle moved in a circle around a point on one of the tables, while the target was at the other end of the table, on average about 5 m away. Both the calculated reference and the actual response (as sensed by the DTrack system) are shown. In figure 7.8 the pointing error during the same test is shown. This error represents the shortest distance from the laser ray line  $\mathcal{L}$  from the target point, calculated from the attitude and position supplied by the DTrack system.



(a) Euler angle attitude reference.



(b) Measured Euler angles.

Figure 7.7: 5-DoF closed-loop + feedforward test: attitude reference and results.

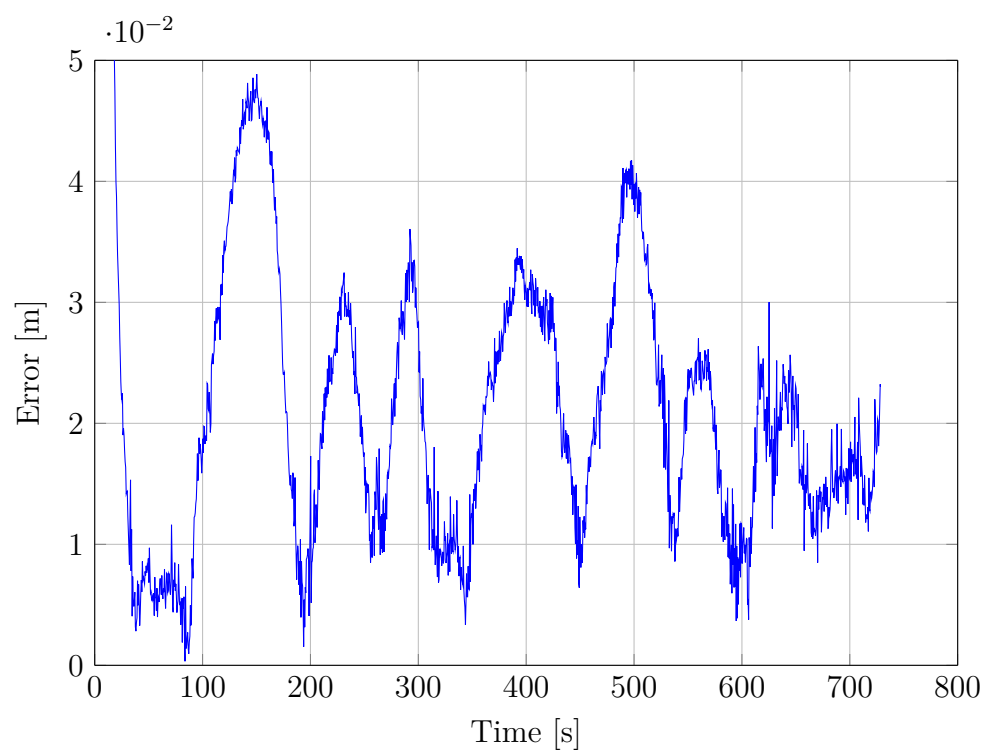


Figure 7.8: Pointing error for 5-DoF test. Note the scale ( $10^{-2}$  m).

# Chapter 8

## Conclusions

In this work, control of a 5-DoF satellite simulation platform was attained. Automated identification procedures were developed and applied. With the information about the relevant parameters, a control system was designed and implemented. Automated procedures for elimination of gravity disturbances were also implemented and used. Finally, a complete test of the platform, with trajectory following in both position and attitude, was implemented and successfully executed. All of the objectives defined at the start were achieved.

### 8.1 Lessons learned

**Development cycle** During the whole process the overarching approach was, at every step, to design a control system which supplies a certain functionality, simulate the proposed controller in MATLAB, then use the TEAMS facility to run real-time control tests. After the functionality had been verified, the next step was to increment the system with the next required function and repeat the process. Such a quick cycle of development-validation-testing proved very efficient in making the project move from very simple models to fulfilling the requirement of a complete pointing solution in only a few months.

**Record-keeping** From the start of the work, results data for every simulation and test was saved in a way that it could be quickly retrieved later. Also, the input parameters (gains, inertia tensor, starting pressure, balancing state, among others) were saved in the same file as the results. This made easy to compare results and be sure that the right things were being compared. On top of that, it cannot be stressed enough how useful it was, for example, to be able to run improved identification algorithms on data which had been collected much earlier, with other procedures in mind.

It should be noted that it pays to also record data which is apparently not relevant to the procedure at hand. On one occasion, a method 1 thruster identification procedure was returning very inconsistent readings. It was later verified that this was because the previous balancing procedure left stored momentum on the reaction wheels, causing a spurious cross-coupling torque to unexpectedly appear along with the thruster output. Reaction wheel data would not ordinarily be analyzed in thruster identification, because only the thrusters are used in method 1. But once the suspicion appeared, a quick look at the recorded data confirmed it.

## 8.2 Further work

Many ideas were produced in the course of the work, but the limited time available meant quite a few of them remained untested. Future works would probably benefit from implementing some or all of these.

- The inertia tensor estimate could be improved by using a least squares procedure which takes its properties (for example, positive-definiteness) into account. A starting point could be the article by Keim et al. (2006), where the authors describe using a constrained LSQ formulation based on linear matrix inequalities (LMIs) for inertia tensor estimation.
- Somewhat surprisingly, 5-DoF test results have shown the main source of inaccuracy to be the position error, instead of the attitude error. A complete identification of the thrusters' force vectors, although quite time-consuming, would certainly prove extremely beneficial to the project in the long run.
- Only the main sources of disturbances were considered. A more detailed study on the disturbances, including air bearing-originated ones, could reveal interesting facts. Also, as the attitude platform is quite heavy, it is possible that anisoelastic disturbances might play a somewhat relevant role.
- Pressure variation estimation could be much improved with a better model of thruster air consumption at different thrust levels.
- Lastly, improving the state filtering (possibly by means of an observer) might lead to better results both for identification and testing, by reducing high-frequency noise from the IMU and DTrack sensors.

# References

- Advanced Realtime Tracking GmbH (2013). DTrack User Manual.
- Agrawal, B. N. and Rasmussen, R. E. (2001). Air-bearing-based satellite attitude dynamics simulator for control software research and development. In Murrer, Jr., R. L., editor, *Proc. SPIE 4366, Technologies for Synthetic Environments: Hardware-in-the-Loop Testing VI*, volume 4366, pages 204–214.
- Aguiar, A. P. and Hespanha, J. a. P. (2007). Trajectory-Tracking and Path-Following of Underactuated Autonomous Vehicles With Parametric Modeling Uncertainty. *IEEE Transactions on Automatic Control*, 52(8):1362–1379.
- Altmann, S. L. (1989). Hamilton, Rodrigues, and the Quaternion Scandal. *Mathematics Magazine*, 62(5):291.
- Astro- und Feinwerktechnik Adlershof GmbH (2008). Short Specification – Reaction Wheel RW 90.
- Astro- und Feinwerktechnik Adlershof GmbH (2015). DTrack setup. Available at: <http://www.ar-tracking.com>.
- Bauer, F., Bristow, J., Folta, D., Hartman, K., Quinn, D., and How, J. (1997). Satellite formation flying using an innovative autonomous control system (Auto-Con) environment. In *Guidance, Navigation, and Control Conference*, Reston, VA. American Institute of Aeronautics and Astronautics.
- Beard, R., Lawton, J., and Hadaegh, F. (2001). A coordination architecture for spacecraft formation control. *IEEE Transactions on Control Systems Technology*, 9(6):777–790.
- Beichman, C., Lawson, P., Lay, O., Ahmed, A., Unwin, S., and Johnston, K. (2006). Status of the terrestrial planet finder interferometer (TPF-I). In Monnier, J. D., Schöller, M., and Danchi, W. C., editors, *Proceedings of SPIE*, volume 6268, pages 62680S–62680S–9.
- Bergmann, E. V., Walker, B. K., and Levy, D. R. (1987). Mass property estimation for control of asymmetrical satellites. *Journal of Guidance, Control, and Dynamics*, 10(5):483–491.
- Bhat, S. P. and Bernstein, D. S. (2000). A topological obstruction to continuous global stabilization of rotational motion and the unwinding phenomenon. *Systems & Control Letters*, 39(1):63–70.

## References

- Black, H. D. (1964). A passive system for determining the attitude of a satellite. *AIAA Journal*, 2(7):1350–1351.
- Bristow, J., Folta, D., and Hartman, K. (2000). A formation flying technology vision. In *Space 2000 Conference and Exposition*, number September, Reston, VA. American Institute of Aeronautics and Astronautics.
- Brown, O. and Eremenko, P. (2006). The Value Proposition for Fractionated Space Architectures. In *Space 2006*, number September, pages 1–23, Reston, VA. American Institute of Aeronautics and Astronautics.
- Camp, J., LeMaster, E., Nortman, S., and Cordova, S. (2004). Formation Control of Holonomic Air-Bearing Robots Using Potential Field Interaction Laws. In *AIAA Guidance, Navigation, and Control Conference and Exhibit*, number August, pages 1–12, Reston, VA. American Institute of Aeronautics and Astronautics.
- Chaturvedi, N., Sanyal, A., and McClamroch, N. H. (2011). Rigid-Body Attitude Control. *IEEE Control Systems Magazine*, 31(3):30–51.
- Chesi, S., Gong, Q., Pellegrini, V., Cristi, R., and Romano, M. (2014). Automatic Mass Balancing of a Spacecraft Three-Axis Simulator: Analysis and Experimentation. *Journal of Guidance, Control, and Dynamics*, 37(1):197–206.
- Cho, D.-M., Jung, D., and Tsotras, P. (2009). A 5-dof Experimental Platform for Spacecraft Rendezvous and Docking. In *AIAA Infotech@Aerospace Conference*, number April, Reston, VA. American Institute of Aeronautics and Astronautics.
- Cho, S. and McClamroch, N. H. (2002). Feedback control of triaxial attitude control testbed actuated by two proof mass devices. In *Proceedings of the 41st IEEE Conference on Decision and Control, 2002.*, volume 1, pages 498–503. IEEE.
- Cho, S., Shen, J., McClamroch, N. H., and Bernstein, D. (2001). Equations of motion for the triaxial attitude control testbed. In *Proceedings of the 40th IEEE Conference on Decision and Control (Cat. No.01CH37228)*, volume 4, pages 3429–3434. IEEE.
- Choset, H., Knepper, R., Flasher, J., Walker, S., Alford, A., Jackson, D., Koertenkamp, D., Burridge, R., and Fernandez, J. (1999). Path planning and control for AERCam, a free-flying inspection robot in space. In *Proceedings 1999 IEEE International Conference on Robotics and Automation (Cat. No.99CH36288C)*, volume 2, pages 1396–1403. IEEE.
- Chung, S.-J., Kong, E., and Miller, D. (2005). Dynamics and Control of Tethered Formation Flight Spacecraft Using the SPHERES Testbed. In *AIAA Guidance, Navigation, and Control Conference and Exhibit*, number August, Reston, VA. American Institute of Aeronautics and Astronautics.
- Clohessy, W. H. and Wiltshire, R. S. (1960). Terminal guidance system for satellite rendezvous. *Journal of the Aerospace Sciences*, 27(9):653–658.

## References

- Crouch, P. (1984). Spacecraft attitude control and stabilization: Applications of geometric control theory to rigid body models. *IEEE Transactions on Automatic Control*, 29(4):321–331.
- Danzmann, K. and Rüdiger, A. (2003). LISA technology – concept, status, prospects. *Classical and Quantum Gravity*, 20(10):S1–S9.
- Delpech, M., Malbet, F., Karlsson, T., Larsson, R., Léger, A., and Jorgensen, J. (2014). Flight demonstration of formation flying capabilities for future missions (NEAT pathfinder). *Acta Astronautica*, 105(1):82–94.
- Deutsches Zentrum für Luft- und Raumfahrt e.V. (2009). TanDEM-X – Die Erde in drei Dimensionen. Available at: [http://www.dlr.de/dlr/en/Portaldatal/1/Resources/documents/TanDEM-X\\_web.pdf](http://www.dlr.de/dlr/en/Portaldatal/1/Resources/documents/TanDEM-X_web.pdf).
- Deutsches Zentrum für Luft- und Raumfahrt e.V. (2014). The German Aerospace Center (DLR). Available at: [http://www.dlr.de/dlr/en/Portaldatal/1/Resources/documents/2012\\_1/The\\_DLR\\_GB.pdf](http://www.dlr.de/dlr/en/Portaldatal/1/Resources/documents/2012_1/The_DLR_GB.pdf).
- Deutsches Zentrum für Luft- und Raumfahrt e.V. (2015). TEAMS test facility. Available at: [http://www.dlr.de/irs/en/desktopdefault.aspx/tabcid-6883/12025\\_read-28929/](http://www.dlr.de/irs/en/desktopdefault.aspx/tabcid-6883/12025_read-28929/).
- Durham, W. C. (1993). Constrained control allocation. *Journal of Guidance, Control, and Dynamics*, 16(4):717–725.
- Eickhoff, J. (2009). *Simulating Spacecraft Systems*, volume 1 of *Springer Aerospace Technology*. Springer Berlin Heidelberg, Berlin, Heidelberg.
- Faller, R., Ohndorf, A., Schlepp, B., and Eberle, S. (2012). Preparation, Handover, and Conduction of PRISMA Mission Operations at GSOC. In *63rd International Astronautical Congress of the International Astronautical Federation*, pages 1–11, Naples.
- Fasano, G. and D'Errico, M. (2009). Modeling orbital relative motion to enable formation design from application requirements. *Celestial Mechanics and Dynamical Astronomy*, 105(1-3):113–139.
- Ferguson, P., Yang, T., Tillerson, M., and How, J. (2002). New Formation Flying Testbed for Analyzing Distributed Estimation and Control Architectures. In *AIAA Guidance, Navigation, and Control Conference and Exhibit*, number August, pages 1–11, Reston, VA. American Institute of Aeronautics and Astronautics.
- Fosth, D. C. (1967). The Lunar Orbiter Attitude Control Simulator. *IEEE Transactions on Aerospace and Electronic Systems*, AES-3(3):417–423.
- Hatcher, N. M. and Young, R. N. (1968). An automatic balancing system for use on frictionlessly supported attitude-controlled test platforms. Technical Report March, NASA Langley Research Center, Hampton, VA.

## References

- Hill, G. W. (1878). Researches in the Lunar Theory. *American Journal of Mathematics*, 1(1):5.
- Hopf, H. (1940). Systeme symmetrischer Bilinearformen und euklidische Modelle der projektiven Räume. *Vierteljahrsschrift der Naturforschenden Gesellschaft in Zürich*, 85(7):165–177.
- Jung, D. and Tsotoras, P. (2003). A 3-DoF Experimental Test-Bed for Integrated Attitude Dynamics and Control Research. In *AIAA Guidance, Navigation, and Control Conference and Exhibit*, number August, Reston, VA. American Institute of Aeronautics and Astronautics.
- Kapila, V., Sparks, A. G., Buffington, J. M., and Yan, Q. (2000). Spacecraft Formation Flying: Dynamics and Control. *Journal of Guidance, Control, and Dynamics*, 23(3):561–564.
- Keim, J., Aqikmese, A., and Shields, J. (2006). Spacecraft Inertia Estimation Via Constrained Least Squares. In *2006 IEEE Aerospace Conference*. IEEE.
- Kim, B., Velenis, E., Kriengsiri, P., and Tsotoras, P. (2003). Designing a low-cost spacecraft simulator. *IEEE Control Systems Magazine*, 23(4):26–37.
- Kim, J. J. and Agrawal, B. N. (2006). System Identification and Automatic Mass Balancing of Ground-Based Three-Axis Spacecraft Simulator. In *AIAA Guidance, Navigation, and Control Conference and Exhibit*, number August, pages 1–12, Reston, VA. American Institute of Aeronautics and Astronautics.
- Kim, J. J. and Agrawal, B. N. (2009). Automatic Mass Balancing of Air-Bearing-Based Three-Axis Rotational Spacecraft Simulator. *Journal of Guidance, Control, and Dynamics*, 32(3):1005–1017.
- Koditschek, D. (1988). Application of a new Lyapunov function to global adaptive attitude tracking. In *Proceedings of the 27th IEEE Conference on Decision and Control*, number December, pages 63–68. IEEE.
- Krieger, G., Moreira, A., Fiedler, H., Hajnsek, I., Werner, M., Younis, M., and Zink, M. (2007). TanDEM-X: A Satellite Formation for High-Resolution SAR Interferometry. *IEEE Transactions on Geoscience and Remote Sensing*, 45(11):3317–3341.
- Lawson, C. L. and Hanson, R. J. (1974). *Solving Least Squares Problems*. Society for Industrial and Applied Mathematics, Philadelphia, PA.
- Ledebuhr, A. G., Ng, L. C., Jones, M. S., Wilson, B. A., Gaughan, R. J., Breitfeller, E. F., Taylor, W. G., Robinson, J. A., Antelman, D. R., and Nielsen, D. P. (2001). Micro-satellite ground test vehicle for proximity and docking operations development. In *2001 IEEE Aerospace Conference Proceedings (Cat. No.01TH8542)*, volume 5, pages 2493–2504. IEEE.
- Lee, A. Y. and Wertz, J. a. (2002). In-Flight Estimation of the Cassini Spacecraft’s Inertia Tensor. *Journal of Spacecraft and Rockets*, 39(1):153–155.

## References

- Lee, J. M. (2012). *Introduction to Smooth Manifolds*, volume 218 of *Graduate Texts in Mathematics*. Springer New York, New York, NY.
- Leite Filho, W., Mallaco, L., and Carrijo, D. (1999). Hardware in the loop simulation of an attitude control system. In *Modeling and Simulation Technologies Conference and Exhibit*, number c, pages 3–6, Reston, VA. American Institute of Aeronautics and Astronautics.
- Makley, F. L. (1999). Attitude Determination Using Two Vector Measurements. In *Proceedings of the Flight Mechanics Symposium*, pages 39–52, Greenbelt, MD.
- Mattingley, J. and Boyd, S. (2012). CVXGEN: a code generator for embedded convex optimization. *Optimization and Engineering*, 13(1):1–27.
- Mesbahi, M. and Hadaegh, F. Y. (2001). Formation Flying Control of Multiple Spacecraft via Graphs, Matrix Inequalities, and Switching. *Journal of Guidance, Control, and Dynamics*, 24(2):369–377.
- Molette, P., Cougnet, C., Saint-Aubert, P., Young, R., and Helas, D. (1984). Technical and economical comparison between a modular geostationary space platform and a cluster of satellites. *Acta Astronautica*, 11(12):771–784.
- Moran, F. J. and Dishman, B. H. (1970). Air bearing table mechanization and verification of a spacecraft wide angle attitude control system. *Journal of Spacecraft and Rockets*, 7(7):819–825.
- Nolet, S. (2007). The SPHERES Navigation System: from Early Development to On-Orbit Testing. In *AIAA Guidance, Navigation and Control Conference and Exhibit*, number August, pages 1–17, Reston, VA. American Institute of Aeronautics and Astronautics.
- Ogata, K. (2001). *Modern Control Engineering*. Prentice Hall PTR, Upper Saddle River, NJ, USA, 4th edition.
- Oosting, K. and Dickerson, S. (1988). Simulation of a high-speed lightweight arm. In *Proceedings. 1988 IEEE International Conference on Robotics and Automation*, pages 494–496. IEEE Comput. Soc. Press.
- Pascoal, A. M. and Aguiar, A. P. (2011). Trajectory tracking & Path-following control. Available at: [http://www.eeci-institute.eu/GSC2011/Photos-EECI/EECI-GSC-2011-M6/EECI-GSC-2011-M6/06\\_TrackPFcontrol.pdf](http://www.eeci-institute.eu/GSC2011/Photos-EECI/EECI-GSC-2011-M6/EECI-GSC-2011-M6/06_TrackPFcontrol.pdf).
- Robertson, A., Inalhan, G., and How, J. (1999). Spacecraft formation flying control design for the Orion mission. In *Guidance, Navigation, and Control Conference and Exhibit*, number c, Reston, VA. American Institute of Aeronautics and Astronautics.
- Romano, M. (2005). On-the-ground experiments of autonomous spacecraft proximity-navigation using computer vision and jet actuators. In *Proceedings, 2005 IEEE/ASME International Conference on Advanced Intelligent Mechatronics*, pages 1011–1016. IEEE.

## References

- Sabol, C., Burns, R., and McLaughlin, C. A. (2001). Satellite Formation Flying Design and Evolution. *Journal of Spacecraft and Rockets*, 38(2):270–278.
- Salcudean, S. (1988). On the control of magnetically levitated robot wrists. In *Proceedings of the 27th IEEE Conference on Decision and Control*, pages 186–191. IEEE.
- Scharf, D., Hadaegh, F., and Ploen, S. (2003). A survey of spacecraft formation flying guidance and control (part I): guidance. In *Proceedings of the 2003 American Control Conference*, volume 2, pages 1733–1739. IEEE.
- Scharf, D., Hadaegh, F., and Ploen, S. (2004). A survey of spacecraft formation flying guidance and control (part II): control. In *Proceedings of the 2004 American Control Conference*, volume 4, pages 2976–2985. IEEE.
- Schaub, H. and Junkins, J. L. (2009). *Analytical Mechanics of Space Systems*. AIAA, Reston, VA, USA, 2nd edition.
- Schlotterer, M. and Novoschilov, S. (2012). On-Ground Path Planning Experiments for Multiple Satellites. In *23rd International Symposium on Space Flight Dynamics*.
- Schwartz, J. L. (2004). *The Distributed Spacecraft Attitude Control System Simulator: From Design Concept to Decentralized Control*. PhD thesis, Virginia Polytechnic Institute and State University.
- Schwartz, J. L., Peck, M. A., and Hall, C. D. (2003). Historical Review of Air-Bearing Spacecraft Simulators. *Journal of Guidance, Control, and Dynamics*, 26(4):513–522.
- Schweighart, S. A. and Sedwick, R. J. (2002). High-Fidelity Linearized  $J_2$  Model for Satellite Formation Flight. *Journal of Guidance, Control, and Dynamics*, 25(6):1073–1080.
- Servidua, P. and Pena, R. (2005). Spacecraft thruster control allocation problems. *IEEE Transactions on Automatic Control*, 50(2):245–249.
- Shen, J., McClamroch, N. H., and Bloch, A. (2002). Local equilibrium controllability of the triaxial attitude control testbed. In *Proceedings of the 41st IEEE Conference on Decision and Control, 2002.*, volume 1, pages 528–533. IEEE.
- Shuster, M. D. (1993). A Survey of Attitude Representations. *The Journal of the Astronautical Sciences*, 41(4):439–517.
- Sidi, M. J. (1997). *Spacecraft Dynamics and Control*. Cambridge University Press, Cambridge, UK, 4th edition.
- Smith, G. A. (1965). Dynamic Simulators for Test of Space Vehicle Attitude Control Systems. In *Proceedings of the Conference on the Role of Simulation in Space Technology, Part C*, Blackburg, VA. Virginia Polytechnic Inst. and State Univ.

## References

- Stamminger, A., Altenbuchner, L., Ettl, J., Hörschgen-Eggers, M., Jung, W., and Turner, P. (2013). DLR's Mobile Rocket Base - Flight Tickets for your Microgravity Experiments. In *64th International Astronautical Congress of the International Astronautical Federation*, Beijing, China.
- Stuelpnagel, J. (1964). On the Parametrization of the Three-Dimensional Rotation Group. *SIAM Review*, 6(4):422–430.
- Tang, S., Zhang, S., and Zhang, Y. (2011). A Modified Direct Allocation Algorithm with Application to Redundant Actuators. *Chinese Journal of Aeronautics*, 24(3):299–308.
- Tanygin, S. and Shuster, M. D. (2007). The Many TRIAD Algorithms. In *Proceedings of the AAS/AIAA 17th Space Flight Mechanics Meeting*, volume 127, pages 81–99, Sedona, AZ.
- Tanygin, S. and Williams, T. (1997). Mass Property Estimation Using Coasting Maneuvers. *Journal of Guidance, Control, and Dynamics*, 20(4):625–632.
- Ustrzycki, T., Lee, R., and Chesser, H. (2011). Spherical Air Bearing Attitude Control Simulator for Nanosatellites. In *AIAA Modeling and Simulation Technologies Conference*, number August, pages 1–9, Reston, VA. American Institute of Aeronautics and Astronautics.
- Viswanathan, S. P., Sanyal, A., and Holguin, L. (2012). Dynamics and Control of a Six Degrees of Freedom Ground Simulator for Autonomous Rendezvous and Proximity Operation of Spacecraft. In *AIAA Guidance, Navigation, and Control Conference*, number August, pages 1–19, Reston, VA. American Institute of Aeronautics and Astronautics.
- Wen, J.-Y. and Kreutz-Delgado, K. (1991). The attitude control problem. *IEEE Transactions on Automatic Control*, 36(10):1148–1162.
- Wertz, J. R., editor (1978). *Spacecraft Attitude Determination and Control*. Kluwer, Dordrecht, Netherlands.
- Wertz, J. R., Everett, D. F., and Puschell, J. J., editors (2011). *Space Mission Engineering: The New SMAD*. Microcosm Press, Hawthorne, CA, USA.
- Wilcock, D. F. (1965). Design and Performance of Gas-Pressurized, Spherical, Space-Simulator Bearings. *Journal of Basic Engineering*, 87(3):604.
- Wu, Y.-H., Gao, Y., Lin, J.-W., Raus, R., Zhang, S.-J., and Watt, M. (2014). Low-Cost, High-Performance Monocular Vision System for Air Bearing Table Attitude Determination. *Journal of Spacecraft and Rockets*, 51(1):66–75.
- Yamanaka, K. and Ankersen, F. (2002). New State Transition Matrix for Relative Motion on an Arbitrary Elliptical Orbit. *Journal of Guidance, Control, and Dynamics*, 25(1):60–66.

## References

- Yang, Y. and Cao, X. (2006). Design and Development of the Small Satellite Attitude Control System Simulator. In *AIAA Modeling and Simulation Technologies Conference and Exhibit*, number August, pages 1–7, Reston, VA. American Institute of Aeronautics and Astronautics.
- Yelun, X. (2003). The Dynamical Equations in Terms of Relative Orbit Elements for Satellite Formation Flying. In *54th International Astronautical Congress of the International Astronautical Federation, the International Academy of Astronautics, and the International Institute of Space Law*, number October, Bremen. American Institute of Aeronautics and Astronautics.

# Appendix A

## Air mass inertia calculation

The attitude platform's bottles each carry about one liter of air. When completely full at 300 atm, a bottle's carried air mass is approximately  $m = 0.374 \text{ kg}$  (at  $20^\circ \text{ C}$ ).

We can approximate the bottles as  $h = 0.2 \text{ m}$  length cylinders aligned longitudinally with the  $X$  or  $Y$  axes, with a  $r = 0.04 \text{ m}$  radius. The distance between bottle centroid and center of rotation is  $d = 0.3 \text{ m}$ .

A cylinder turning about a radius over its centroid has a moment of inertia

$$I = \frac{1}{12}m(3r^2 + h^2) \quad (\text{A.1})$$

The principal moments of inertia can then be calculated as:

$$\begin{aligned} I_{zz} &= 4 \left[ \frac{1}{12}m(3r^2 + h^2) + md^2 \right] \\ &= \frac{1}{3}m(3r^2 + h^2 + 12d^2) \\ &\approx 0.1402 \text{ kgm}^2 \end{aligned} \quad (\text{A.2})$$

$$\begin{aligned} I_{xx} = I_{yy} &= 2 \left( \frac{mr^2}{2} \right) + \frac{I_{zz}}{2} \\ &\approx 0.0707 \text{ kgm}^2 \end{aligned} \quad (\text{A.3})$$